SAPIENZA
UNIVERSITÀ DI ROMA

Faculty of Civil and Industrial Engineering
Department of Structural and Geotechnical Engineering

PhD Thesis in Structural Engineering

Micromechanical and macromechanical approaches for the analysis of periodic masonry structures

PhD Candidate:
Mariacarla Nocera

Advisor:
Prof. Daniela Addessi

Co-Advisor:
Prof. Domenico Liberatore

Rome, April 2021

To my family.

Abstract

In European countries, preservation of masonry architectural heritage is a felt concern. The most fascinating landscapes are characterized by a large presence of masonry structures that have become part of country cultural identity. This justifies the lively interest towards the development of efficient computational tools to assess the structural capacity of masonry buildings. Among the available modeling strategies, finite element models seem to be suitable tools to characterize the evolution of the nonlinear mechanisms occurring in the material under typical loading conditions. This work focuses on finite element modeling of masonry structures at different scales. A micromechanical model, based on a damage-plastic constitutive law for masonry mortar joints, is developed to reproduce the structural response of unreinforced masonry arches, by studying global force-displacement response curves and collapse mechanisms. The proposed model is implemented in finite element procedures, where the mesh-dependency problem is efficiently overcome by adopting nonlocal integral formulations. To prove the efficiency of the adopted model, the response of experimentally tested walls and arches is numerically reproduced. Then, some parametric analyses on arches are performed with the aim of analyzing the effect of most relevant geometrical and mechanical parameters on the global structural response. Subsequently, the use of macromodeling technique based on smeared crack constitutive laws for the cyclic in-plane analysis of masonry panels is explored. The numerical investigation is focused on two material macromechanical models (total strain cracking and crack and plasticity) that show some limitations when analyzing the behavior of masonry structures subjected to in-plane cyclic loading. A modified version of the Drucker-Prager model including cohesive softening is introduced to overcome these shortcomings.

It is proved that the numerical results correlate better with the experimental outcomes. In particular, attention is focused on two different techniques adopted to overcome the mesh-dependency of the finite element solution: fracture energy regularization and nonlocal integral approach. A single-fixed smeared crack is implemented in finite element procedures adopting these two different techniques. Numerical applications are performed to prove the robustness and stability of these two approaches.

Acknowledgements

Special thanks to my professors. If I am here today and reach this goal, it is my own and their success.

I want to thank Professor Daniela Addessi for the guidance and great help throughout the work I tackled and Professor Domenico Liberatore for his support and wise advice.

I want to thank Professor Paulo B. Lourenço for the kind welcome and for allowing me to be part of his research group during the six months I spent at the University of Minho.

With affection, I thank my traveling friends, those who supported me everywhere in this long road.

I want to thank my parents, my sister, my big family, and my closest friends. I am grateful to all of you for always believing in me, for being there for me, supporting me, especially in the most stressful moments.

Last but not least, I gratefully thank my imaginary friends for their everlasting and unconditional love. It was fundamental during the time I spent writing my thesis.

Contents

1 Introduction **1**

1.1 Motivations and historical background 1

1.2 Objectives and scopes 5

1.3 Organization of the thesis 6

2 State of the art **8**

2.1 Historical masonry constructions 8

2.1.1 Mechanical behavior of masonry material 8

2.1.2 Structural elements: walls and arches 15

2.2 Modeling approaches for masonry structures and analysis strategies 31

2.2.1 FEM based approaches 32

2.2.2 Structural component models 41

2.2.3 Discrete element method 43

2.2.4 Limit analysis 44

2.3 Overview of constitutive models for masonry 48

2.3.1 Continuum damage models 48

2.3.2 Smeared crack models 52

2.3.3 Plasticity models 54

2.4 Overview of localization problems and regularization techniques . 57

2.4.1 Strain localization due to softening 58

2.4.2 Fracture energy regularization 61

2.4.3 Nonlocal integral regularization 62

3 Micromechanical finite element modeling of masonry structures 66

3.1 Damage-plastic model 66

3.1.1 Computational aspects 71
3.2 Response of masonry walls 73
3.3 Response of unreinforced masonry arches 83
3.3.1 Experimental-numerical comparison 84
3.3.2 Effect of geometry 87
3.3.3 Effect of material parameters 91
3.4 Summary 94

4 Macromechanical finite element modeling of masonry structures 96
4.1 Smeared crack constitutive models 97
4.1.1 Total strain cracking model 97
4.1.2 Crack and plasticity model 101
4.1.3 Modified crack and plasticity model 106
4.1.4 Numerical application 109
4.2 Summary 119

5 Regularized smeared crack model 121
5.1 A single-fixed smeared crack model 121
5.1.1 Fracture energy regularization 125
5.1.2 Nonlocal regularization 127
5.1.3 Computational aspects 129
5.2 Numerical applications 130
5.3 Summary 138

6 Conclusive remarks 143

List of Figures

1.1 Some Italian masonry landscapes: (a) Ponte delle Torri, Spoleto (b) Civita di Bagnoreggio. 2
1.2 Failure mechanisms of masonry structures (Gatta, 2019). 3
1.3 Failure mechanisms of masonry arch: (a) Four - hinge mechanism and (b) sliding; (Melbourne et al., 2007). 4
1.4 (a) The Colosseum and (b) a detail of a sliding mechanism on one of its arches. 4
1.5 (a) Mausoleum of Teodorico and (b) a detail of a sliding mechanism on one of its arches. 5

2.1 Stone masonry textures (Lourenço, 1998). 9
2.2 Most common brick masonry textures. 9
2.3 Compressive behavior for uni-axial load normal to bed joints: (a) state of stress in masonry constituents and (b) failure mode of a masonry prism. 11
2.4 Page (1981, 1983): local state of stress in masonry prisms under uni-axial compression with different orientation θ from the bed joint direction. 11
2.5 Failure modes of masonry walls under direct tension: (a) cracks passing along mortar and bricks and (b) zigzag type for load parallel to bed joint orientation, from Backes (1985). 12
2.6 Page (1983): local state of stress in masonry prisms under uni-axial tension with different orientation θ from the bed joint direction. . 12
2.7 Typical behavior of quasi-bittle materials under tensile loading and definition of mode I fracture energy G_{fI}. 13

2.8 Typical behavior of quasi-bittle materials under compressive loading and definition of fracture energy G_c. 13
2.9 Behavior of masonry under shear and definition of mode II fracture energy. 14
2.10 Masonry bi-axial strength: experimental results of Page (1981, 1983) for (a) $\theta = 0°$, (b) $\theta = 22.5°$and (c) $\theta = 45°$. 15
2.11 Typical stone masonry sections: one, two, and three leaves Binda et al. (1999). 17
2.12 Examples of brick masanry section Binda and Saisi (2002). 18
2.13 Typical failure modes of masonry walls: (a) rocking; (b) sliding shear failure; and (c) diagonal cracking (adapted from Calderini et al. (2009)). 20
2.14 Three methods of spanning a passageway: (a) post and lintel system, (b) corbelled arch, (c) arch. (from Iannuzzo (2018)). 21
2.15 Some types of post and lintel system: (a) Stonehenge (b) Machu Picchu (from Iannuzzo (2018)). 22
2.16 Some historical examples of a corbelled arch: (a) Kompong Kdei Bridge of Cambodia, (b) False arch at "Cuadrángulo de las monjas" at Uxmal in Yucatán - Maya architecture (from Iannuzzo (2018)). 23
2.17 Some historical arch structures: Colosseum. 24
2.18 Some historical arch structures: (a) Arch of Triumph (destroyed) in Syria's Palmyra ruins, (b) aqueduct in the Old Town of Segovia (from Iannuzzo (2018)). 24
2.19 Some types of arch. 25
2.20 The pushing effect exerted by the vault on the piers for Vitruvio. 26
2.21 A famous drawing from the Forster Codex (a) which shows an experimental test on an arch made by Leonardo da Vinci. He formulated a safety criterion (b) and a failure rule (c). 26
2.22 Structure of St Paul's Cathedral in London. 27
2.23 Collapse scheme for De La Hire. 28
2.24 Meridians and parallels; crack detected in the dome of St. Peter's (Vanvitelli, 1743). 30
2.25 Micromodeling technique (Gatta, 2019). 33

2.26 Micro-modeling of a high (a) and a law (b) wall, from Oliveira and Lourenço (2004). 34
2.27 Sacco and Toti (2010): (a) damaging states of brick-mortar interface and (b) detailed micromodeling of a masonry arch. 35
2.28 Macro-modeling technique: masonry as a homogeneous material. 35
2.29 Ponte delle Torri: Spoleto: (a) real structure and (b) FE model used by Addessi et al. (2020b). 36
2.30 Ciocci et al. (2018): FE model of the Ica Cathedral in Peru. . . . 37
2.31 From Leonetti et al. (2018):schematic representation of the adaptive model refinement strategy: (a) initial coarse mesh composed of homogenized macro-elements; (b) intermediate multi-level mesh with partial structural damage; (c) final multi-level mesh at incipient collapse. 39
2.32 Examples of RVEs adopted for the derivation of homogenized masonry mechanical properties, (a) Anthoine et al. (1995), (b) Cavalagli et al. (2011), (c) Taliercio (2014), (d) Stefanou et al. (2015) and (e) Milani (2011); (D'Altri et al., 2019). 40
2.33 Multiscale technique: transition between macro and microscale. . 40
2.34 From Addessi et al. (2015): (a) equivalent frame scheme and (b) distribution of the plastic hinge. 42
2.35 From Caliò et al. (2012): (a) equivalent mechanical scheme and (b) example of damage scenarios 43
2.36 From Mamaghani et al. (1999): Failure mode of a masonry arch. 44
2.37 Adapted from Lourenço (2001): comparison between limit and nonlinear analysis for a masonry arch loaded at quarter span with point load. 45
2.38 From Baggio and Trovalusci (2000): (a) masonry textures and collapse multiplier, (b) collapse mechanism and collapse multiplier of walls in "opus poligonale" subjected to inclinated body force. . . 47
2.39 Damage mechanics concepts: (a)RVE,(b) effective area $\tilde{A}$. 50
2.40 From Jirásek (2011): (a) Schematic representation of smeared crack model as an elastic unit coupled in series to a crack unit, (b) local coordinate system aligned with the crack. 52

2.41 (a) Uniaxial tension experiment with ductile metals and (b) Uniaxial tension mathematical model (de Souza Neto et al., 2011). . 55
2.42 Bar under uni-axial tension (Jirásek, 2002). 58
2.43 (a) Stress-strain diagram with linear softening and (b) two strain values corresponding to the same stress level (Jirásek, 2011). . . . 58
2.44 Fan of possible post-peak branches of the load-displacement diagram (Jirásek, 2011). 59
2.45 Effect of mesh refinement on the numerical results: load-displacement diagrams and strain profiles (Jirásek, 2011). 60
2.46 Representative volume of material used for nonlocal strain average (Bažant and Jirásek, 2002). 63

3.1 Mortar joints: local axis x_T -x_N. 67
3.2 Mortar joints: local axis x_T -x_N 68
3.3 Mortar joints: constitutive laws for mode I and mode II. 70
3.4 Out-of-plane test set-up. (Bellini et al., 2018). 75
3.5 Elasto-plastic with hardening constitutive law for FRCM. 77
3.6 Geometry of the masonry wall reinforced with FRCM composite materials (Addessi et al., 2018). 77
3.7 Global response curves for masonry wall reinforced with FRCM (adapted from Addessi et al. (2018)). 78
3.8 FE brick and mortar discretization for (a) unreinforced and (b) reinforced numerical model of the masonry walls (Bellini et al., 2018). 78
3.9 Distribution of the damage variable D with the proposed micromechanical model in the unreinforced wall (a) Mid - height deflection = 5 mm, (b) Mid - height deflection = 15 mm (c) damage color bar. 79
3.10 From (Addessi et al., 2018): masonry wall reinforced with FRCM composite materials: comparison of the vertical strains obtained with the micromechanical and multiscale models. 80
3.11 Four-point out-of-plane bending test of the masonry wall: specimen geometry (Van der Pluijm, 1999). 81

3.12 FE brick and mortar discretization for the numerical model of the masonry wall Van der Pluijm (1999). 82
3.13 Adapted from Addessi et al. (2017), four-point out-of-plane bending test of the masonry wall: maximum moment m per unit width versus curvature K. 83
3.14 Circular arch tested by Oliveira et al. (2010): (a) Construction of the arch and (b) geometry and loading condition. 85
3.15 Comparison between numerical and experimental force-displacement response curves. 86
3.16 Circular arch tested by Oliveira et al. (2010): (a) experimental and (b) numerical failure mechanisms (FH = 'flexural hinge'). 87
3.17 Effect of the t/R ratio: (a) load-displacement curves, (b) maximum load and failure mechanism (FH = 'flexural hinge', SH = 'shear hinge'). 89
3.18 Distribution of the damage variable D for different values of t/R at the end of the analyses: (a) $t/R = 0.13$, (b) $t/R = 0.20$, (c) $t/R = 0.27$ and (d) $t/R = 0.33$. (FH = 'flexural hinge', SH = 'shear hinge'). 90
3.19 Distribution of the damage variable D for arch with with $t/R = 0.33$ at different values of the applied displacement s: (a) $s = 0.5\,\text{mm}$ and (b) $s = 0.7\,\text{mm}$. (FH = 'flexural hinge', SH = 'shear hinge') 90
3.20 Material parameters effect: influence of the tensile strength. . . . 92
3.21 Material parameters effect: influence of mode I fracture energy. . 92
3.22 Distribution of the damage variable D at the end of the analyses for $t/R = 0.07$ and different values of g_{cI}: (a) $g_{cI} = g_{cI,r}/4$, (b) $g_{cI} = g_{cI,r}/2$ and (c) $g_{cI} = g_{cI,r} \times 2$. 93
3.23 Distribution of the damage variable D at the end of the analyses for $t/R = 0.27$ (a,c,e) and $t/R = 0.33$ (b,d,f) and different values of μ: (a,b) $\mu = 0.5$, (c,d) $\mu = 0.65$ and (e,f) $\mu = 0.7$. 94

4.1 Failure surface in principal stress space. 99

4.2 Masonry stress-strain law: tensile and compressive law for TSRC model. 100
4.3 Constant shear retention for TSRC model. 100
4.4 Masonry stress-strain law: tensile and compressive law for CP model. 105
4.5 Uni-axial test 107
4.6 Uni-axial stress strain diagram $\sigma_1 - \varepsilon_1$. 107
4.7 Uni-axial stress strain diagram $\sigma_1 - \varepsilon_1^p$. 107
4.8 Cohesion hardening function. 108
4.9 Masonry stress-strain law: tensile and compressive law for MCP model. 109
4.10 Experimental campaign: setup from Anthoine et al. (1995). . . . 110
4.11 Geometry of the (a) high and (b) low panel. 111
4.12 Comparisons between experimental and numerical (TSRC and CP) force-displacement response curve under monotonic loading: (a) high (slender) panel, and (b) low (squat) panel. 112
4.13 Cyclic displacementet history applied to high (a) and low (b) panel. 113
4.14 Comparison between experimental and numerical (TSRC) force-displacement response curve under cyclic loading :(a) high and (b) low panel. 114
4.15 Comparison between experimental and numerical (CP) force-displacement response curve under cyclic loading :(a) high and (b) low panel. . 115
4.16 Crack patterns for the high (slender) wall: (a) TRSC s=2 mm; (b) TRSC s=12 mm;(c) CP s=2 mm; and (d) CP s= 6 mm. 116
4.17 Crack patterns for the low (squat) wall: (a) TRSC s=2 mm; (b) TRSC s=7 mm;(c) CP s=2 mm; and (d) CP s= 4 mm 116
4.18 Comparison between experimental and numerical (MCP) force-displacement response curve under cyclic loading :(a) high and (b) low panel. 117
4.19 Comparison between experimental and numerical (MCP and CDP) force-displacement response curve under cyclic loading :(a) high and (b) low panel. 118

4.20 Ispra (a) high and (b) low wall: crack distribution, at the end of the analyses, for the MCP model (first column) implemented in DIANA code (DIANA, 2019), distribution of the damage for the CDP model (second column) implemented in FEAP code (Taylor, 2017) and experimental failure paths (third column) from Anthoine et al. (1995). 119

5.1 Crack stresses, relative displacements and local coordinate system of the crack (adapted from Sena-Cruz (2005)). 122
5.2 Rankine yield surface in the 2D principal stress space. 125
5.3 Linear tension softening. 127
5.4 Linear tension softening. 128
5.5 Variable cross section beam: geometry and load condition. 130
5.6 Non regularized load-displacement curves. 131
5.7 Fracture energy regularization using Rots' method (Rots, 1988): load-displacement curves. 132
5.8 Explicit values of the equivalent crack length for quadrilateral and triangular linear elements related to different crack patterns (adapted from Oliver (1989)). 133
5.9 Fracture energy regularization using Oliver' method (Oliver, 1989): load-displacement curves. 133
5.10 Crack strain patterns with fracture energy regularization for u = 0.1 *mm*: (a) mesh 25 FEs (b) mesh 50 FEs and (c) mesh 100 FEs. 134
5.11 Nonlocal integral regularized smeared-crack model: load-displacement curves. 135
5.12 Crack strain patterns with nonlocal integral regularization for u = 0.1 *mm*: (a) mesh 25 FEs (b) mesh 50 FEs and (c) mesh 100 FEs. 136
5.13 Weak element beam: geometry and load condition. 137
5.14 Non regularized load-displacement curves. 137
5.15 Fracture energy regularization using Rots' method (Rots, 1988): load-displacement curves. 138
5.16 Fracture energy regularization using Oliver' method (Oliver, 1989): load-displacement curves. 139

5.17 Nonlocal integral regularized smeared-crack model: load-displacement curves. 139
5.18 Crack strain patterns with fracture energy regularization for u = 0.1 mm: (a) mesh 25 FEs (b) mesh 50 FEs and (c) mesh 100 FEs. 140
5.19 Crack strain patterns with nonlocal integral regularization for u = 0.1 mm: (a) mesh 25 FEs (b) mesh 50 FEs and (c) mesh 100 FEs. 141

List of Tables

3.1 Computational procedure for mortar. 73
3.2 Damage-friction solution procedure 74
3.3 Material parameters for the bricks and mortar of the masonry wall. 76
3.4 Mechanical parameters for the reinforcing layer of the masonry wall reinforced with FRCM. 76
3.5 Four-point out-of-plane bending test of the masonry wall: material parameters for mortar. 81
3.6 Four-point out-of-plane bending test of the masonry wall: material parameters for bricks. 82
3.7 Elastic material parameters adopted for bricks and mortar. 86
3.8 Damage material parameters adopted for mortar. 86

4.1 Mechanical parameters adopted for TSRC and CP models. 110
4.2 Additional mechanical parameters adopted for CP models. 110

5.1 Computational procedure for the model. 129
5.2 Mechanical parameters adopted for the models. 130
5.3 Geometry parameters adopted for the models. 130
5.4 Mechanical parameters adopted for the models. 135
5.5 Geometry parameters adopted for the models. 135

Chapter 1

Introduction

1.1 Motivations and historical background

Masonry is the oldest building material that is still currently utilized in building activity. The construction technique, consisting of placing stone or brick units on top of each other laid dry or bonded with mortar, has revealed itself as successful, justified by its simplicity and durability. Despite the simplicity associated with building in masonry, the several advantages that the material offers, such as economy, high fire resistance, and recyclability, the analysis of the mechanical behavior of masonry constructions remains a true challenge. However, as known, a complex mechanical response emerges due to the heterogeneous material nature, particularly the masonry material exhibits distinct directional properties due to the mortar joints, which act as planes of weakness. Consequently, masonry structures present complex mechanical behavior, typically nonlinear.

Structures may be classified as historical when they become part of our built heritage (Oliveira, 2003). In European countries, the preservation of masonry architectural heritage is a felt concern. The conservation of historical structures has been received particular attention since they are among the principal components of the historic environment. Fascinating landscapes are characterized by a large presence of masonry structures that have become part of the country cultural identity (see Figure 1.1). This justifies the lively interest in developing efficient computational tools to assess the structural capacity of masonry build-

(a)

(b)

Figure 1.1: Some Italian masonry landscapes: (a) Ponte delle Torri, Spoleto (b) Civita di Bagnoreggio.

ings. Indeed, the analysis of historical masonry presents an important trouble. However, they often show significant structural vulnerability and have been seriously damaged by natural disasters such as earthquakes, mainly due to the poor material properties and often inadequate structural configurations. At structural level, masonry buildings exhibit good resistance to vertical loads while performing badly against horizontal actions. Figure 1.2 shows the main collapse mechanisms distinguished based on the earthquake's effects on masonry structures, namely crumbling, out-of-plane and in-plane failures. When proper masonry textures are adopted, limiting the crumbling phenomenon, it was widely estimated that out-

of-plane collapse mechanisms are the most frequent. The walls normally loaded in their plane undergo flexure and, when internal stresses exceed the material strength, crack patterns develop with directions depending on the edge restraint positions. Some experimental tests on uncracked masonry panels loaded out-of-plane can be found in Griffith et al. (2007). In-plane failure can involve sliding of mortar joints, diagonal cracking bands or damaged zones located at the corners of the panels, depending on geometry, loading and boundary conditions (Anthoine et al., 1995).

(a) Masonry crumbling (b) Out-of-plane failure (c) In-plane failure

Figure 1.2: Failure mechanisms of masonry structures (Gatta, 2019).

Many ancient and historical masonry buildings are characterized by the presence of arches and vaults. In particular the arch is a fundamental constructive element having both load-bearing and ornamental function. The analysis of the earthquake's effects has led to identify typical collapse mechanisms of unreinforced masonry arches, that is the formation of nonlinear flexural hinges and voussoirs sliding (see Figure 1.3).

Other mechanisms were studied and are present in the literature, but these two are certainly considered the main ones. The flexural mechanism was largely investigated conversely from the sliding, which in some situations is predominant respect to the flexural one. Figures 1.4 and 1.5 show some famous examples of artistic and cultural heritage, where sliding mechanism is strongly manifest.

Research in historical masonry constructions is essential to understand their specificity, with the development of computational tools and consistent constitutive models to reproduce the experimental outcomes. Many methods were proposed to assess the structural capacity of masonry constructions (see Chapter 2.2).

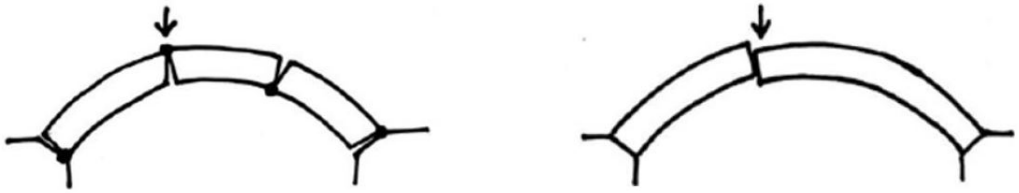

(a) Four-hinge mechanism (b) Sliding

Figure 1.3: Failure mechanisms of masonry arch: (a) Four - hinge mechanism and (b) sliding; (Melbourne et al., 2007).

(a) (b)

Figure 1.4: (a) The Colosseum and (b) a detail of a sliding mechanism on one of its arches.

The choice of the adopted methodology depends on several factors: searched information, computational cost, and available input data. Often simple aspects as geometry data or characterization of the material mechanical properties are difficult to retrieve. Thus, identifying a unique model with general validity represents a hard, perhaps unrealistic task.

Finite element approaches appear as attractive tools to describe the evolution of nonlinear mechanisms evolving in masonry material. Models based on

(a) (b)

Figure 1.5: (a) Mausoleum of Teodorico and (b) a detail of a sliding mechanism on one of its arches.

continuum damage and smeared crack well describe the degrading effects using the consolidated principles of solid mechanics theory (see Section 2.3). Usually, damage and crack models are combined with plasticity formulations, with the purpose to also introduce the effects of irreversible strains and, thus, provide a more realistic description of the material mechanical response in terms of hysteretic dissipation properties (see Chapter 4).

1.2 Objectives and scopes

The aim of this study relies on the above considerations and is focused on two different scales of modeling and analysis of the possible failure mechanisms on the masonry structures, through finite element models that well represent the masonry response. The main objectives can be summarized as follows:

- Development of a micromechanical model suitable for capturing the strongly nonlinear behavior of the complex structures as unreinforced masonry arches, to investigate their collapse mechanisms. Based on an existing damage-

plastic constitutive law, a new user finite element is implemented to numerically reproduce the behavior of masonry structures;

- Validation and enrichment of existing smeared crack macromechanical models implemented in finite element codes widely spread in the scientific community. A modified version of a literature model is formulated to overcome some shortcomings of reproducing the response of masonry structures;

- Strain localization due to the softening: mesh-adjusted softening modulus (crack band approach) and regularized softening models. A fixed smeared crack model is implemented. Two different techniques are used to avoid the well-known mesh-dependency drawback emerging in cases of strain-softening: fracture energy and nonlocal integral regularization. Analyses of simple structures are presented to prove the robustness and stability of these two approaches.

1.3 Organization of the thesis

The thesis is organized as follows:

- Chapter 2 offers the main aspects regarding the state of the art correlated with the topic discussed subsequently. In the first section, an overview of the principal characteristics of the material masonry is given to identify recurrent features of the mechanical response. A review of the structural behavior and the collapse mechanisms of two main structural elements, walls and arches, is later presented. In the second section, the available modeling strategies for masonry structures are described, emphasizing the finite element (FE) approach. In the third section, the available literature material models based on continuum damage, smeared crack and plasticity are described to highlight the fundamental aspects and drawbacks, respectively. Lastly, the strain-softening phenomenon is defined, and the so-called mesh-dependency problem is addressed. Two possible solutions, adopted in this thesis, known as fracture energy and nonlocal integral regularization technique, are explained.

- Chapter 3 presents a new damage-plastic model for the micromechanical analysis of 2D masonry structures. First, the existing constitutive law is illustrated and the main aspects related to the finite element implementation are presented. A comparison between numerical and experimental outcomes are proved for two masonry walls to validate the model. Particularly, the complexity of the arch mechanics, proved by many experimental campaigns, led the scientific community to develop efficient and accurate numerical models. Indeed, the structural response of unreinforced masonry arches submitted to asymmetrical vertical concentrated loads is studied, by analyzing both global force-displacement response curves and collapse mechanisms. Numerical results are validated by comparison with experimental ones, and parametric numerical studies investigate the influence of geometry and material mechanical parameters. The finite element model appears to be a suitable and efficient tool to accurately describe evolution of degrading mechanisms and capture the typical collapse modes of arches.

- Chapter 4 proposes a modified version of an existing smeared crack model motivated by the investigation of the use of macro-modeling technique based on smeared crack model, that showed some limitations when analyzing the behavior of masonry structures subjected to in-plane cyclic loading. A suite of numerical simulations is performed referring to an experimental campaign on two masonry panels. The results obtained from the modified model better correlate with the experimental output.

- Chapter 5 moves towards the exploration of the regularization technique. A fixed smeared crack model is formulated. Two different approaches are implemented to avoid the well-known mesh-dependency drawback emerging in strain-softening cases: fracture energy and nonlocal integral regularization. Analyses of simple structures are presented to prove the robustness and stability of these two approaches. A comparison between them is shown.

- Chapter 6 summarizes the main contributions and offers overall concluding remarks.

Chapter 2

State of the art

2.1 Historical masonry constructions

Masonry is an ancient building material that has been widely used during history, and is still used nowadays. Being the main structural technique adopted in historical construction, a broad understanding of masonry mechanical behavior is fundamental for the preservation and conservation of our cultural heritage, first, section 2.1.1 introduces the principal features of the masonry material. In section 2.1.2, a review of the structural behavior and collapse mechanisms of two main masonry structural elements, walls and arches, is subsequently given. In particular the main historical developments of arches are revised, from the constructive point of view.

2.1.1 Mechanical behavior of masonry material

Masonry is a heterogeneous material that can be decomposed into three components, that is mortar, units and interfaces (representing the mechanical interaction between mortar and units). A large number of arrangements can be accomplished with these three components, generated from their different combinations. Stones and bricks have been used as units that can be joined together using mortar or just by mere superposition. Based on stone combination in the construction and degree of refinement in the surface finish, stone masonry can be broadly categorized as shown in figure 2.1.

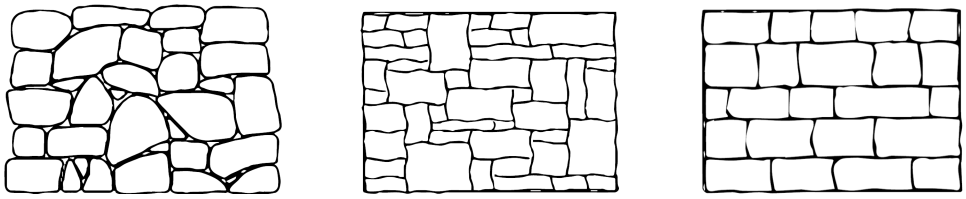

(a) Rubble (b) Ashlar (c) Coursed ashlar

Figure 2.1: Stone masonry textures (Lourenço, 1998).

Several types of brick masonry can be found, depending on the stretchers and header arrangement. Figure 2.2 shows some examples of the most widespread textures.

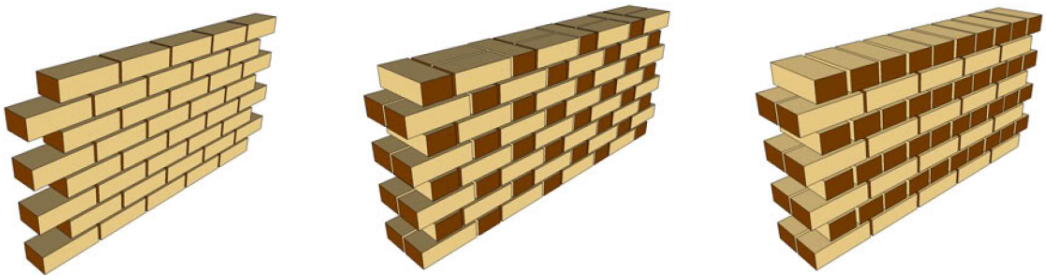

(a) Running bond (b) Flemish bond (c) English bond

Figure 2.2: Most common brick masonry textures.

Despite many typologies, the overall mechanical behavior presents several characteristic features. Indeed, the characterization of ancient structures and materials, used by advanced numerical models, is an arduous task. Nevertheless, experimental investigations have been conducted to carry out detailed information about the material properties that can be adopted and used to design procedures based on numerical models. Here an overview of recurrent features will be given, analyzing the behavior of the composite material. A more detailed description of the mechanical properties of the three components, in particular mortar and units and unit-mortar interface, that is often regarded as the weakest component of masonry composite material, can be found in several references (Drysdale et al., 1982; McNary and Abrams, 1985; Van der Pluijm, 1993, 1997; Van der Pluijm et al., 2000). Tensile and shear responses were largely investigated by pointing

out peculiar characteristics in terms of strength, fracture energy, and stress-strain relationship, which strongly affect the composite response.

2.1.1.1 Uni-axial behavior of composite material

From a phenomenological point of view, masonry can be considered as a composite material with an overall orthotropic behavior. The different elastic mechanical properties of mortar and units and their geometrical arrangement govern the orthotropy of the elastic response. Moreover, mortar joints typically act as weak planes, and the structural response is heavily dependent on their orientation. The uni-axial compressive strength of masonry in the direction normal to the bed joints has been observed as the most significant structural material property. Several authors (McNary and Abrams, 1985) used uni-axial compressive tests to investigate strength, stiffness, and deformation capacity of masonry. The different strengths and deformable characteristics of units and mortar are precursors of failure, as proved by the pioneering work of Hilsdorf (1969). For instance, considering mortar softer than bricks, as usually happens, a tri-axial compression state in the mortar and a combined compression/bi-axial tension in the brick occur under uni-axial compressive load normal to bed joints, see Figure 2.3. Thus, the lateral mortar expansion is restrained by bond and friction between brick and mortar. Consequently, vertical cracks develop in the units leading to the specimen collapse, see Figure 2.3. Because of the material anisotropic nature, the strength and failure mode varies with various bed joints' inclinations (Page, 1981, 1983). If the loading direction is parallel to bed joints, the bed joints' splitting in tension transpires. For average inclinations, a mixed mechanism is met, see Figure 2.4

Masonry tensile strength is strongly dependent on both mechanical properties of the constituent materials and orientation of the applied stresses concerning bed joint direction. In general, for tensile stress normal to bed joints, tensile strength can be considered equal to tensile bond strength between mortar and units. On the contrary, failure is associated with excessive stress in the bricks when low strength units characterize masonry, and high tensile bond strength is considered. For tensile loading parallel to the bed joints, a complete test program was set-up by Backes (1985). The author examined masonry wallets under direct tension,

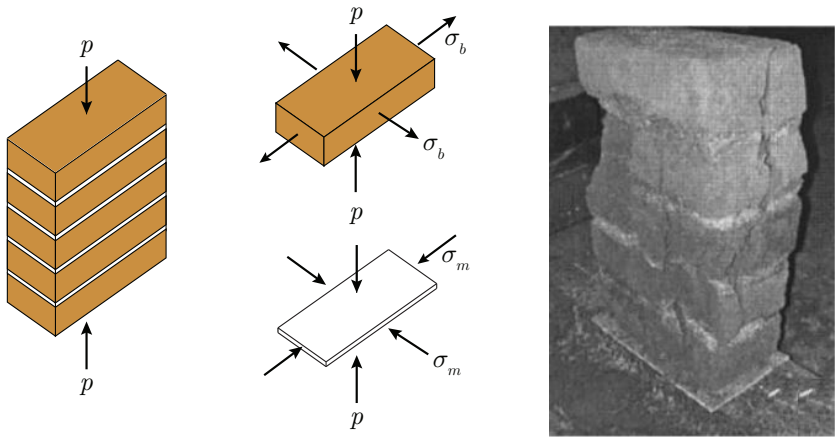

(a) (b)

Figure 2.3: Compressive behavior for uni-axial load normal to bed joints: (a) state of stress in masonry constituents and (b) failure mode of a masonry prism.

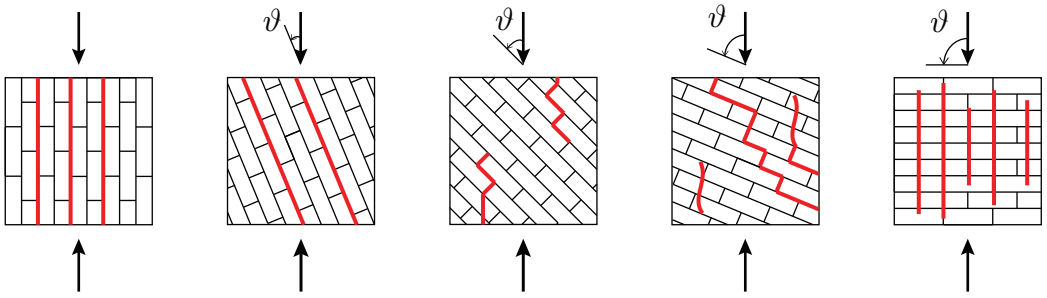

(a) $\theta = 0$ (b) $\theta = 22.5$ (c) $\theta = 45$ (d) $\theta = 67.5$ (e) $\theta = 90$

Figure 2.4: Page (1981, 1983): local state of stress in masonry prisms under uni-axial compression with different orientation θ from the bed joint direction.

and observed that tension failure was influenced by the type of the mortar and masonry units. For more durable mortar and weaker masonry units, the tension cracks moved along the head mortar joints and through the center of the bricks as shown in Figure 2.5 (a). For weak mortar joints and strong masonry units, zigzag paths appeared, see Figure 2.5 (b).

Figure 2.6 shows different modes of failure observed by Page (1983) on solid clay units masonry walls subjected to uni-axial tension. As can be seen, for intermediate inclinations of the bed joints, the failure is concentrated at joints.

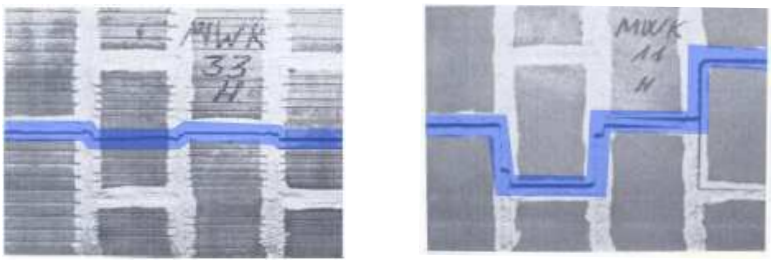

(a) (b)

Figure 2.5: Failure modes of masonry walls under direct tension: (a) cracks passing along mortar and bricks and (b) zigzag type for load parallel to bed joint orientation, from Backes (1985).

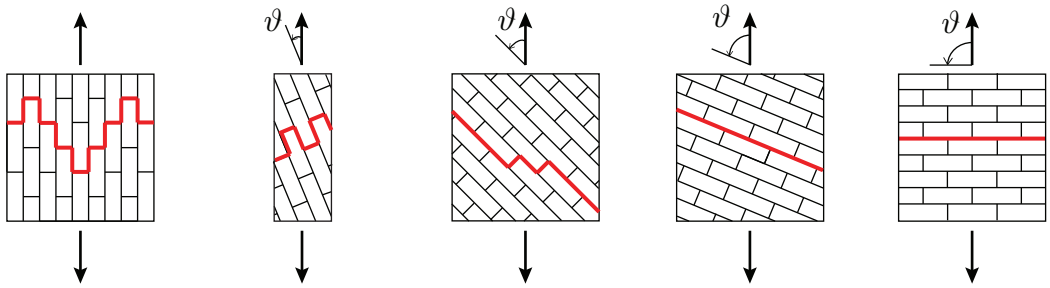

(a) $\theta = 0$ (b) $\theta = 22.5$ (c) $\theta = 45$ (d) $\theta = 67.5$ (e) $\theta = 90$

Figure 2.6: Page (1983): local state of stress in masonry prisms under uni-axial tension with different orientation θ from the bed joint direction.

The shear response of masonry joints is a complex task; it has been observed that it heavily depends on the test set-up's ability to generate a uniform state of stress in the joints. Different test configurations are possible, and details can be found in Van der Pluijm (1993, 1998), Hofmann and Stockl (1986), Atkinson et al. (1989). It is noted that the shear strength increases with the confining compression stress because of the frictional behavior of masonry. Moreover, the real behavior of the mortar joint is generally non-associative. A recurrent behavior is the reduction of dilatancy angle both with increasing relative tangential displacement, as a consequence of progressive smoothing of asperities, and also under the action of growing normal stresses.

Quasi-brittle materials like masonry typically show softening behavior, com-

monly attributed to material heterogeneity, due to different phases and material defects, like flaws and voids (Lourenço, 1997). Strain-softening is defined as a gradual decrease of the mechanical resistance under a continuous increase of deformation imposed on a material specimen or structure (Lourenço, 1996). Figures 2.7, 2.8, 2.9 show characteristic stress-displacement diagrams for quasi-brittle materials in uni-axial tension, uni-axial compression, and pure shear, respectively. The area under the σ - δ is the fracture energy associated to mode I, denoted by G_{fI} and G_{cI}, for tension and compression, respectively. Shear behavior is governed by the mode II fracture energy G_{fII}, defined by the area under the τ - δ diagram. A more detailed description will be give in section 2.3.

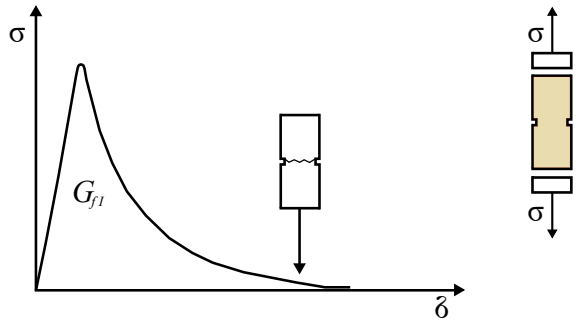

Figure 2.7: Typical behavior of quasi-bittle materials under tensile loading and definition of mode I fracture energy G_{fI}.

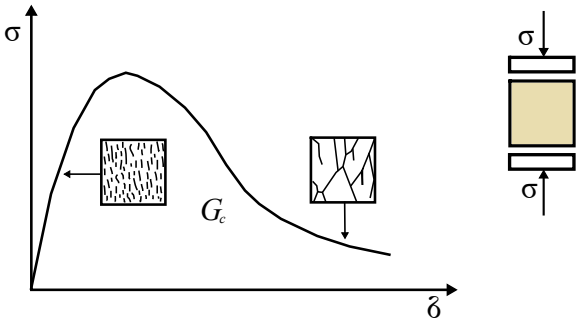

Figure 2.8: Typical behavior of quasi-bittle materials under compressive loading and definition of fracture energy G_c.

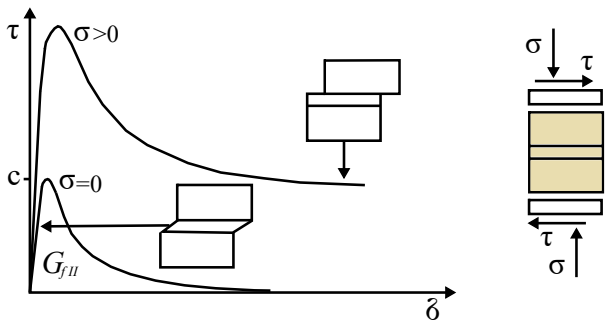

Figure 2.9: Behavior of masonry under shear and definition of mode II fracture energy.

2.1.1.2 Bi-axial behavior of composite material

Due to the material anisotropy, masonry strength depends heavily on the orientation of the principal stresses with respect to the material axes defined by bed and head joints directions. Therefore, the constitutive behavior of masonry under bi-axial states of stress cannot be completely described in the basis of the constitutive response under uni-axial loading conditions (Lourenço, 1996). The response under bi-axial states is relevant to fully characterize masonry mechanical behavior. The most complete experimental research regarding the characterization of masonry bi-axial behavior was done by Page (1983), as already mentioned. The tests were carried out with half-scale solid clay units. Both the orientation of the principal stress ratio considerably affected the failure mode and strength.

Figure 2.10 shows the experimental test data in terms of bi-axial strength for different value of θ, defined as the rotation angle between the principal stresses and the material axes. Anisotropic behavior is considerably proved, as tensile and compressive strengths parallel and normal to bed joints differed. Furthermore, increasing resistance was obtained for bi-axial compressive loads. Different failure modes occurred: cracking and sliding in bed and/or head joints for uni-axial compression and collapse for cracking in the joints alone or combined bricks and joint failure for tension-compression load. In bi-axial compression, failure occurred by splitting of the specimen at mid-thickness, in a plane parallel to the external free surfaces, independent on the orientation of the principal stresses. Other researchers have been conducted the bi-axial tests, see Ganz and Thürlimann

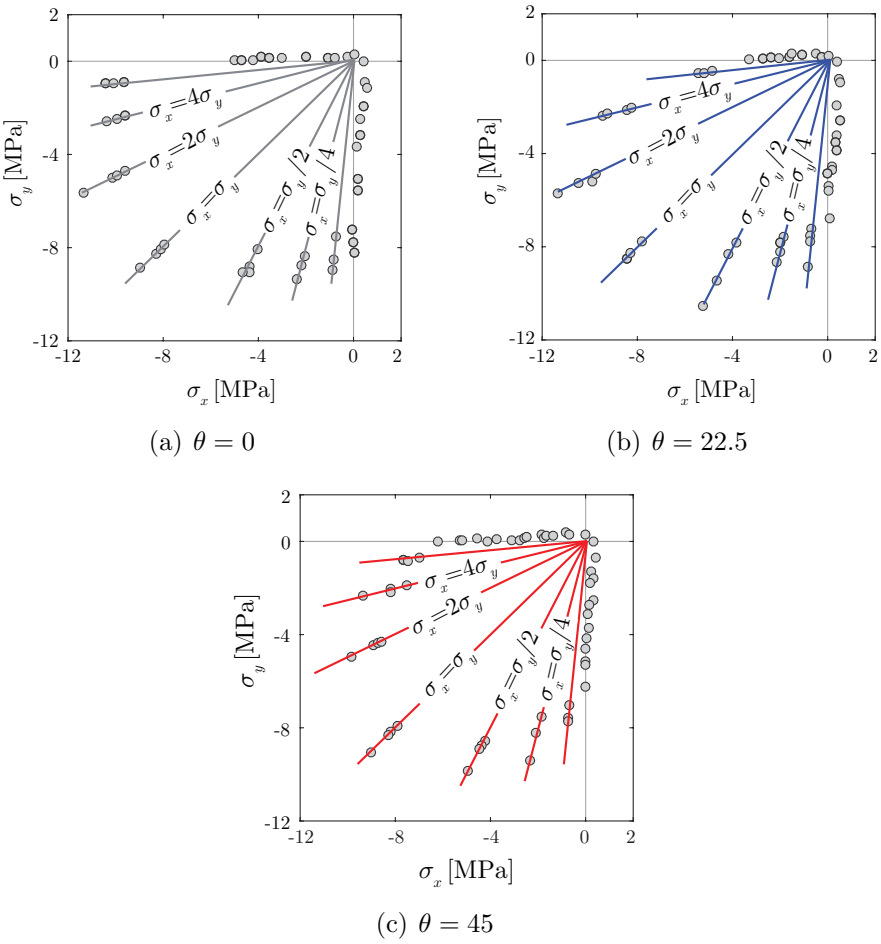

(a) $\theta = 0$ (b) $\theta = 22.5$

(c) $\theta = 45$

Figure 2.10: Masonry bi-axial strength: experimental results of Page (1981, 1983) for (a) $\theta = 0°$, (b) $\theta = 22.5°$and (c) $\theta = 45°$.

(1982) for hollow clay units masonry, Naraine and Sinha (1991) for half-scale clay brick specimens and Alshebani and Sinha (2000) for a calcium-silicate brick masonry.

2.1.2 Structural elements: walls and arches

In this section, a brief introduction about the most widely spread masonry structural elements, like walls an arches and their failure mechanisms is given. In particular, the development of the architecture of the arch is described, and subsequently a historical review about their collapse mechanisms is reported (Heyman

and Jacques, 1998).

2.1.2.1 Walls and damage mechanisms

As far as walls are concerned, each geographical region and period in history presented various building methods. Masonry walls can be classified into load-bearing ones, supporting vertical loading and sustaining the vertical load of buildings, and shear walls, providing in-plane strength and contributing to resist the lateral forces caused by wind and earthquake. In the following section the different types of walls are shown, considering the type of masonry that composes it, in particular stone and brick masonry textures as figures (2.1 and 2.2) show, respectively. Stone masonry was widely used by Egyptians and by Incas in Peru. Initially, their constructions were built with irregular masonry. It is worth noting how the not aligned courses, both vertical and horizontal, led the walls with significant stone interlocking, giving an intrinsic strength against horizontal actions. Nevertheless, it is only with Classic Greek builders that masonry assumed modern aspect: fine ashlar stones quite dressed in parallelepiped shape with no mortar joint. As a general consideration, the more homogeneity of the masonry and the exclusion of the bending stresses on the blocks led to a more efficient wall, also with a smaller thickness (Roca et al., 2019). The classification of stone masonry, due to its intrinsic complexity, deserved particular attention. The local and global behavior of masonry walls is influenced by the type and quality of materials, the presence of connections through the leaves, the shape and dimension of the elements, the thickness of mortar joints and the constructive techniques (Binda et al., 1999). Research on the morphology of stone masonry wall sections in Italy was started in the early 1990s (Abbaneo et al., 1993; Binda et al., 2000). Abbaneo et al. (1993) and Binda et al. (2003) distinguished stone masonry walls into four groups, corresponding to one leaf, two leaves, three leaves and dry joint walls (Figure 2.11).

During the same years, Giuffrè (1993a) also investigated the mechanical behavior of stonework masonry typologies. As a result of the investigation and typology classification, the masonry typologies were summarized in the form of a report. The presence of some features, including the connection elements, is a crucial pa-

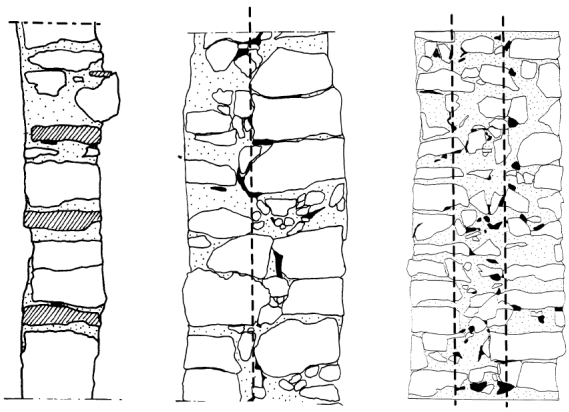

Figure 2.11: Typical stone masonry sections: one, two, and three leaves Binda et al. (1999).

rameter for evaluating the mechanical behavior of walls. Other authors (Da Porto et al., 2003) investigated the problems related to stone masonry walls classification. Accordingly, it was reported that the most frequently-observed stone masonry typology is made of two or three leaves, which are not interconnected with the outer leaves made of irregularly shaped stones bonded in sub-horizontal courses. The average thickness of the observed walls is about 50 cm. After the severe earthquake in Italy in 2009, Cardani and Binda (2013) suggested a set of guidelines for the characterization of the masonry quality for on-site visual inspection. Case study masonry walls were selected from several regions. Masonry walls are classified with regards to the following six factors: the type of masonry units, the shape of the stone elements (regular or irregular), the thickness of the horizontal mortar joint, the horizontality of the courses, the presence of wedges and the type of cross-section of the masonry wall (one or multiple leaves). In conclusion, the authors declared that the visual inspection of the texture does not adequately identify masonry quality. For a better understanding of masonry properties, in-situ and laboratory tests are needed.

Bricks were first hurled around 3500 BC in Mesopotamia, present-day Iraq, one of the world's high-risk seismic areas. From Roman aqueducts and public buildings to the Great Wall of China, from the domes of Islamic architecture to the early railway arch bridges, from the first 19th century tall American buildings to the 20th-century nuclear power plants, bricks have been utilized as a structural

material in all applications of construction and civil engineering (D'Ayala, 2004). As discussed earlier, according to the way that brick is laid and how the brick facing is oriented in the finished wall, different patterns may be fixed. Brick masonry walls are commonly composed of several layers or two outer leaves with a cavity filled with rubble and their characteristic depends on two factors (D'Ayala, 2004). As for the first factor, integrity and shear resistance of brick masonry walls is affected by the extent and quality of the bond between mortar and bricks. The second factor is the connection between the leaves. This is ensured by headers, consisting of bricks located through the wall at regular intervals. Old brick masonry usually has thick sections (often more than 600 mm) with a much less homogeneous distribution of the bricks in the section than in modern ones (Binda and Saisi, 2001). In some cases, only the outer leaf is composed of regular bricks, while the internal part is made of pieces of bricks and large mortar joints. The thickness of joints is usually much lower than that of the brick in a ratio 1-2/5. Although, this was not the case of late Roman architectures and Byzantine constructions where the mortar joints were much thicker than before. From a study carried out on Milan Roman walls and Ravenna Byzantine walls the following classification could be made (Figure 2.12): (I) solid walls with thin joints, (II) solid walls with thick joints, (III) solid walls with multiple leaves (with different thickness of the leaves) (Binda and Saisi, 2002).

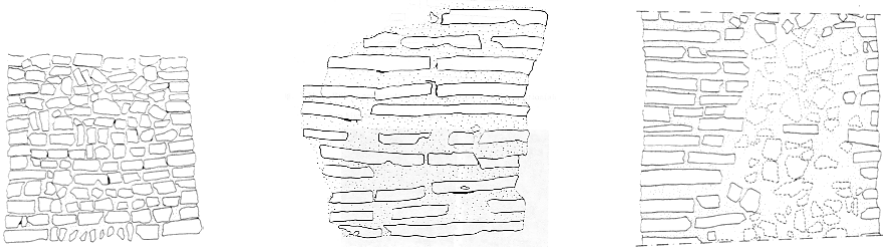

(a) St Giovanni in Conca, Milan

(b) St Michele in Africisco, Ravenna

(c) St Simpliciano Basilica, Milan

Figure 2.12: Examples of brick masanry section Binda and Saisi (2002).

Rosa Valluzzi et al. (2009) gave a classification of brick masonry walls of different structural typologies of historical buildings. The authors sorted out the masonry walls in terms of masonry typology (type of brick) and thickness.

Two significant collapse mechanisms can quite describe damage of masonry walls, known as out-of-plane and in-plane. As described by Giuffrè (1993a), the first occurs when connections between orthogonal walls and between walls and floors are particularly weak. This is frequently the case in existing stone masonry buildings without tie rods, with a lack of interlocking at the connection of intersecting walls, the presence of supported wooden floors, and thrusting roofs. If proper devices improve connections and the masonry panels behavior involves an effective overall building configuration, in-plane mechanisms govern the response. According to the goal of this research, attention is focused on the in-plane collapse mechanisms, instead a comprehensive review of out-of-plane mechanisms can be found in Sorrentino et al. (2017). Remarks of seismic damage of masonry walls and experimental laboratory tests (Anthoine et al., 1995) proved that masonry panels subjected to in-plane loading show two common behavior types with distinct failure modes associated, flexural and shear collapse mechanisms (Magenes and Calvi, 1997), respectively, see Figure 2.13. The first can show two different failure configurations, mostly depending on the relation between the applied vertical load and the material compressive strength. Suppose the applied vertical load is high to compressive strength. In that case, the panel is characterized by a widespread damage pattern, with sub-vertical cracks oriented towards the more compressed corners. This failure is known as crushing. Conversely, suppose the applied vertical load is low to compressive strength. The horizontal load allows tensile flexural cracking at the corners, and the panel starts to behave as a nearly rigid body rotating about the toe. This failure is known as rocking. As well, the shear behavior presents two different failure configurations that can develop in sliding shear or diagonal crack. Sliding, usually on a horizontal bed joint plane, occurs when the development of flexural cracking at the corners reduces the resisting section. Instead, the formation of a diagonal crack develops at the center of the panel and then propagates towards the corners.

Many experimental tests attempted to investigate the influence of several parameters that influence the different failure modes activation, recognizable as the wall geometry, boundary conditions, acting axial load, mechanical characteristics of masonry constituents, and the masonry geometrical characteristics. It is worth pointing out that it is not always easy to distinguish the occurrence of a spe-

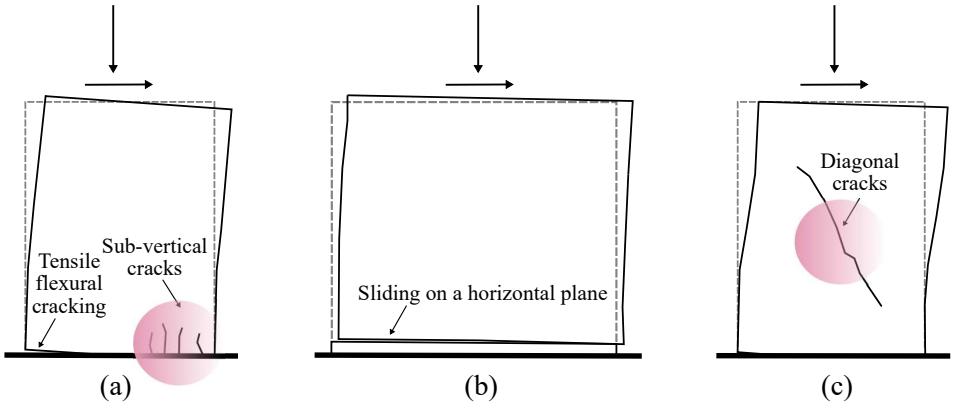

Figure 2.13: Typical failure modes of masonry walls: (a) rocking; (b) sliding shear failure; and (c) diagonal cracking (adapted from Calderini et al. (2009)).

cific type of mechanism, since many interactions may occur between them. Many studied were done to understand in which case one mode can prevail (Giuffrè, 1993b; Magenes and Calvi, 1997; Lourenço et al., 2005). In general, as addressed by Calderini et al. (2009), it was assessed that rocking tends to win in slender walls, while bed joint sliding tends to occur only in very squat walls; in moderately slender walls, diagonal cracking tends to predominate over rocking and bed joint sliding for increasing levels of vertical compression. Diagonal cracking propagating through blocks tends to prevail over diagonal cracking propagating through mortar joints for increasing vertical compression levels. The increasing interlocking of blocks may transition from diagonal cracking through mortar joints to rocking blocks or bed joint sliding. Commonly, crushing occurs for high levels of vertical compression. The effect of geometry is one of the most significant parameters that influences masonry wall failure mode under seismic action in the above respects. In the section 4.1.4, the experimental tests performed at the Joint Research Centre of Ispra (Anthoine et al., 1995) will be numerical simulated and analyzed to highlight this aspect. They showed how a slender wall is characterized by a flexural response with high-damaged zones located at the top and bottom sides starting from the corners. In contrast, a squat wall exhibits a brittle failure with diagonal cracks in the middle of the panel due to the dominant shear mechanism.

2.1.2.2 Arches and damage mechanisms

The masonry arch is the most significant and one of the most ancient masonry elements expressing in itself the most marked peculiarities, both conceptual and geometrical, of other more complex masonry structures. The arch's understanding is one of the most innovative ideas in the history of constructions providing significantly to the evolution of structures and human progress. Arches appeared in the Mesopotamian brick architecture, as early as the 2nd millennium BC. Their orderly use started with the Ancient Romans, who were the first to utilize this technique to extend structures. It is a primitive element whose structural analysis could lead us to know better and understand old masonry structures' behavior. In this section, a brief investigation, both historical and structural, about masonry arch is presented with this aim. As addressed in Iannuzzo (2018), since the arch affirms its function on the need to span on opening, its form is probably from an evolution of some other primitive systems used for the same idea. In Figure 2.14, the post and lintel system, the corbelled arch, and the arch are shown.

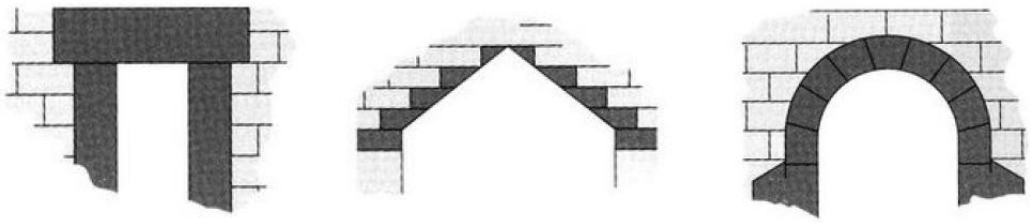

(a) (b) (c)

Figure 2.14: Three methods of spanning a passageway: (a) post and lintel system, (b) corbelled arch, (c) arch. (from Iannuzzo (2018)).

Post and lintel system (Figure 2.14 (a)), or a trabeated system, is a building system where vertical elements with spaces between them hold strong horizontal elements. The horizontal elements are called by various names like lintel, header, or architrave, while the supporting vertical elements may be called posts, columns, or pillars. This structural system is a significant principle of Neolithic architecture and Ancient Indian, Greek and Egyptian architecture also; furthermore, it was spread in North and Central America by Mayan and in South America by Inca

architecture.

(a) (b)

Figure 2.15: Some types of post and lintel system: (a) Stonehenge (b) Machu Picchu (from Iannuzzo (2018)).

From a structural point of view, the two posts are under compression; the lintel is subjected to flexural compressive and tensile stresses due to the self-weight and the loads above it. The system's static mechanism represents the highest problem to a post and lintel construction for the limited weight supported and for the small distance that can be spanned. Corbelled arches were commonly used by ancient civilization around 2000 BC. The first examples of this kind of constructions go back around 3000 BC, like tholos tomb on the Iberian Peninsula and elsewhere around the Mediterranean. In many parts of the world, it is possible to observe constructions related, more or less directly, to the corbelled arch: Ancient Egyptian pyramids from around the time of Sneferu, Ebla in Syria, Ugarit, Nuraghe constructions in ancient Sardinia, Hittites constructions in ancient Anatolia, certain pre-Columbian Mesoamerican constructions, and many others in India and Cambodia.

The corbelled arch (Figure 2.14 (b)) is a sort of intermediate step between a post-lintel structure and the proper arch. Contrary to what one might guess, their similarity is only geometrical because the structural behavior is different. This arch-like construction adopts the corbelling' technique (placing stones progressively cantilevering) to span a space or void in a structure. Thus, the corbel arch is built by offsetting from each supporting side successive courses of stone to

(a) (b)

Figure 2.16: Some historical examples of a corbelled arch: (a) Kompong Kdei Bridge of Cambodia, (b) False arch at "Cuadrángulo de las monjas" at Uxmal in Yucatán - Maya architecture (from Iannuzzo (2018)).

project towards the symmetry axis until the courses meet at the archway's apex. Corbelling the courses means that the arches can be constructed with no centering or shorting. This peculiar characteristic of corbel arches is because almost all other arches request some temporary support (Roca et al., 2019). Although improved load-bearing efficiency over the post and lintel design, corbeled arches are not fully self-supporting structures. The corbeled arch is the so-called "false arch." This behavior leads to an important difference from proper arches: not all of the structure's tensile stresses caused by the superstructure's weight are transformed into compressive stresses.

Even if some ancient Sumerian buildings include examples of simple small arches and brick masonry arches discovered in the ruins of Ur in Mesopotamia (1400 BC), the development and the wide spreading of the arch structure appeared later. If the Etruscans were the first to make systematic use of the masonry arches, the Romans employed this structure largely, diffusing this kind of system in Europe by constructing many relevant masonry arch structures such as aqueducts, bridges, and finally the most famous ancient building constructed with arches: The Colosseum (see Figure 2.17).

From a structural point of view, the arch is a pure curved compression form, which could span a large area by resolving forces into compressive stresses elimi-

Figure 2.17: Some historical arch structures: Colosseum.

(a)

(b)

Figure 2.18: Some historical arch structures: (a) Arch of Triumph (destroyed) in Syria's Palmyra ruins, (b) aqueduct in the Old Town of Segovia (from Iannuzzo (2018)).

nating tensile stresses. In Figure 2.19 some typical shapes of arch are reported.

An overview of the static behavior investigated over the years on the mechanisms of the arches is reported.

Vitruvio in *De architectura* showed to have intuited the pushing effect exerted

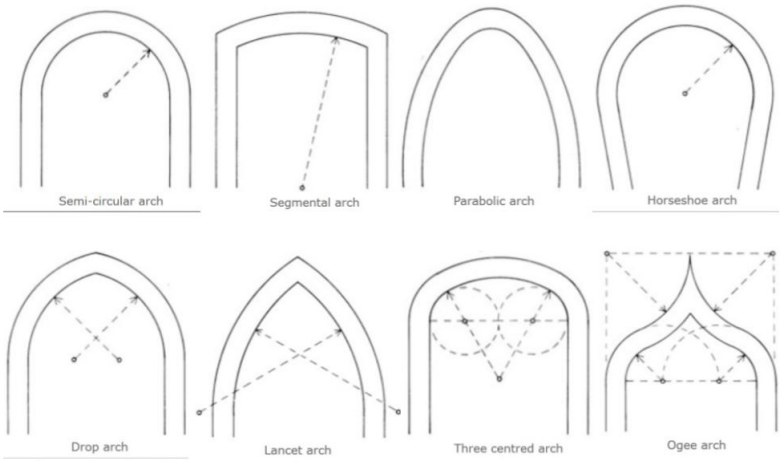

Figure 2.19: Some types of arch.

by the vault on the piers. Leon Battista Alberti (*De Re Aedificatoria; 1452*) decreed the aesthetic and symbolic principles and the proportions underlying the dimensioning of the structures, Leonardo da Vinci (*Codes of Madrid, Forster II Code, 1490-1505*) defined the arch as "an arch is nothing but a strength caused by two weaknesses." As reported in a drawing of the *Forster II Code* (Figure 2.21 (a)), it seems that Leonardo arrived at a criterion of safety reported in Figure 2.21 (b) and a failure rule shown in Figure 2.21 (c): someone could think that the lines depicted in Figure 2.21 (b) and Figure 2.21 (c) describe a line of thrust due to a load acting at the keystone (Figure 2.21 (a)) and much larger than the self-weight of the arch. Leonardo synthesized the failure rule with these words: "... the arch will not crack if the chord of the outer arch will not touch the inner arch ..." in which it is possible first to see a primitive formulation of the rule according to which the line of thrust has to lie within the arch geometry.

The first analytical study on the mechanics of the arch can be traced back to Robert Hooke. During his career, he showed experiments on arches model. He knew the arch's intimate physical behavior, but he did not give the corresponding mathematical theory during his life. Hooke noted that if he could solve the catenary problem, he would, at the same time, have found the solution of the shape of the perfect arch carrying the same loads in compression. Hooke, who was Cristopher Wren's collaborator in carrying out the work on St Paul's Cathedral

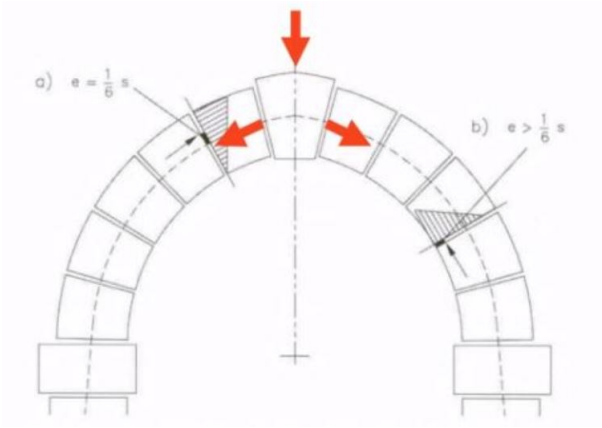

Figure 2.20: The pushing effect exerted by the vault on the piers for Vitruvio.

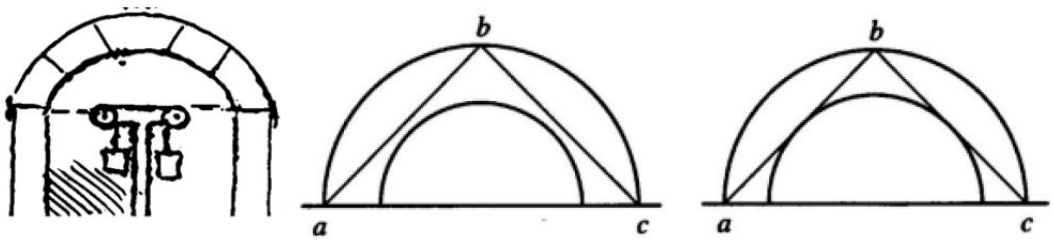

(a) (b) (c)

Figure 2.21: A famous drawing from the Forster Codex (a) which shows an experimental test on an arch made by Leonardo da Vinci. He formulated a safety criterion (b) and a failure rule (c).

in London after the Great Fire (1666) (Figure 2.22), as well as being a member of the Royal Society, observed that an upside-down catenary works only in compression, just as a catenary works only in tension. Since the nineteenth century, various scientists have tried to prove that Hooke's work on the catenary guided Wren, but the evidence is not certain.

Starting from Hooke's intuition, expressed in the aphorism "ut pendet continuum flexile, sic stabit contiguum rigidum inversum", studies on these structures' optimal profile continued. The search for the resolution of the catenary problem was not trivial. Leibniz (1691) and after Huygens and Johann Bernoulli, with his older brother Jakob (*Problema de curvatura fornicis*) also seem to have resolved the issue at about the same time: anyhow, their solutions were not rigorous

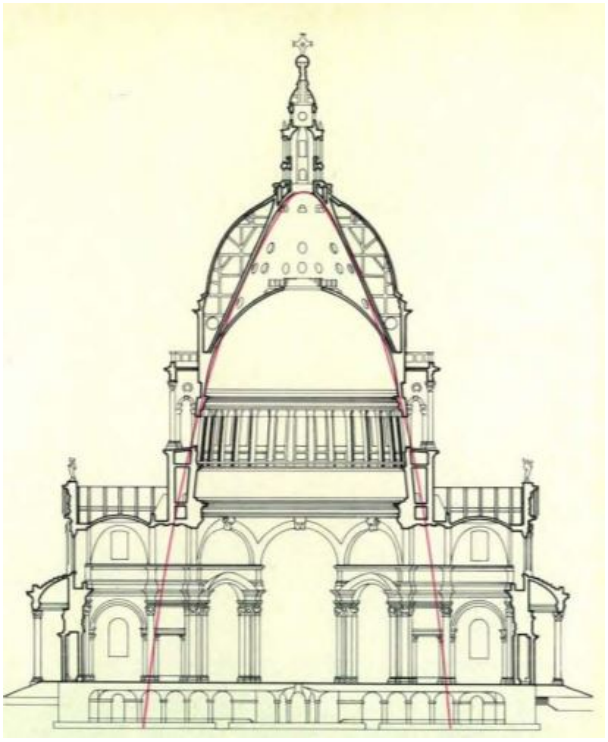

Figure 2.22: Structure of St Paul's Cathedral in London.

mathematically.

Though with some mistakes, the problem was solved some years later by Gregory (1697). Gregory cleared that if the thrust line lies within the arch can be found, then, the arch is stable. Finally, Gregory understood that the horizontal action on an arch's abutment is the same as pulling an equivalent hanging chain.

La Hire in La Hire (1695) investigated a semi-circular arch assembled from rigid voussoirs and considered frictionless joints between them. He provided important contributions to the development of the arch's static, using for the first time the mechanics for the study of an arch, analyzed as composed by rigid bodies. The innovation in La Hire's consists of the use of the force polygon and the corresponding funicular polygon for the arch. Although the funicular polygon for an arch can be viewed as a "discrete" line of thrust, he posed himself the problem of finding the weights of the voussoirs such that equilibrium should be kept. Since he assumed that the contact joints are smooth, the thrust line must be orthogonal to the joints conducting to a paradoxical statement. If the springing line is horizontal,

it follows that the springing voussoirs must have an infinite weight to guarantee the stability of the arch. For the first time, sliding mechanisms were taken into account. Indeed La Hire remarked that friction between the voussoirs would confer the necessary stability to the structure. Though then in La Hire (1712), he returned to the arch given a different hypothesis: the friction was taken to be so large that sliding could not occur. Then, the direction of the line of thrust was no longer fixed as before, and the line of thrust, is in this case, undetermined.

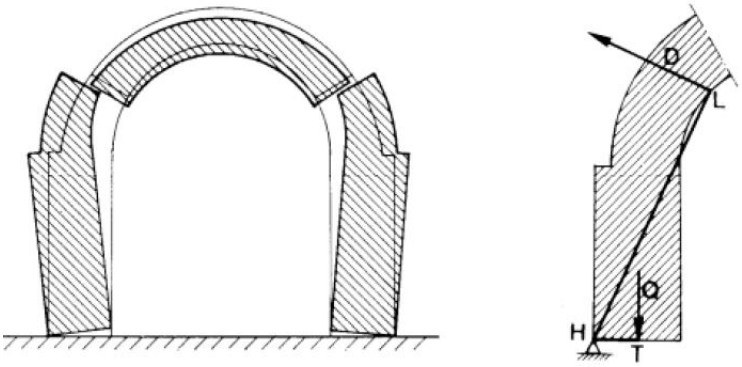

Figure 2.23: Collapse scheme for De La Hire.

Was in that period that the French engineer Bernard Forest de Bélidor made widespread use of La Hire's method and in his work Bélidor (1729), he spent an entire section on arches treating them approximately using La Hire's theories but applying some changes with the basic aim to establish a set of design rules.

In this historical context, Couplet noted that the voussoirs could not slide each other allowing only detachments and excluded from the calculation any resistance in compression of the masonry. Couplet wrote in Couplet (1729) and in Couplet (1730) two remarkable memoirs on arch thrust, implicitly arrogating Heyman's three basic assumptions: no tensile strength, infinite compressive strength, and sliding cannot occur. Furthermore, Couplet formalized in this work two ways of approaching any structural problem: through equilibrium (statics), considering the thrust lines, and through deformation (mechanisms). In particular, he states that an arch will not collapse if the chord of half the extrados does not touch the intrados but is entirely lying within the arch geometry. In his work, Couplet tackled the problem to find the minimum thickness of a round arch subjected only

to its weight. Later, he reworks the La Hire and Bélidor approaches to evaluate the abutment thrust and the whole structure's stability. The Couplet's work was noted quickly and had a big spread.

Indeed, as mentioned in Heyman (1966), Danyzy (Danyzy, 1732) made several tests following the Couplet's approach. He used arches made from plaster voussoirs and he found confirmations of Couplet's results. Although the Danyzy's results were published not before 1778, Frezier (Frézier, 1737) reported in his work a plate showing the Danyzy's experimental. Still, the analysis of St.Peter Dome, conducted by Poleni, are worth mentioning. Their object is the investigation of the numerous injuries that had occurred on the dome designed by Michelangelo. Before Poleni's examinations note that Giacomo Della Porta modified the project, that built it by raising the top of 7 meters and transforming Michelangelo's hemispherical dome into a raised dome. Poleni showed a deep knowledge of La Hire and Couplet's work and a profound understanding of the concept of Hooke's hanging chain. Poleni thought of the dome as made up of segments that leaned against each other at the top so that the mechanical behavior was traced back to that of the arch. Using the mechanism of the arch, he explained the cracking of the dome, according to the meridians.

Call Gregory back (Gregory, 1697), which, according to Poleni, is the first to argue that catenaries give us the curves of the most "existent" strings: "Qualis tamen sit fornicis figura legitima, ad usque editas nostras demonstrationes ignoratam est." He drew inspiration even from work by Stirling (1717) using a catenary formed by smooth spheres. After experimental tests conducted in Padua, he concluded that the crack pattern was due only to the poor material used for the construction's inferior part. The dome was repaired and reinforced between 1743 and 1744 with iron hoops, and the cracks were patched (through "scuci e cuci").

A more decisive development in the study of the arch was due to Coulomb. In his famous memoir "Essai sur une application des règles de maximis et minimis a quelques problèmes de statique relatifs a l'Architecture" (Coulomb, 1773) Coulomb resolved many problems considering failure imaginary planes along which the slip could occur concerning the cohesion and the friction of the material. Although, concerning the masonry arches, Coulomb took into account the strength of the material and assessed the stability only with equilibrium considerations

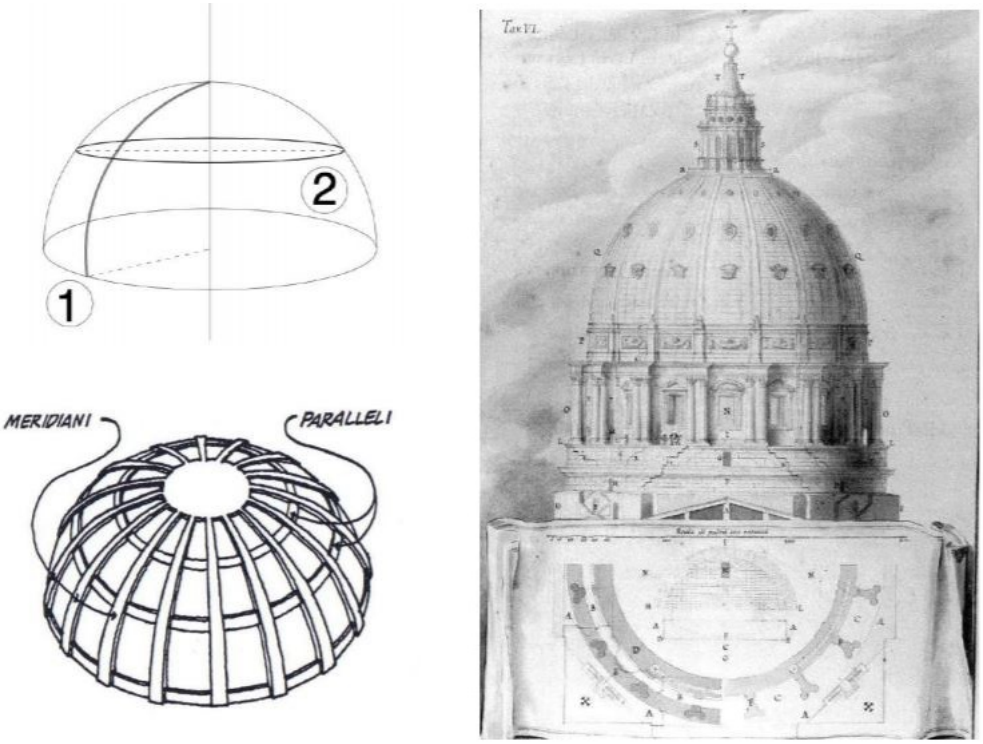

Figure 2.24: Meridians and parallels; crack detected in the dome of St. Peter's (Vanvitelli, 1743).

through maximum and minimum principles. Moreover, he stated that the arch's failure could occur only with the formation of hinges between voussoirs, concluding that the friction was enough to prevent any sliding. Coulomb's work meant a pillar in the development of the mechanics of the arches.

Although his example was not followed, deserving of note is the work offered by Lorenzo Mascheroni in 1785 and reissued in 1819 and 1829. With perfect control of the kinematic analysis, he showed that the collapse could occur according to four distinct mechanisms in a symmetrical arch, which, if not all equally probable, have nevertheless be taken into account to establish a rigorous theory. Despite this, almost all subsequent authors would have followed the Colombian approach.

Successively, indeed, Navier mentioned the Coulomb approach for arches theory. In his famous lessons, Résume des Leçons Données a l'Ecole des Ponts et Chassées (Navier, 1833-38), Navier resumes the problem of arches with the hypothesis of Coulomb, specifying its contents. It takes into consideration the four

collapse mechanisms of a symmetrical arch. Michon makes a decisive contribution. In 1848 (Michon, 1848) he published a collection of "Tables et formules pratiques pour l'établissement des voutes cylindriques" with which the analysis of the mechanisms of collapse found a definitive solution. As addressed in Becchi and Foce (2002), from the point of view of modern structural mechanics, the studies on collapsing analysis that was carried out earlier represent a valuable term of comparison. Indeed, in modern times the stability of the arch falls within the frame of Limit Analysis (see Section 2.2.4), through which the degree of safety of the structure can be assessed.

The first application of limit analysis is from Kooharian with his work "Limit Analysis of Voussoir (Segmental) and Concrete Arches" (Kooharian, 1952). This paper represents the starting point for the application of Limit Analysis to masonry structures.

Considering the Heyman's plasticity hypothesis (Heyman, 1966) regarding the impossibility of mutual sliding between the ashlars, it is reasonable to think that the nineteenth-century and earlier authors' classification is more general considering cases with sliding in the presence of friction.

2.2 Modeling approaches for masonry structures and analysis strategies

In the last half-century, the scientific community put a great deal of effort into the computational analysis of masonry structures in order to develop tools for the prediction and assessment of their structural behavior. Different approaches and scales of representation of the mechanical behavior have been proposed. In this section, a short outline of available methods is presented and attention is focused on the finite element models (FEM) description, according to the goal of this research.

2.2.1 FEM based approaches

Finite element models involving nonlinear constitutive laws with damage and plasticity inner variables appear as promising tools for assessing the structural capacity of masonry buildings. These models are usually classified concerning the modeling scale used, distinguishing between micromechanical, macromechanical, and multiscale models.

2.2.1.1 Micromechanical Finite Element Approach

The different components of masonry, units, mortar and unit-mortar interface, are distinctly modeled in the micromechanical approaches. In this method, all the internal structure information is described; thus, the complex interaction between the masonry constituents is naturally taken into account. As opposed to the macromechanical approaches (see Section 2.2.1.2), which are preferred for large scale modeling, these methods are suitable to estimate all the constituents' local behavior. One of the first pioneers in this method was Page (1978), who attempted to apply micro-modeling approaches to masonry structures. Under this approach, nonlinear interface elements were used to represent mortar joints, accounting for high compressive strength, low tensile strength, and limited shear strength dependent on the level of compression and the composite material's bond strength. For the bricks, linear-elastic continuum finite elements were used. Experimental tests conducted by the author determined the non-linear stress-strain relationships and the failure criteria. Figure 2.25 schematically shows the most common micro-models.

In the so-called *detailed* micromechanical strategy (see Figure 2.25 (a)), bricks and mortar are described through continuum finite elements, whereas discontinuous elements model the mortar interfaces. The elastic and inelastic properties of all the components can be realistically taken into account. The *detailed* micromodeling is probably the most accurate tool to reproduce the real behavior of masonry. This strategy leads to very accurate results but requires an intensive computational effort. Alternately, *simplified* micromodels were developed, which consider joints as mechanical units representing both mortar and unit-mortar interface and adopt either expanded units with elastic response and potential crack

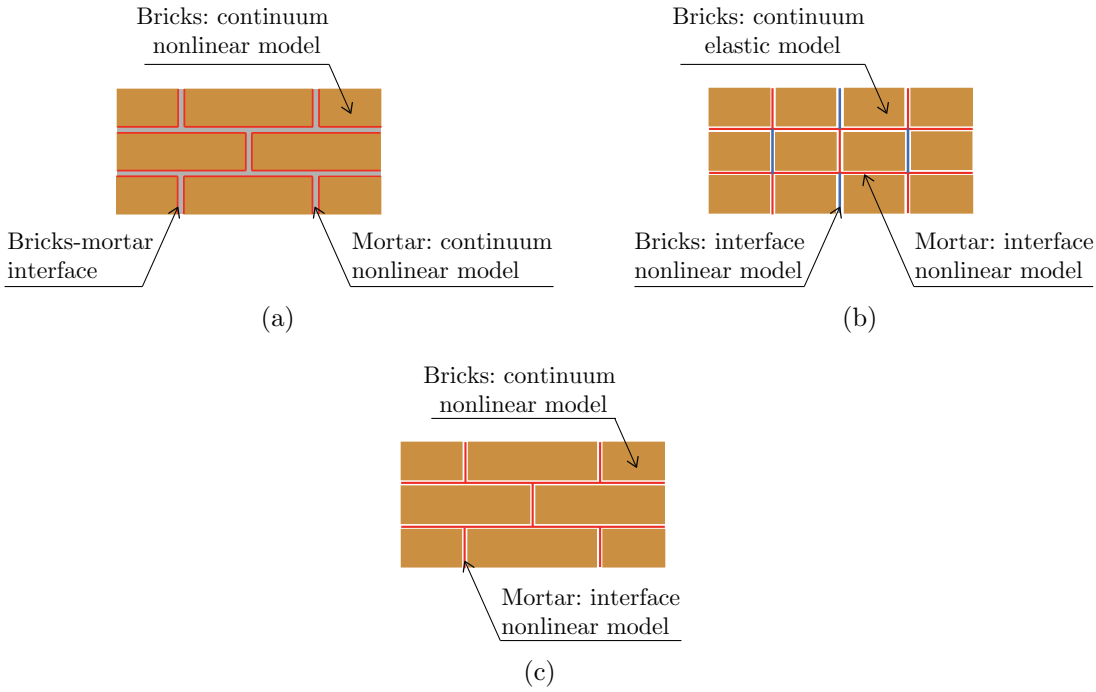

Figure 2.25: Micromodeling technique (Gatta, 2019).

interfaces or continuum nonlinear model for bricks (Figures 2.25 (b) and (c), respectively). It is also possible to model both bricks and mortar with continuum elements without using interface elements (see Section 3.1.1).

Within this framework, different constitutive laws were proposed for each constituent material, according to the assumption reported below by Addessi and Sacco (2012): model for the brick, that can be considered as:

- rigid;
- deformable with linear response;
- interface or continuum material with nonlinear response;

and model for the mortar, that can be considered as

- interface or continuum material characterized by linear response;
- interface or continuum material characterized by nonlinear response.

Micromechanical models were widely adopted by several authors in literature, Lourenço and Rots (1997); Gambarotta and Lagomarsino (1997); Oliveira and Lourenço (2004); Sacco and Toti (2010); Raffa et al. (2013); Minga et al. (2018) and these use a discrete description of masonry micro-structure, mixing continuum and interface elements for bricks and mortar joints, respectively.

The model suggested by Lourenço and Rots (1997) is widely used. The authors implemented a constitutive interface model based on an incremental formulation of plasticity theory. They proposed a composite yield surface to simulate the tensile failure of mortar joints, shear response of joints, and crushing of units under monotonic loading. Furthermore, cracks in the units were taken into account by placing a potential crack interface in each unit's middle part. A modified version of the model was later introduced by Oliveira and Lourenço (2004) to accurately reproduce the interface cyclic behavior's main characteristic (Figure 2.26).

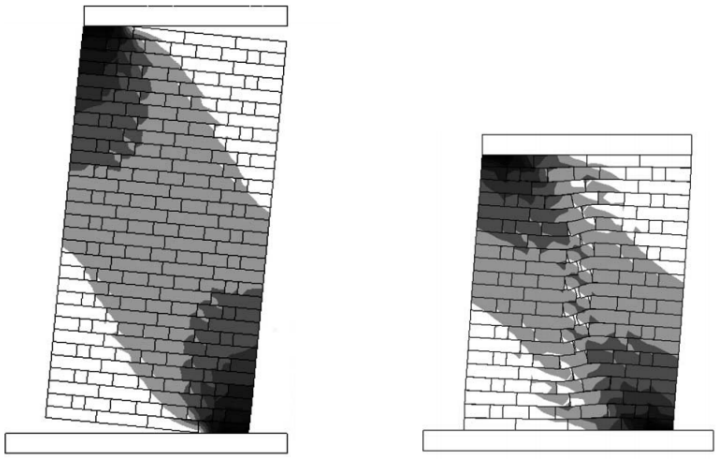

(a) (b)

Figure 2.26: Micro-modeling of a high (a) and a law (b) wall, from Oliveira and Lourenço (2004).

Sacco and Toti (2010) presented another interesting interface model (Figure 2.27). The authors proposed a formulation of the interface to represent the interaction between brick-mortar at the contact surface, which considers the combined effect of damage and friction. The model was used to model masonry elements, particularly to investigate the behavior of unreinforced masonry arches.

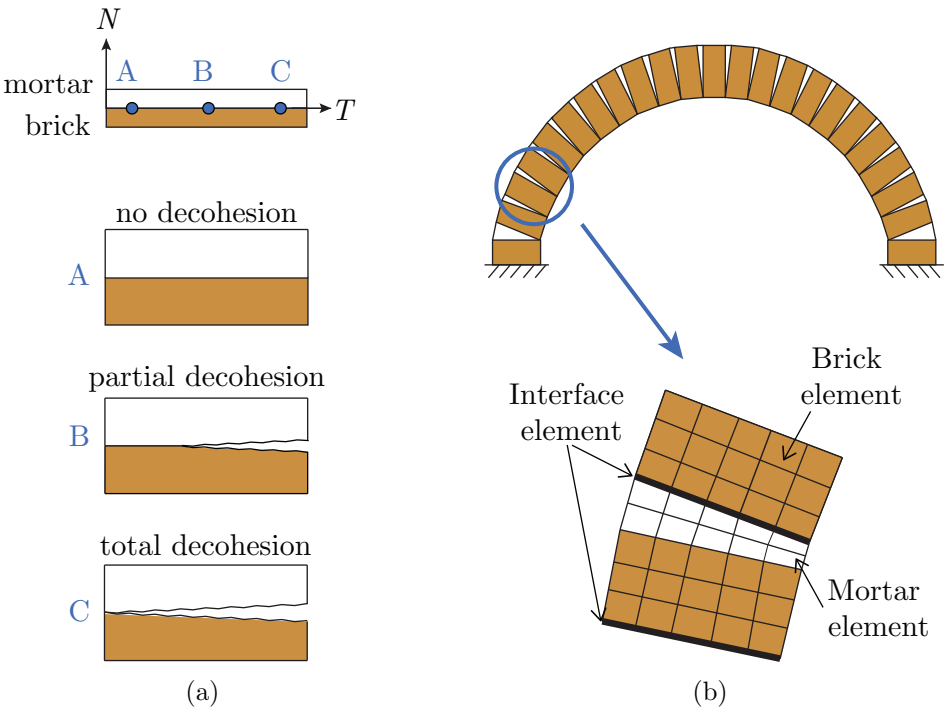

Figure 2.27: Sacco and Toti (2010): (a) damaging states of brick-mortar interface and (b) detailed micromodeling of a masonry arch.

2.2.1.2 Macromechanical Finite Element Approach

In the macromechanical approaches, masonry is modeled as a continuum deformable body, considered as a homogenized medium.

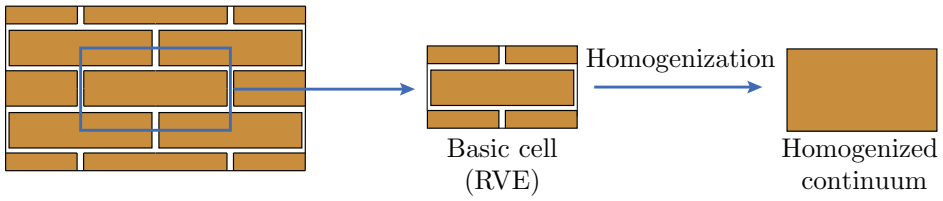

Figure 2.28: Macro-modeling technique: masonry as a homogeneous material.

These models are based on phenomenological constitutive laws for the masonry material. The definition of suitable homogeneous constitutive laws is a challenging task, in that an appropriate relationship has to be established between average masonry strains and stresses. The continuum parameters must be defined us-

ing tests on sufficiently large-sized specimens subjected to homogeneous states of stress. As an alternative to difficult experimental tests, it is possible to estimate the individual components experimentally and consider the obtained data as input parameters of numerical homogenization procedures and multiscale approaches, where the constitutive law of the material is obtained from a homogenization process which relates the structural-scale model to a material-scale model (see Section 2.2.1.3). Despite some difficulties in identifying the constitutive law of the equivalent homogenized material and the mechanical parameters, macromechanical models are probably the most popular and common approaches due to their low computational burden. They are widely used to analyze real complex structures. Figures 2.29 and 2.30 show some examples of structures modeled with macromechanical techniques.

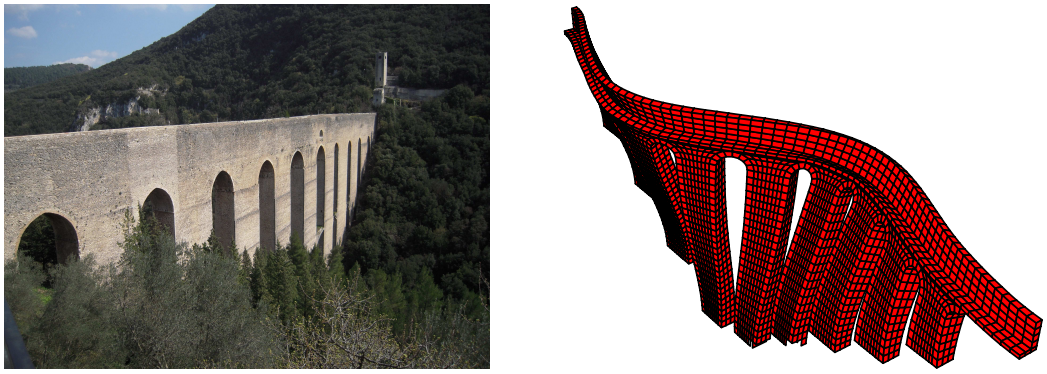

(a) (b)

Figure 2.29: Ponte delle Torri: Spoleto: (a) real structure and (b) FE model used by Addessi et al. (2020b).

Macromechanical models show significant useful advantages compared to more detailed approaches describing discontinuities. In particular, FE meshes are simpler since they do not accurately describe masonry internal structure. The finite elements can have dimensions greater than the single brick units. This type of modeling is most valuable when a compromise between accuracy and efficiency is needed.

Different constitutive laws have been proposed to describe masonry mechanical behavior. A classical model is the No-Tension Material law, where a zero tensile

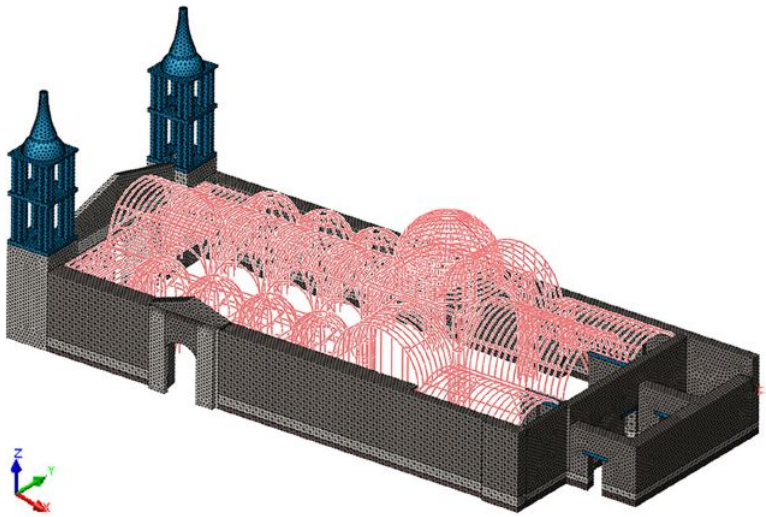

Figure 2.30: Ciocci et al. (2018): FE model of the Ica Cathedral in Peru.

strength is assumed; thus, fracture strains arise when the stress is zero. The hypothesis of no-tension material has been widely used to analyze the stability of masonry vaults and domes (Heyman, 1966). Other elegant approaches that used the no-tension law are present in literature (Angelillo, 1994; Alfano et al., 2000; Bruggi and Taliercio, 2015). Although they represent solutions for such a complex problem, their applicability to real case studies is still limited. Furthermore, although the assumption of null tensile strength can be considered, in general, conservative, this could lead to failure mechanisms which are not coherent with the ones experimentally observed, given that actually masonry tensile strength of masonry is low but no zero.

Other macromechanical approaches have been developed, using constitutive laws based on continuum damage mechanics (see Figure 2.29), discrete and smeared fracture mechanics (see Figure 2.30), and plasticity theory (Lourenço et al., 1997; Sena-Cruz et al., 2004; Karapitta et al., 2011; Addessi and Sacco, 2014). A more detailed description will be later addressed in Section 2.3.

Due to their efficiency, their diffusion in commercial FE codes and the relatively few mechanical parameters to chosen, smeared crack and isotropic damage models have been widely adopted to investigate masonry structures. However, in

some cases, their availability for the simulation of masonry structures' collapse behavior presents some shortcomings, mainly due to the anisotropy of masonry and its heterogeneity. But poor information, usually available on historic structures' mechanical properties, favors often using these less accurate models.

More sophisticated models have been developed (Berto et al., 2002; Pelà et al., 2013; Gatta, 2019) taking account orthotropic response that represents scientifically sound solutions. Furthermore, their application on real case study has been limited because their computational effort and the number of material properties to be mechanically characterized are considerably higher than isotropic approaches. As highlighted before, this modeling technique represents, despite its intrinsic limits, a good compromise between accuracy and computational effort, and a large number of proposed models prove a strong interest in its development.

2.2.1.3 Multiscale models and computational homogenization

Multiscale modeling has caught hold between micro and macro approaches in the last decades to study heterogeneous microstructured materials' mechanical response as masonry. Two main families based on homogenization procedures and multiscale approaches could be identified. As addressed in Lloberas-Valls et al. (2012), the first approach is known as Concurrent Multiscale Method (Brasile and Casciaro, 2009; Leonetti et al., 2018; Reccia et al., 2018). As a multiscale model, it concerns the study of multiple length scales and information exchange among them. The micro-structural scale is adaptively included and resolved in the structural model, establishing a strong coupling between macro and micro scales. Different versions of concurrent multiscale methods have been employed to analyze damage masonry structures in previous works by some authors Greco et al. (2016, 2017). Still, a well-known model that is worth mentioning is Leonetti et al. (2018). As addressed by the authors, as the location of damage initiation and evolution is not known a priori in general, these multiscale methods are provided with an adaptive ability, meaning that the model can automatically refine itself according to a suitably defined zooming-in criterion based on the first failure detection at the microscopic scale (see Figure 2.31).

The associated model refinement criterion requires evaluating microscopically

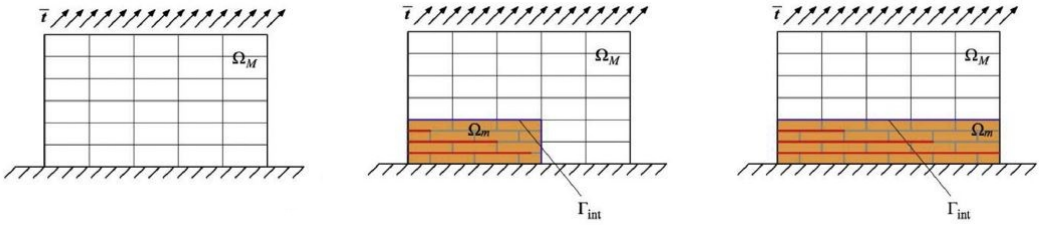

(a) (b) (c)

Figure 2.31: From Leonetti et al. (2018):schematic representation of the adaptive model refinement strategy: (a) initial coarse mesh composed of homogenized macro-elements; (b) intermediate multi-level mesh with partial structural damage; (c) final multi-level mesh at incipient collapse.

informed first failure surfaces, which consider both classical and bending deformation effects, by catching advantage of a couple-stress based homogenization technique. The second approach is known as Computational Homogenization Method (Masiani and Trovalusci, 1996; Cecchi et al., 2005; Mistler et al., 2007). Assuming that the length scales are separated, this approach establishes a weak coupling between them. This approach divides the structural problem into two scales: an equivalent homogenized medium is studied at the macrolevel, where the constitutive response at each material point is determined by homogenizing the stress field computed in a properly selected representative volume element (RVE). To this aim, several RVEs geometries have been proposed to account for different periodic and non-periodic patterns of masonry (Anthoine, 1995). Indeed, the RVE contains a detailed description of masonry components, geometry, arrangement, and constitutive behavior and is analyzed at micro-scale. The constitutive response at macrolevel, initially unknown, is derived by applying concepts of localization and homogenization within a scale transition procedure (see Figure 2.33).

A strain driven formulation is usually assumed, consisting of evaluating the macroscopic strain vector $\mathbf{E}$ at each material point of the macrolevel model, which is adopted as input data for the linked sub-domain (the before mentioned RVE). An accurately defined boundary values problem (BVP) has to be solved to determine the stress field on the RVE and, then, the corresponding macroscopic stress

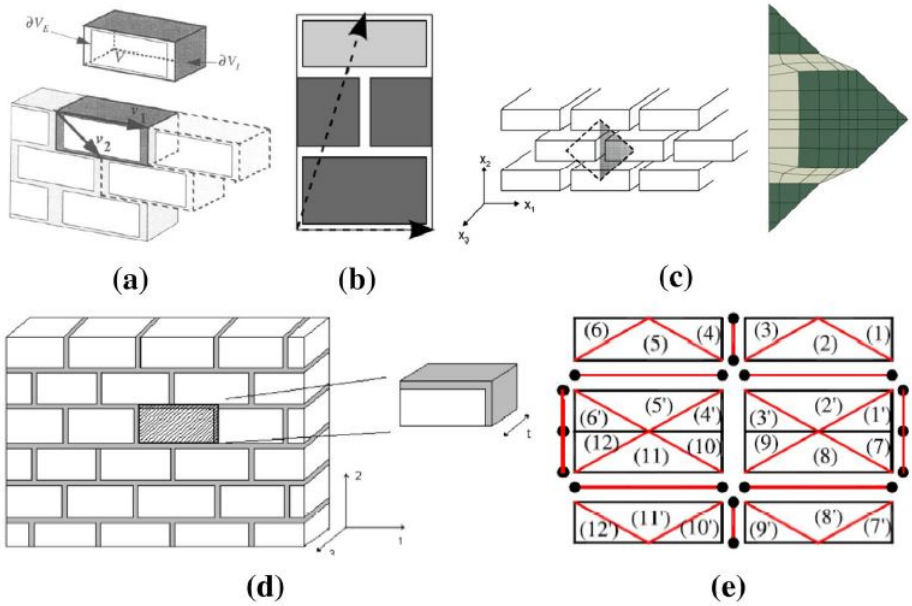

Figure 2.32: Examples of RVEs adopted for the derivation of homogenized masonry mechanical properties, (a) Anthoine et al. (1995), (b) Cavalagli et al. (2011), (c) Taliercio (2014), (d) Stefanou et al. (2015) and (e) Milani (2011); (D'Altri et al., 2019).

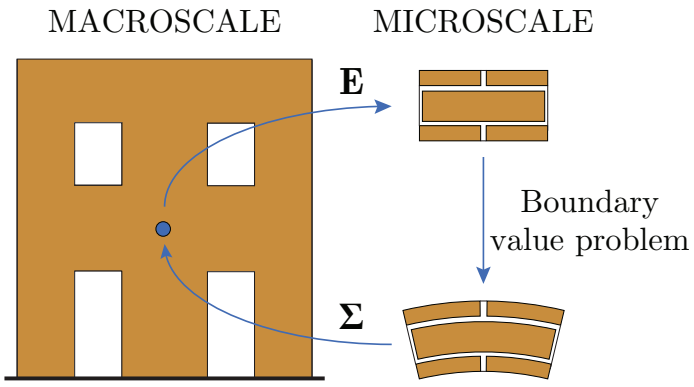

Figure 2.33: Multiscale technique: transition between macro and microscale.

$\boldsymbol{\Sigma}$ using the Hill-Mandel equivalence principle. Different boundary conditions, i.e. prescribed displacements, prescribed tractions, and periodic conditions were considered for the RVE to obtain the best estimation of the homogenized mechanical properties.

As mentioned in D'Altri et al. (2019), alternative multiscale approaches can be found in the scientific literature, which may differ in terms of:

- Continuum type adopted in the structural-scale model (Cauchy continuum, Cosserat continuum, etc);
- Type of homogenization procedure (first or second order computational homogenization, transformation field analysis (TFA), etc);
- Type of modeling of the RVE (i.e. modeling strategy adopted for the material-scale model, e.g. block-based models).

These approaches generally work on step-by-step and point- by- point transitions between the structural-scale model and the material-scale model, and vice-versa. Multiscale computational homogenization methods are commonly implemented within the FEM framework and, so, also called FE^2 approaches. Most of these approaches are based on FE first-order homogenization schemes. Still, well-known models that are worth mentioning are (Sacco, 2009; Zucchini and Lourenço, 2009; Addessi and Sacco, 2011; De Bellis and Addessi, 2011; Addessi and Sacco, 2012).

2.2.2 Structural component models

The most simple approach to model complex historic buildings is given by defining different structural elements, using truss, beam, panel, plate, or shell elements to represent columns, piers, arches, and vaults. The macro-element method idealizes the structure into structural components with nonlinear phenomenological responses, mainly according to empirical criteria inspired by the observation of post-earthquake damage patterns. For the study of buildings, significant research efforts have been devoted to the development of rigid and deformable macro-elements. Commonly earthquake-damage observations showed that cracks and damage are concentrated in piers and spandrels that are typically identified as the two main structural components. The subdivision of the structure into components is an a-priori operation conducted by who interprets the structural scheme of the building. The macro-element modeling is one of the most simplified approaches adopted to investigate masonry structures, but this also shows some

drawbacks. In particular, in some cases, it assumes that any activation of local failure mode, mainly associated with the out-of-plane response of masonry walls, is prevented, contrary to a reality where out-of-plane and in-plane damages can simultaneously arise. They cannot account for structural details and the a-priori idealization of the structure requires a certain level of expertise in modeling. Several formulations have been proposed and a detailed classification can be found in D'Altri et al. (2019), which distinguishes two main categories: equivalent beam-based (Lagomarsino et al., 2013; Addessi et al., 2015; Liberatore et al., 2017) and spring-based approaches (Chen et al., 2008; Caliò et al., 2012).

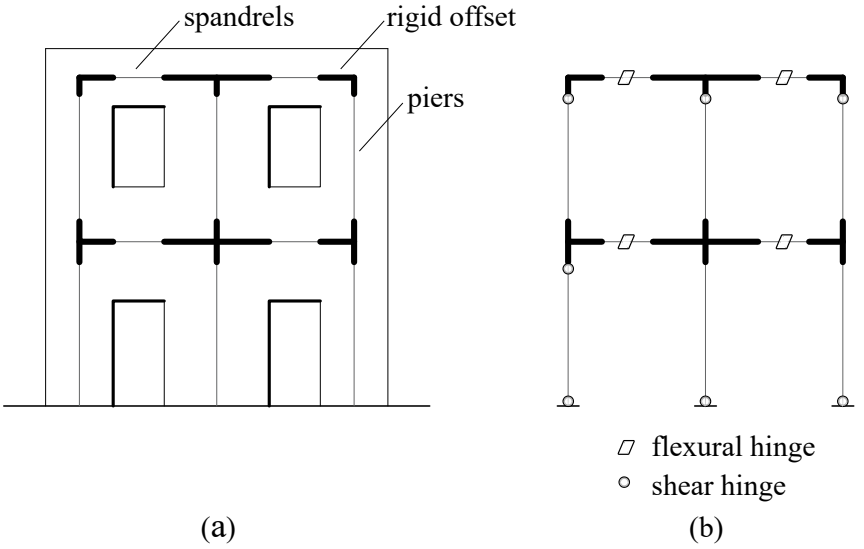

Figure 2.34: From Addessi et al. (2015): (a) equivalent frame scheme and (b) distribution of the plastic hinge.

The first, commonly known as "equivalent frame models," reproduces the masonry panels behavior with nonlinear beam elements (see Figure 2.34). As an example, in Sangirardi et al. (2019) the authors consider the walls as an assemble of deformable one-dimensional elements connected through rigid nodes, which are indeed undamaged parts of the walls. Piers and spandrels can be identified as the main load-bearing components. The nonlinear behavior can be modeled using either distributed or lumped inelasticity. In this case, the lumped approach consists of placing flexural and shear hinges at both the ends and mid-span of the elements, respectively. Here the authors used a sophisticated approach, in-

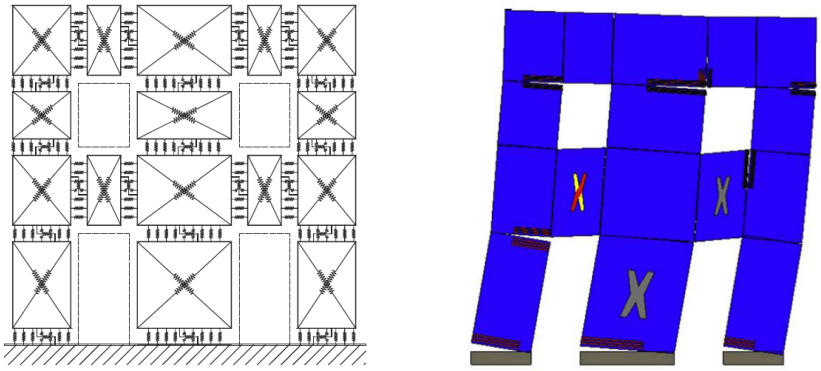

(a) (b)

Figure 2.35: From Caliò et al. (2012): (a) equivalent mechanical scheme and (b) example of damage scenarios

troducing a modified version (Liberatore et al., 2019) of the Bouc-Wen model, accounting for the strength degradation, in the constitutive laws of the flexural and shear hinges, to simulate the complex nonlinear behavior of masonry panels under cyclic loads. The spring-based approach approximates the in-plane response of walls using nonlinear springs. An interesting advance in this method's context is the macro-element model developed by Caliò et al. (2012), where the basic panel element is described by four rigid edges connected by four hinges and two diagonal nonlinear springs. Each side of the panel can interact with other panels using a discrete distribution of nonlinear springs (see Figure 2.35).

2.2.3 Discrete element method

The Discrete element (DE) method was proposed by Cundall (1971) for the analysis of fracture mechanics problems. Later, this approach was applied to solids and has also been used to model masonry structures. This method is characterized by modeling the material as an assemblage of distinct blocks, the masonry units (Lemos, 2007), interacting along the boundaries.

There are presently various discrete element formulations applied to the study of masonry structures. In general blocks can be considered both rigid and deformable. For structures where relatively low stresses and strains occur in the

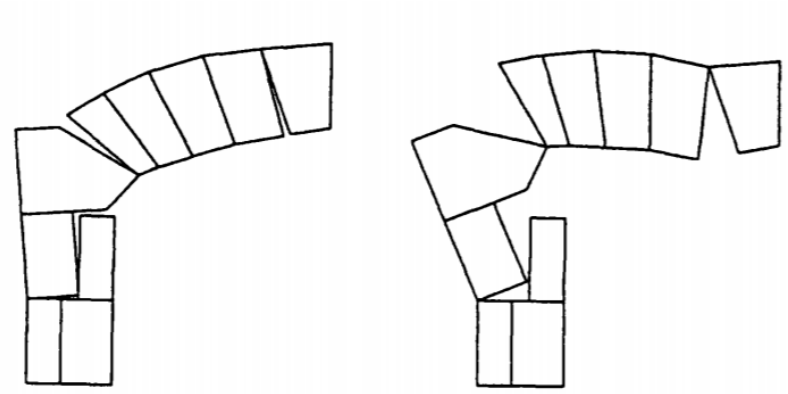

Figure 2.36: From Mamaghani et al. (1999): Failure mode of a masonry arch.

blocks, the undeformable blocks' hypothesis is rather realistic. On the other hand, the consideration of block deformability approaches discrete element method. An overview of the DE methods is from Lemos (2007), where various formulations were reviewed to clarify the main differences that can be found in the contact assumptions, block representation and solution methods. Several applications have been conducted on real masonry structures using rigid or elastic blocks. A large number of references are reported in Lemos (2007), Roca et al. (2010) and D'Altri et al. (2019).

2.2.4 Limit analysis

Starting from the 18th century the principles of statics were applied to masonry structures by Poleni, Coulomb, La Hire, Couplet, and many others. Engineers and architects in the past used considerations related to limit analysis intuitively, but without a general theory. J. Heyman had the merit of the formulation of the theorems of limit or plastic analysis for masonry structures (Heyman, 1966). According to this formulation the limit theorems of plasticity can be applied to masonry structures provided the following conditions are verified:

- Zero tensile strength, that is no tensile forces can be transmitted between masonry blocks;
- Infinite compressive strength;

- No sliding between joints.

The presence of mortar at the joints may provide some weak adhesion; therefore, the first hypothesis may be slightly conservative. The second hypothesis is reasonable because masonry resists well to compressive actions. Moreover, historical buildings usually present stresses under service loading that are one or two orders of magnitude below the stone's crushing strength (Roca et al., 2019). The last one assumes an infinite friction coefficient. Although this is not correct, most cases analyzed in literature concerned slender masonry arches where sliding failures are quite rare. This is not true for squat arches, how in section 3.3 will be investigated. These conditions allow for applying the lower-bound and upper-bound theorems, which lead to the so-called static and kinematic approaches for the analysis of masonry structures, respectively. The limit analysis does not need much computational requirements and knowledge of the practitioner but is still powerful compared to the more sophisticated nonlinear approaches today adopted in modern engineering. A comparison between limit analysis and nonlinear analysis in terms of the capacity curve for an arch loaded at a quarter span is shown in figure 2.37.

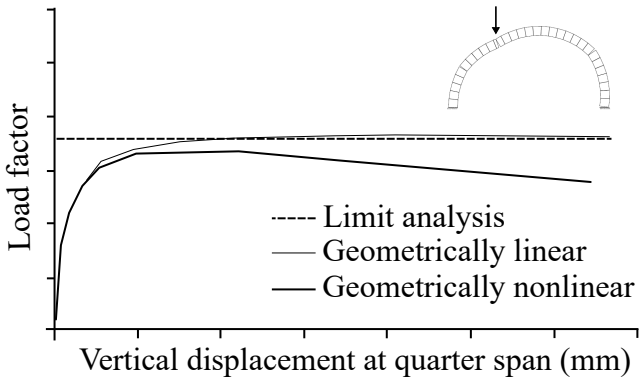

Figure 2.37: Adapted from Lourenço (2001): comparison between limit and nonlinear analysis for a masonry arch loaded at quarter span with point load.

As addressed by Roca et al. (2019), it is possible to observe that the capacity curve can follow the structure's entire behavior from linear elasticity until the maximum load capacity and beyond it, providing the same capacity as limit analysis, if nonlinear geometrical effects are ignored. If nonlinear geometrical effects

are contemplated, the capacity of the arch is reduced to a moderate extent. On the other hand, limit analysis supplies only the maximum capacity with no information about the load history and damage progression. As mentioned before, the collapse mechanism can be investigated by applying static and kinematic approaches. Regarding the last one, Giuffrè (1994) and Carocci (2001) applied the kinematic limit analysis to study masonry structures' vulnerability through their decomposition into rigid blocks. Recent computer-based limit methods, principally based on the kinematic approach, were developed by assuming the following hypothesis:

- Material is characterized by zero tensile and infinite compressive strength;
- Shear failure at joints is perfectly plastic;
- Limit load occurs with small displacements.

It should be noted that the mentioned plastic limit theorems can be used only if the normality condition stands, adopting a simple frictional Coulomb law with an associated flow rule. Nevertheless, no dilatancy occurs in some real samples, and non-associative rules should be assumed. The non-compliance with the normality rule means that plasticity's fundamental theorems will not generally provide a unique solution, as highlighted by Drucker (1954) almost half a century ago. Several methods were proposed for the assessment of masonry structures by limit analysis. For instance Orduña and Lourenço (2005) suggested a solution procedure for the non-associated limit analysis of rigid block masonry assemblages, incorporating non-associated flow rules and a coupled yield surface. Gilbert et al. (2006) introduced a simple iterative approach based on the successive solution of linear programming sub-problems. Baggio and Trovalusci (2000) proposed that the solution of the limit analysis problem in the presence of friction at interfaces between rigid blocks, i.e. a nonlinear programming problem, is obtained by solving a preliminary problem of linear programming, corresponding to a linearized limit analysis in the presence of dilatancy at the interfaces. As an example, Figure 2.38 shows the results of the mentioned procedure applied to two-dimensional assemblages made of polygonal stones modeling the masonry walls of three different historical centers in Italy. The walls are characterized by many contact surfaces

for each stone and their scattered orientation (Figure 2.38 (a)). The considered external forces were the self-weight and the increasing horizontal body action factorized by the multiplier α. The results show a quasi-monolithic behavior of all the walls despite the scatter size, texture, and stone orientation in the masonry. The procedure appears to be successful and able to give a sound collapse mechanism (Figure 2.38 (b)).

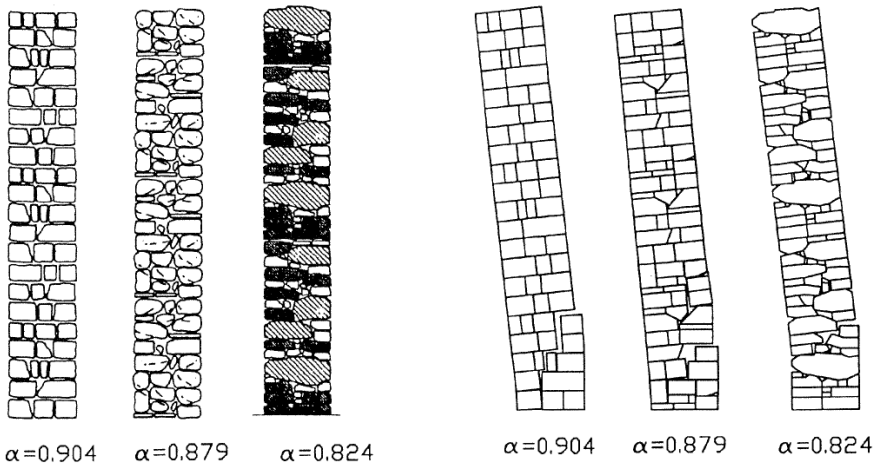

Figure 2.38: From Baggio and Trovalusci (2000): (a) masonry textures and collapse multiplier, (b) collapse mechanism and collapse multiplier of walls in "opus poligonale" subjected to inclinated body force.

As already mentioned, a kinematic analysis should be used as a complementary tool when more sophisticated analyses are performed. Indeed, in the presence of good-quality masonry with homogeneous constructive characteristics and structural behavior, when subjected to seismic loading, ancient structures can be investigated as an assembly of independent and considerably autonomous substructures (2.2.2). For instance, Betti and Vignoli (2011) evaluated the seismic vulnerability of the Basilica of the Santa Maria dell'Impruneta by using both a finite element macro-model and the limit analysis.

2.3 Overview of constitutive models for masonry

The mechanical behavior of masonry material is complex and highly nonlinear, even for moderate stress levels. The available literature on material modeling includes models based on the theories of plasticity, hyperelasticity, hypoelasticity, fracture mechanics, plastic-fracture or continuum damage mechanics. This section briefly describes the fundamental aspects and the main purposes, characterizing the constitutive models that will later be used, implemented, and modified. In particular, basic concepts will be defined for the continuum damage models, the smeared crack models, and the plasticity models.

2.3.1 Continuum damage models

According to this theory, constitutive equations are derived considering the material as a *continuum medium*. Under certain load conditions, the material structure may begin to destroy. Small cracks may form, voids, and other forms of small cavities develop in highly stressed parts. Such deterioration weakens the material and lowers its load-carrying capacity. In a pioneering paper, Kachanov (1958) proposed to describe such deterioration's collective effect through a continuous field variable termed damage. Because of their nature, it is obvious that these defects are discrete entities; therefore, an inherently discrete process was modeled by a continuous variable. What was lost in accuracy in modeling the deterioration was then gained in computational simplicity. A suitable measure of the internal degradation state was taken into account from a scalar internal variable that did not have a clear physical meaning. Further developments have defined the damage variable as the reduction of the cross-sectional area due to microcracking. The simplest version of the isotropic damage model considers the damaged stiffness tensor as a scalar multiple of the initial elastic stiffness tensor, i.e., damage is characterized by a single scalar variable. This approach's principal features will be pointed out to understand better a more sophisticated model, based on damage and plasticity, that will be formulated in Chapter 3.1.1 of this thesis. Figure 2.39 (a) shows a representative volume element (RVE) in the neighborhood of point M of a damaged medium and a plane passing through M with normal $\mathbf{n}$ to define

the damage variable as follows:

$$D(M, \mathbf{n}) = \frac{A_d}{A} \ , \tag{2.1}$$

where A is the sectional area and A_d represents area of defects. Based on its definition, damage variable can vary between 0 and 1, corresponding to the virgin and fully damaged material, respectively. If isotropic damage is considered, dependency from the normal $\mathbf{n}$ is neglected and 2.1 is further simplified:

$$D(M) = \frac{A_d}{A} \ , \tag{2.2}$$

To use classical laws of continuous mechanics, the formulation of continuum damage models needs a definition of equivalent criterion between the damaged material configuration and a fictitious undamaged one. To this purpose, the net stress concept has to be presented. This is usually done by considering a simple uni-axial tensile test, depicted in Figure 2.39 (b). As the applied force F is increased, the transversal section A_0 decreases due to Poisson's effect and the onset of microcracks. Thus, by denoting with A the reduced cross-sectional area caused by the transverse strains, the nominal, σ_0, and the 'true', σ, tension, are expressed as:

$$\sigma_0 = \frac{F}{A_0} \ , \quad \sigma = \frac{F}{A} \ . \tag{2.3}$$

If small hypothesis holds $A_0 = A$ and, consequently, $\sigma_0 = \sigma$. Thus, by accounting for the microvoids area, the net stress results as:

$$\bar{\sigma} = \frac{F}{\tilde{A}} = \frac{F}{A(1-D)} = \frac{\sigma}{1-D} \ . \tag{2.4}$$

Extention of previous concepts to the pluri-axial case is trivial when isotropic damage is considered, with net stress $\bar{\boldsymbol{\sigma}}$ defined as:

$$\bar{\boldsymbol{\sigma}} = \frac{\boldsymbol{\sigma}}{1-D} \ . \tag{2.5}$$

Strain and energy equivalence principles are introduced to complete the concepts fundamental for the formulation of the continuum damage models, as ad-

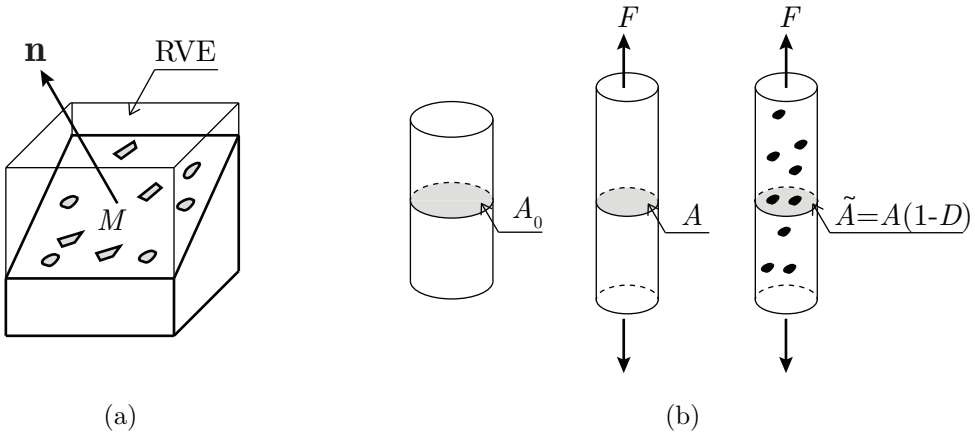

Figure 2.39: Damage mechanics concepts: (a)RVE,(b) effective area $\tilde{A}$.

dressed by Gatta (2019).

2.3.1.1 Strain equivalence principle

The hypothesis of equivalent strain, based on empirical nature, establishes that " the strain behavior of damaged material is represented by constitutive equations of the virgin material in the potential of which the effective stress simply replaces the stress"(Lemaitre, 1985). Ignoring the effect of plastic strain, the constitutive laws for a virgin and damaged material result, sequentially:

$$\boldsymbol{\sigma} = \mathbf{C}\boldsymbol{\varepsilon} \ , \quad \bar{\boldsymbol{\sigma}} = \mathbf{C}\boldsymbol{\varepsilon} \ , \tag{2.6}$$

where $\mathbf{C}$ is the stiffness matrix of the undamaged material. It is useful to introduce the $\tilde{\mathbf{C}}$ matrix, which considers mechanical properties degradation. Thus, the stress-strain relationship of the damaged material can be rewritten as a function of $\boldsymbol{\sigma}$ and $\tilde{\mathbf{C}}$:

$$\boldsymbol{\sigma} = \tilde{\mathbf{C}}\boldsymbol{\varepsilon} \ . \tag{2.7}$$

By deducing $\boldsymbol{\varepsilon}$ from the preceding equation and substituting it in Eq.2.6_2, the latter condition is obtained:

$$\bar{\boldsymbol{\sigma}} = (\mathbf{C}\tilde{\mathbf{C}}^{-1})\boldsymbol{\sigma} \ , \tag{2.8}$$

where $\mathbf{C}\tilde{\mathbf{C}}^{-1}$ denotes the damage operator, which can be expressed, by assuming isotropic damage, as follows:

$$\mathbf{C}\tilde{\mathbf{C}}^{-1} = (1-D)^{-1}\mathbf{I} \ , \tag{2.9}$$

with $\mathbf{I}$ identity matrix. Consequently, the effective damage matrix $\tilde{\mathbf{C}}$ and the net stress $\bar{\boldsymbol{\sigma}}$ are expressed as:

$$\tilde{\mathbf{C}} = (1-D)\mathbf{C} \ , \tag{2.10}$$

and

$$\bar{\boldsymbol{\sigma}} = \frac{\boldsymbol{\sigma}}{1-D} \ . \tag{2.11}$$

Conclusively, by describing the effective stress $\tilde{\boldsymbol{\sigma}}$ as the stress acting on the undamaged material, the illustrated principle establishes an equivalence between effective and net stress:

$$\bar{\boldsymbol{\sigma}} = \tilde{\boldsymbol{\sigma}} = \frac{\boldsymbol{\sigma}}{1-D} \ . \tag{2.12}$$

2.3.1.2 Energy equivalence principle

The energy equivalence principle assumes that "the elastic energy stored in a damaged material Λ_d is equal to the elastic energy of an undamaged equivalent material Λ_0 except that stresses are replaced by the net stresses" (Cordebois et al., 1982). The energy stored in the material Λ_d is:

$$\Lambda_d = \frac{1}{2}\boldsymbol{\sigma}^T\tilde{\mathbf{C}}^{-1}\boldsymbol{\sigma} \ , \tag{2.13}$$

while the elastic strain energy of the equivalent undamaged material Λ_0 is defined as:

$$\Lambda_0 = \frac{1}{2}\bar{\boldsymbol{\sigma}}^T\mathbf{C}^{-1}\boldsymbol{\sigma} \ . \tag{2.14}$$

Thus, by using energy equivalence and net stress definition (Eq.2.5), the material damaged stiffness matrix $\tilde{\mathbf{C}}$ results:

$$\tilde{\mathbf{C}} = (1 - D)^2 \mathbf{C} \ , \tag{2.15}$$

and, consequently, the effective stress is:

$$\tilde{\boldsymbol{\sigma}} = \mathbf{C}\boldsymbol{\varepsilon} = \frac{1}{(1 - D)^2} \tilde{\mathbf{C}}\boldsymbol{\varepsilon} \ . \tag{2.16}$$

2.3.2 Smeared crack models

Rashid (1968) introduced the smeared crack formulation for concrete fracture. Conversely from the discrete approach (Blaauwendraad and Grootenboer, 1981; Blaauwendraad, 1985) where a crack is modeled as a geometrical discontinuity, this considers the medium, where different cracks are present, as a *continuum* material (Rots, 1988). The approach starts with the notion of stress and strain and permits a description in terms of stress-strain relations. Similar to plasticity, which will be investigated in Section 2.3.3, in smeared formulation a decomposition of the total strain into an elastic part, and an inelastic part called the crack strain is used. Instead of postulating a yield condition and a flow rule, the inelastic strain due to crack opening is related directly to the traction transmitted across the crack plane.

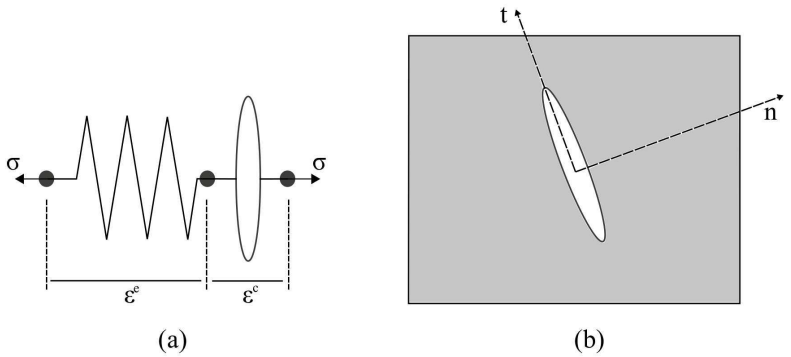

Figure 2.40: From Jirásek (2011): (a) Schematic representation of smeared crack model as an elastic unit coupled in series to a crack unit, (b) local coordinate system aligned with the crack.

Smeared crack concepts can be classified into fixed and rotating smeared crack approaches. With a fixed concept, the crack orientation is fixed during the entire computational process. In contrast, a rotating approach allows the crack's orientation to co-rotate with principal strain axes. Principal features of this approach, considering a one-dimensional model, will be pointed out to understand better the constitutive laws that will be used and modified in Chapter 4 of this thesis. As highlighted before, smeared crack model decomposes the total strain into two parts, one corresponds to the deformation of the uncracked material, and the other is the contribution of cracking. A general nonlinear material law can rule the uncracked material's response, but it is ordinarily considered linear elastic. In one dimension setting, the strain decomposition is written as:

$$\varepsilon = \varepsilon^e + \varepsilon^c \ , \tag{2.17}$$

and the elastic strain ε^e is related to stress by Hooke's law:

$$\sigma = E\varepsilon^e \ . \tag{2.18}$$

The crack strain, ε^c, represents in a smeared manner the additional deformation due to the opening of cracks. The additive strain decomposition corresponds to a rheological model in which an elastic spring is linked in series with a unit describing the crack's contribution, as shown in Figure 2.40 (a) (Jirásek, 2011). Since the coupling is serial, both units transmit the same stress, σ. Originally, the material is considered in its virgin state, the crack strain vanishes, and the overall response is linear elastic. A crack is started when the stress reaches the material's tensile strength. A constitutive law rules the stress evolution after a first crack is formed. It was assumed that the traction sent by the crack drops to zero instantly after crack initiation. On the structural level, such an approach leads to results that are not objective regarding the mesh size, as will be explained in Section 2.4. To ensure proper energy dissipation and avoid unrealistic stress jumps, it is needed to describe the loss of cohesion as a gradual process. This phenomenon is physically supported because the formation of a macroscopic stress-free crack is in a heterogeneous material preceded by the initiation, growth, and coalescence of a network of microcracks. For modeling, we replace such a complex system of small

non-contiguous cracks with an equivalent cohesive crack, which can still transmit stress. This cohesive stress is then considered a function of the crack strain,

$$\sigma = f^c(\varepsilon^c) \tag{2.19}$$

where the appropriate form of the function f^c should be identified from experiments. The three equations (2.17, 2.18, 2.19) fully define the one dimensional smeared crack model (provided that the strain increases monotonically). It should be noted that considering a real material, in a general multi-dimensional setting, microcracks have different sizes, shapes, and orientations. They are not necessarily planar, and their faces are rough. It is useful for the formulation of these models (see Section 4), to introduce local coordinates aligned with the crack (see Figure 2.40 (b)). The initiation criterion should also specify the initial orientation of the crack. Traditional smeared crack models control crack initiation by the Rankine criterion of maximum principal stress.

2.3.3 Plasticity models

The origins of the theory of plasticity can be chased back to the middle of the nineteenth century. Following the substantial development that took place, particularly in the first half of the twentieth century, this theory is set on sound mathematical foundations. It is considered as one of the most successful phenomenological constitutive models of solid materials. Materials whose behavior can be properly described by plasticity theory are called plastic (or rate-independent plastic) materials. Basically, after being subjected to a loading program, these materials may sustain permanent or plastic deformations when completely unloaded. Here the theory described is restricted to infinitesimal deformations, and just the most important concepts and mathematical expressions are reviewed. A more comprehensive treatment of the theory of plasticity can be found in de Souza Neto et al. (2011). From a phenomenologic point of view, plastic materials share some important features of their behavior. As addressed in de Souza Neto et al. (2011), a brief description of such common features can be given using a uni-axial tension experiment with a metallic bar.

Typically, uni-axial tension tests with ductile metals produce stress–strain

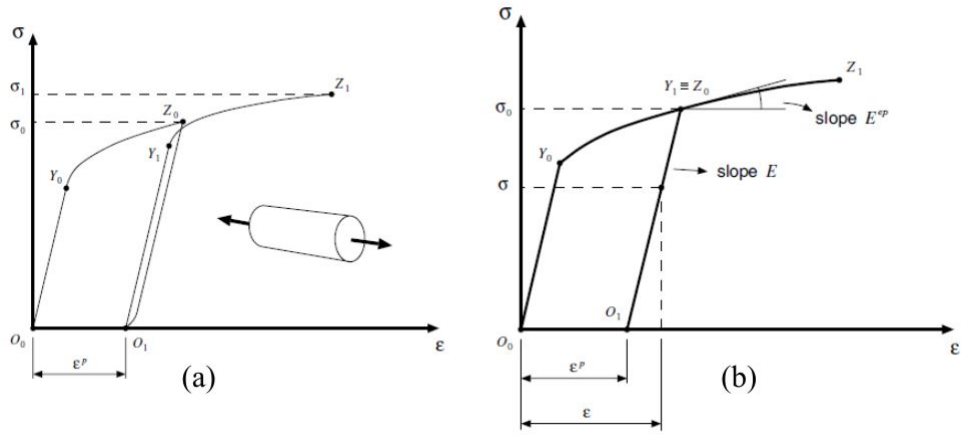

Figure 2.41: (a) Uniaxial tension experiment with ductile metals and (b) Uniaxial tension mathematical model (de Souza Neto et al., 2011).

curves of the type shown in Figure 2.41 (a). Some significant phenomenological properties can be distinguished:

- The existence of an elastic domain, i.e., a range of stresses within which the material's behavior can be considered as purely elastic, without the evolution of permanent (plastic) strains. The so-called yield stress delimits the elastic domain. In Figure 2.41 (a), segments O_1Y_0 and O_1Y_1 define the elastic domain at two different states. The associated yield stresses correspond to points Y_0 and Y_1;
- If the material is more loaded at the yield stress, then plastic yielding (or plastic flow), i.e., evolution of plastic strains, occurs;
- Following the evolution of the plastic strain, an evolution of the yield stress itself is also seen. This phenomenon is known as hardening.

The microscopic mechanisms that give rise to these common phenomenological properties can be quite distinguished for different material types. However, the goal of the mathematical theory of plasticity is to afford constitutive continuum models able of describing with sufficient accuracy the phenomenological behavior

of materials that possess the characteristics discussed in the above. As an example, the constitutive equations for an overall one-dimensional plasticity model, following the uni-axial experiment test are described.

Referring to Figure 2.41 (b), that shows an idealized version of 2.41 (a), the model is defined, as follow:

- Elastoplastic split of the axial strain into the sum of an elastic component ε_e and a plastic component ε_p is one of the chief hypotheses:

$$\varepsilon = \varepsilon_e + \varepsilon_p \ ; \tag{2.20}$$

  where the elastic strain is defined as:

$$\varepsilon_e = \varepsilon - \varepsilon_p \ ; \tag{2.21}$$

- Following the definition of the elastic axial strain, the constitutive law for the axial stress can be expressed as:

$$\sigma = E\varepsilon_e \ ; \tag{2.22}$$

- A yield criterion stated using a yield function has to be introduced to define the elastic domain delimited by yield stress;

$$\Phi(\sigma, \sigma_y) = |\sigma| - \sigma_y \ ; \tag{2.23}$$

- A plastic flow rule has to be addressed, defining the evolution of the plastic strain;

$$\dot{\varepsilon}^p = \dot{\gamma} sign(\sigma) \ ; \tag{2.24}$$

- A hardening law has to be defined, characterizing the evolution of the yield limit.

$$\sigma_y = \sigma_y(\bar{\varepsilon}^p) \qquad \bar{\varepsilon}^p = \dot{\gamma} \ . \tag{2.25}$$

The most common plasticity developed models used in masonry analysis are based on Tresca, von Mises, Mohr-Coulomb, and Drucker-Prager criteria. Literature models are i.e. Lourenço et al. (1997); Oliveira and Lourenço (2004); Saritas and Filippou (2009).

2.4 Overview of localization problems and regularization techniques

Laboratory experiments show that, when loaded at a constant strain rate under either uni-axial or multi-axial stress conditions, masonry materials' responses are characterized phenomenologically by a constitutive response in which stress increases monotonically with strain to a peak value and then decreases with further increase in strain characterized by localized deformation. This phenomenon is called "strain softening" and, as already mentioned in Section 2.1.1, is a typical masonry material behavior. A salient feature of strain softening is that the tangent modulus becomes negative. Strain softening is usually co-occurred with localized deformation. However, finite element analysis with strain softening models, based on classical theory of continuum mechanics, usually suffers from pathological mesh dependence. The so-called mesh dependence means two aspects: one is that the size of the localization zone becomes small with refined finite element mesh; another is that the load-displacement responses are associated with the mesh size and do not have converge to a meaningful and unique solution. Such drawbacks are a consequence of the loss of the mathematical problem well-posedness, which appears using the classical local constitutive laws for softening materials. Ill-posed problems can be regularized using different methods presented in the open literature: Cosserat or micro-polar models (De Borst, 1991; Addessi, 2014); higher-order gradient models (Peerlings et al., 1996; Addessi et al., 2002); integral type nonlocal models (Pijaudier-Cabot and Bazant, 1987; Toti et al., 2015); changing the mesh topology in anticipation of material failure; fracture energy models (Lourénço et al., 1997; Comi and Perego, 2001). Before entering the description of two possible solutions, adopted in this thesis known as fracture energy regularization approach and nonlocal integral regularization technique, the problem's

nature is explained briefly, through a one dimension example. Later, in Chapter 5, will be demonstrated and studied the pathological sensitivity of the numerical results to the discretization, referring to multiple dimensions cases.

2.4.1 Strain localization due to softening

A simple one-dimensional localization problem is reported from Jirásek (2002), to demonstrate the pathological sensitivity of the numerical results to the discretization. Consider a bar of a constant cross section A and total length L under uni-axial tension (see Figure 2.42).

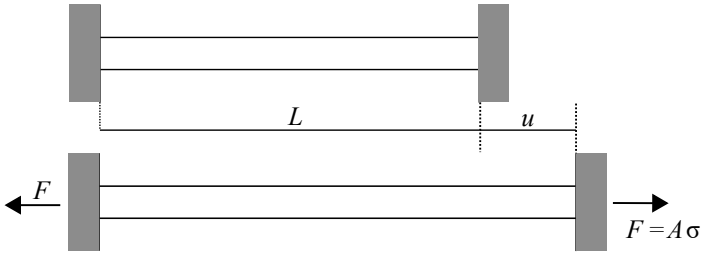

Figure 2.42: Bar under uni-axial tension (Jirásek, 2002).

A bi-linear stress-strain constitutive relation with linear elastic behavior up to the peak stress, f_t (damage-onset strength) followed by linear softening, (see Figure 2.43 (a)), is assumed to represent the material response.

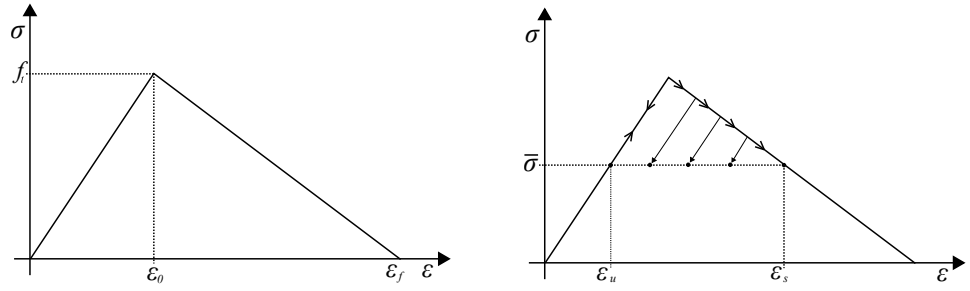

Figure 2.43: (a) Stress-strain diagram with linear softening and (b) two strain values corresponding to the same stress level (Jirásek, 2011).

If $\varepsilon_0 = f_t/E$, where E is Young's modulus of elasticity, the peak stress is achieved. The tensile strain at which, after the damage onset, the transmitted

stress disappears (tensile failure strain) is denoted by ε_f. When a displacement u is applied at one of the supports, the response continues linear elastic up to peak stress $\sigma = f_t$. After the peak stress, the resistance of the bar starts decreasing. At each cross-section, stress can reduce either at increasing strain (softening behavior) or decreasing strain (elastic unloading). The equation of equilibrium implies that the stress profile must rest uniform along the bar. However, at any given stress level $\bar{\sigma}$ between zero and f_t, there are two values of strain ε_s and ε_u or which the constitutive equation is satisfied, Figure 2.43 (b), and so the strain profile does not have to be uniform. Indicating by L_s the cumulative length of the softening regions and by $L_u = L - L_s$ the cumulative length of the unloading regions, the material, for example, can be softening in an interval of lengths L_s and unloading everywhere else in an interval of length L_u. When the stress is quite relaxed to zero, the strain in the softening region is $\varepsilon_s = \varepsilon_f$ and, the strain in the unloading region is $\varepsilon_u = 0$.

Therefore, the total bar elongation is $u_f = L_s\varepsilon_s + L_u\varepsilon_u = L_s\varepsilon_f$. Still, the softening region length L_s remains undetermined and can take any value within the interval $[0, L]$. However, it means that the structural problem has infinitely many solutions. The corresponding post-peak branches of the load-displacement diagram fill the fan shown in Figure 2.44.

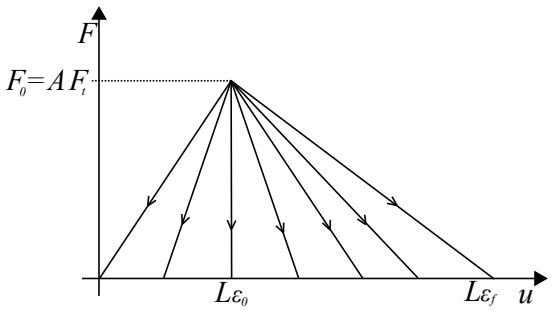

Figure 2.44: Fan of possible post-peak branches of the load-displacement diagram (Jirásek, 2011).

The uncertainty in the length L_s of the softening regions is removed if imperfections are taken into account. The imperfections can be associated with the material (its properties are non-uniform) or the bar geometry (sectional bar dimensions are non-uniform). If the strength in a small region is assumed lightly

lower than in the remaining portion of the bar, when the applied stress reaches the reduced strength, softening starts, and the stress decreases; consequently, the material outside the weaker region must unload elastically because its strength has not been exhausted. Therefore if the loading process is done on a bar with geometric or material imperfections, the strain will localize in the weakest cross-section combined with vanishing energy dissipation. As stated above, it's possible to conclude that the softening region size cannot exceed its size with minimum strength. However, the region with minimum strength can be arbitrarily small, and the corresponding softening branch can be arbitrarily close to the elastic branch of the load-displacement diagram. Therefore, as explained by (Jirásek, 2011), the standard local damage model accounting for strain-softening leads to a solution that has several problems: (1) the region of material softening is infinitely small; (2) the load-displacement diagram always exhibits snap-back, independently of the structural size and the material ductility; (3) the total amount of energy dissipated during the failure process is zero.

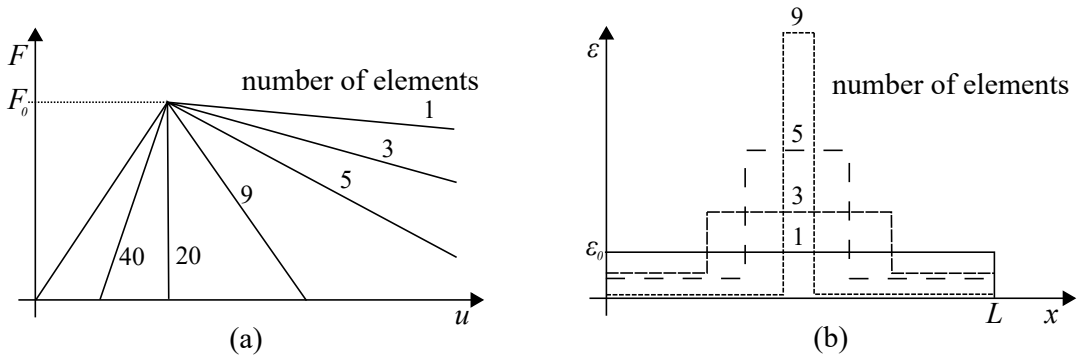

Figure 2.45: Effect of mesh refinement on the numerical results: load-displacement diagrams and strain profiles (Jirásek, 2011).

To summarize, as noticed before in the introduction, from the mathematical point of view, these problems are linked to the so-called *loss of ellipticity* of the governing differential equation, which occurs when the tangent modulus, after peak-stress, ceases to be positive. The boundary value problem becomes ill-posed; i.e., it does not have a unique solution with continuous dependence on the given data. From the numerical point of view, ill-posedness is manifested by the sensitivity of the results to the size of finite elements. If finite elements discretize

a bar and the numerical algorithm suitably captures the localized solution, the softening region extends over one element. The slope of the post-peak branch depends on the number of elements, see Figure 2.45.

2.4.2 Fracture energy regularization

The fracture energy method is frequently used in engineering applications based on an adjustment of the stress-strain diagram depending on the element's size. This technique was originally introduced for softening plasticity (Pietruszczak and Mroz, 1981), but it is best described in the context of crack models (Bažant and Oh, 1983). Before going to explain the theory for the last models, a general definition is reported. The method assumes that dissipation within the single element has to be independent of the element size. To this end, the stress-strain curve is properly modified. The energy dissipated in the finite element is equal to G_f, assigned value in tension and compression (previously defined in Section 2.1.1.2). A characteristic length h^e is defined for each element, which depends on the size, shape, and interpolation function of the used finite element. The specific fracture energies g_f, defined in Eq. 2.26, is then scaled so that it results $g_f h^e = G_f$ for each element (Comi and Perego, 2001),with:

$$g_f = \int_{\varepsilon_0}^{\varepsilon_u} \sigma(\varepsilon) d\varepsilon + \tfrac{1}{2}\sigma_0\varepsilon_0 \tag{2.26}$$

With particular notice to smeared crack models, in a fracture process, the inelastic part of deformation is due to the opening of microcracks that later merge and form a macroscopic crack. These models design the inelastic deformations as the cracking strain. Still, the material can be treated as a continuum. Nevertheless, as the crack opening is a displacement discontinuity, it must be modified into an equivalent strain by smearing over a particular distance in reality. Naturally, the numerical results agree to reality only if the simulated softening region's width is equal to the smearing distance. As addressed by Jirásek (2011), the technique to be described adjusts the curve slope that represents the inelastic behavior depending on local mesh characteristics, i.e., it works with a mesh-adjusted softening modulus. Here a simple case is described to understand the method better. A discrete crack, considering for simplicity just the normal component and a uni-axial

situation, can be described by traction law in the general form:

$$\sigma = f^w(w) \ ; \tag{2.27}$$

where w is the crack opening and σ the stress component normal to the crack. If the crack opening is smeared over a distance h, the resulting cracking strain is

$$\varepsilon_c = \frac{w}{h} = \frac{\tilde{f}^w}{h}; \tag{2.28}$$

where $\tilde{f}^w$ is the inverse function of f^w. Equation 2.28 combined with the elastic law $\varepsilon_e = \frac{\sigma}{E}$ gives the inverse stress-strain relation:

$$\varepsilon = \varepsilon^e + \varepsilon^c = \frac{\sigma}{E} + \frac{\tilde{f}^w}{h}; \tag{2.29}$$

describing the softening branch of the stress-strain diagram. In multiple dimensions, the correct value of h is influenced by the mesh size and the inclination of the crack band (generally inelastic strain localized in a band of element) to the mesh line. Based on this type of evidence and on numerical experiments, Rots (1988) suggested certain rules for choosing the equivalent element size, h, for several typical situations. A more rigorous approach was developed by Oliver (1989). In practical simulations, it seems reasonable to compute h as the size of the element projected onto the crack normal. This estimate can be developed by applying a correction factor proposed by Červenka et al. (2005).

2.4.3 Nonlocal integral regularization

As addressed by Addessi (2000) this approach is certainly considered more general and rational. Considering a continuous model, the locality hypothesis is removed, where the response at a point of the material depends only on the values that a certain set of constitutive variables assumes at that point. The idea is to extend the physical field of classical continuous models, adopting a generalized continuous approach, in which an internal length measure is introduced. Continuous nonlocal models take into account the complex interaction mechanisms existing in the progressive degradation of materials. They are based on the idea that, in the

presence of the high gradients of damage and deformation, which characterize the localization phenomena, the response at a point of the material is influenced, in a certain way, by the mechanical behavior around it. Such models for materials with heterogeneous microstructure were developed and originally applied to elastic materials, considering the tension at a point as a function of the deformation, defined as the mean of the distribution over a certain material representative volume (see figure 2.46) centered in the same point. The scatter of microstresses and smoothed macrostress profile demonstrates how the stress value at the center of representative volume differs from the stress corresponding to average strain over this volume.

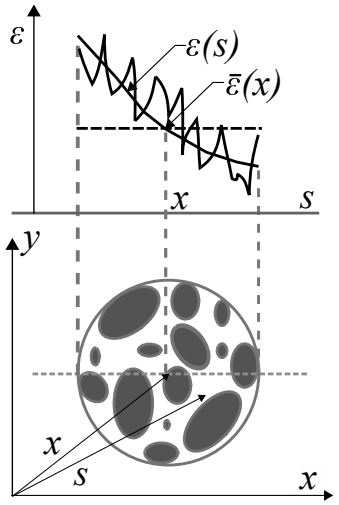

Figure 2.46: Representative volume of material used for nonlocal strain average (Bažant and Jirásek, 2002).

The formation of a crack in the center of the volume element does not depend only on the value that the deformation assumes in the center, but on the global deformation in a properly defined neighborhood, which determines the value of the deformation energy inside it. The nonlocal deformation variable at a given point $\mathbf{x}$ is defined as the weighted average on a certain volume of material Ω_r:

$$\bar{\varepsilon}(\mathbf{x}) = \frac{1}{\Omega_r(\mathbf{x})} \int_{\Omega_r} \alpha(|\mathbf{x}-\mathbf{s}|)\varepsilon(\mathbf{s}) d\Omega(\mathbf{s}) \ ; \tag{2.30}$$

where $\varepsilon(\mathbf{s})$ is the local deformation tensor, $\alpha(|\mathbf{x}-\mathbf{s}|)$ is the weight function that

depends on the distance $r = |\mathbf{x}-\mathbf{s}|$ between the point considered, with coordinates $\mathbf{x}$, and the points contributing to the mean, Ω_r is a normalized volume such that, if the deformation is uniformly distributed, the average coincides with the local value:

$$\Omega_r(\mathbf{x}) = \int_{\Omega_r} \alpha(|\mathbf{x}-\mathbf{s}|) d\Omega(\mathbf{s}) \ . \tag{2.31}$$

The weight function is such that it assumes a maximum value at point $\mathbf{x}$ and decreases as it moves away from the point itself. Generally, the bell shape is chosen for it. Typical examples are the second-order parabola, the fourth-order parabola, the cosine function, the Gaussian normal distribution function, etc. Bažant (1984) and Bazant et al. (1984), extending this logic to softening materials, developed nonlocal integral models to overcome the analytical and numerical problems related to the deformation's localization. Other types of operators have been developed and can be adopted to define the constitutive variable, such as a nonlocal average. Still, the nonlocal models of the integral type are addressed to this thesis's goal. In the original formulation of the nonlocal integral models, all the constitutive variables are defined as integral means. However, this choice entails considerable complications due to:

- the model predicts nonlocal behavior in every situation, even in the elastic or plastic field with positive hardening;
- some unstable deformation modes at zero energy may arise; in this case, it is necessary to superimpose a continuous local model.

The models developed later are based on the idea that only the variables that control the softening behavior should be defined as nonlocal. Regarding the elastic part of the deformation, it is appropriate to keep the classic definition of nonlocal. In the field of damage mechanics, integral formulations have been extensively studied and applied to numerical cases. The first models proposed (Pijaudier-Cabot and Bažant, 1987) are based on the nonlocal definition of the variable Y, which controls the evolution of the damage D, identified, in this specific case, with the strain energy. The latter is therefore replaced in the model by its integral mean. Thus the evolution of the damage is controlled by the nonlocal variable $\bar{Y}$.

If the evolutionary equation of the damage is integrable, it appears in a functional expression as:

$$D = g(\bar{Y}) \tag{2.32}$$

Simultaneously, the damage model's load function has also been formulated in terms of the nonlocal variables. In later developments (Bažant and Pijaudier-Cabot, 1988), the authors propose to replace the damage variable D with its nonlocal definition.

$$\bar{D} = \frac{1}{\Omega_r(\mathbf{x})} \int_{\Omega_r} \alpha(|\mathbf{x}-\mathbf{s}|) D(\mathbf{s}) d\Omega(\mathbf{s}) \ ; \tag{2.33}$$

In general, it can be stated that by introducing any variable that makes the dissipation variation nonlocal, the localization of the dissipated energy in a zero-dimensional volume is avoided. It should be noted that near the analyzed medium's contour, a portion Ω^* of the representative volume Ω_r can come out of the same contour. For points belonging to Ω^*, the previous definition has been replaced with the following one.

$$\bar{Y} = \frac{1}{\Omega_r - \Omega^*} \int_{\Omega_r - \Omega^*} \alpha(|\mathbf{x}-\mathbf{s}|) D(\mathbf{s}) d\Omega(\mathbf{s}) \ . \tag{2.34}$$

In the case of a body with infinite extension, the representative volume Ω_r is equal to the length l for a one-dimensional continuum, to the area of a circle of diameter l for a two-dimensional continuum, to the volume of a sphere of diameter l for a three-dimensional continuum. The length l, called characteristic length, represents the material's property and is the same order of magnitude of the inhomogeneity (Rodrıguez-Ferran et al., 2004; Toti et al., 2015; Tesei and Ventura, 2016).

Chapter 3

Micromechanical finite element modeling of masonry structures

This section describes a damage-plastic model for the micromechanical analysis of 2D masonry structures. First, the existing constitutive law (Sacco, 2009) is illustrated. A new user finite element, modified and enriched to describe masonry curved geometry and the occurring damage and friction plasticity mechanisms is introduced and the main aspects related to the finite element implementation are presented. A comparison between numerical and experimental outcomes is performed for masonry walls to validate the model. Lastly, the static response of masonry arches is studied. Numerical results are validated by comparison with experimental outcomes, and parametric numerical studies investigate the influence of geometry and material mechanical parameters.

3.1 Damage-plastic model

According to the micromechanical approach, bricks and mortar are separately modeled, assuming that nonlinear mechanisms are localized at mortar joints. Thus, a linear elastic stress–strain relationship is assumed for blocks, as:

$$\boldsymbol{\sigma}^b = \mathbf{C}^b \boldsymbol{\varepsilon}^b \tag{3.1}$$

where $\boldsymbol{\sigma}^b = \left\{\sigma_1^b \, \sigma_2^b \, \tau_{12}^b\right\}^T$ and $\boldsymbol{\varepsilon}^b = \left\{\varepsilon_1^b \, \varepsilon_2^b \, \gamma_{12}^b\right\}^T$ are the brick stress and strain vectors, respectively, and $\mathbf{C}^b$ denotes the elastic isotropic constitutive matrix for plane-stress condition, equal to:

$$\mathbf{C}^b = \frac{E}{(1-\nu^2)} \begin{bmatrix} 1 & \nu & 0 \\ \nu & 1 & 0 \\ 0 & 0 & \frac{(1-\nu)}{2} \end{bmatrix} \tag{3.2}$$

As for the mortar, the damage-friction law proposed by Sacco (2009) is adopted, accounting for damage, unilateral contact and friction plasticity mechanisms. This permits to describe flexural and shear failure mechanisms typical of masonry structural elements (Addessi and Sacco, 2016a,b, 2018).

In the existing formulation, the model was capable of reproducing the flexural and shear mechanisms related to fracture mode I and mode II, as illustrated in Figure 3.3, only considering the vertical and horizontal mortar joints. A local coordinate system was introduced with T and N denoting the parallel and normal directions to the mortar joint, respectively, as shown in Figure 3.1.

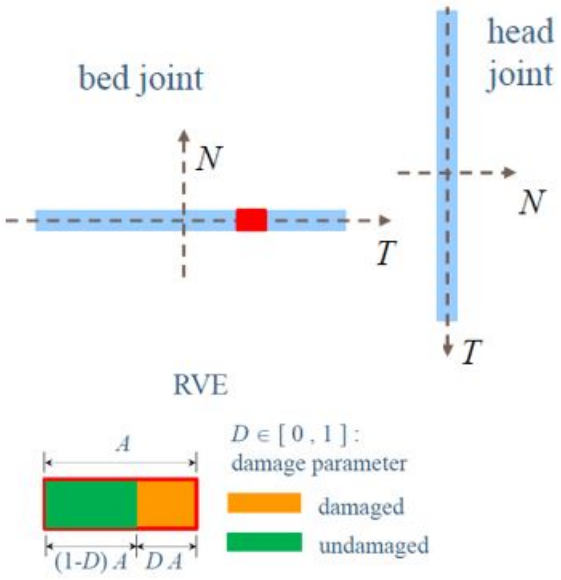

Figure 3.1: Mortar joints: local axis x_T -x_N.

Here, the model is extended to consider arbitrarily oriented joints. To this end, a new local coordinate system (x_T, x_N), shown in Figure 3.2, is introduced according to the arbitrary inclination of the mortar joint. Again T and N denote the parallel and normal directions to the mortar joint, respectively. Then, the mortar constitutive law is written considering the intrinsic reference system defined according to the actual joint rotation.

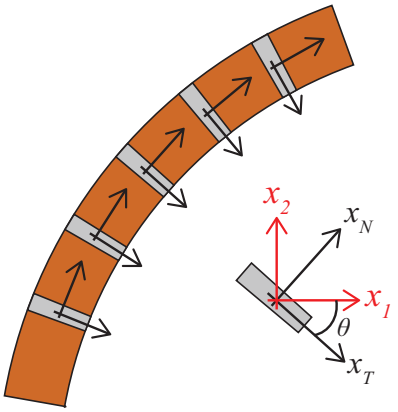

Figure 3.2: Mortar joints: local axis x_T -x_N .

The local strain vector, $\boldsymbol{\varepsilon} = \{\varepsilon_T\, \varepsilon_N\, \gamma_{NT}\}^T$, is evaluated on the basis of that referred to the global reference system, $\boldsymbol{\varepsilon}_G = \{\varepsilon_1\, \varepsilon_2\, \gamma_{12}\}^T$, by means of the standard transformation rule:

$$\boldsymbol{\varepsilon} = \mathbf{R}\boldsymbol{\varepsilon}_G \tag{3.3}$$

where $\mathbf{R}$ is the rotation matrix expressed as functions of the angle θ between the axes x_T and x_1 (Figure 3.2) and equal to:

$$\mathbf{R} = \begin{bmatrix} cos^2\theta & sin^2\theta & cos\theta sin\theta \\ sin^2\theta & cos^2\theta & -cos\theta sin\theta \\ -2cos\theta sin\theta & 2cos\theta sin\theta & cos^2\theta - sin^2\theta \end{bmatrix} \tag{3.4}$$

Accordingly, the stress vector $\boldsymbol{\sigma} = \{\sigma_T\, \sigma_N\, \tau_{NT}\}^T$ is introduced and the constitutive law is expressed as:

$$\boldsymbol{\sigma} = \mathbf{C}^m(\boldsymbol{\varepsilon} - \boldsymbol{\pi}) \tag{3.5}$$

being $\mathbf{C}^m$ the mortar elastic stiffness matrix equal to:

$$\mathbf{C}^m = \begin{bmatrix} C^m_{TT} & C^m_{NT} & 0 \\ C^m_{NT} & C^m_{NN} & 0 \\ 0 & 0 & G^m \end{bmatrix} \tag{3.6}$$

and $\boldsymbol{\pi}$ the vector of the inelastic strains accounting for damage, D, unilateral contact, $\boldsymbol{c}$, and slip, γ^p_{NT}, defined as:

$$\boldsymbol{\pi} = D(\boldsymbol{c} + \boldsymbol{\varepsilon}^P) \tag{3.7}$$

where $\boldsymbol{c}$ and $\boldsymbol{\varepsilon}^P$ are the contact and friction strain vector, respectively:

$$\boldsymbol{c} = \begin{Bmatrix} h(\varepsilon_N)\varepsilon_T \\ h(\varepsilon_N)\varepsilon_N \\ 0 \end{Bmatrix} \quad \boldsymbol{\varepsilon}^P = \begin{Bmatrix} 0 \\ 0 \\ \gamma^p_{NT} \end{Bmatrix} \tag{3.8}$$

In Eq. (3.7), $h(\varepsilon_N)$ is the Heaviside function ($h(\varepsilon_N) = 1$, if $\varepsilon_N \geq 0$, and $h(\varepsilon_N) = 0$ otherwise), introduced to model the unilateral effect phenomenon under reversal loadings. Indeed, brittle-type materials, like masonry, exhibit stiffness recovery due to the re-closure of tensile cracks when the material undergoes compressive states. The damage variable D in Eq. (3.7) takes into account fracture modes I and II. To this end, quantities η_N and η_{NT} are introduced as:

$$\eta_N = \frac{\varepsilon_{N,0}\,\sigma_{N,0}}{2g_{cI}} \qquad \eta_{NT} = \frac{\gamma_{NT,0}\,\tau_{NT,0}}{2g_{cII}} \tag{3.9}$$

which depend on the first cracking strains, $\varepsilon_{N,0}$ and $\gamma_{NT,0}$, on the peak values of the normal and shear stresses, $\sigma_{N,0}$ and $\tau_{NT,0}$, and on the specific fracture energies g_{cI} and g_{cII} for mode I and mode II, respectively.

In Figure 3.3 the normal and shear stress–strain relationships are illustrated. To formulate the damage evolution problem, the following damage associated variable is defined:

$$\beta = \sqrt{\left(\frac{\langle \varepsilon_N \rangle_+}{\varepsilon_{N,0}}\right)^2 + \left(\frac{\gamma_{NT}}{\gamma_{NT,0}}\right)^2} - 1 \tag{3.10}$$

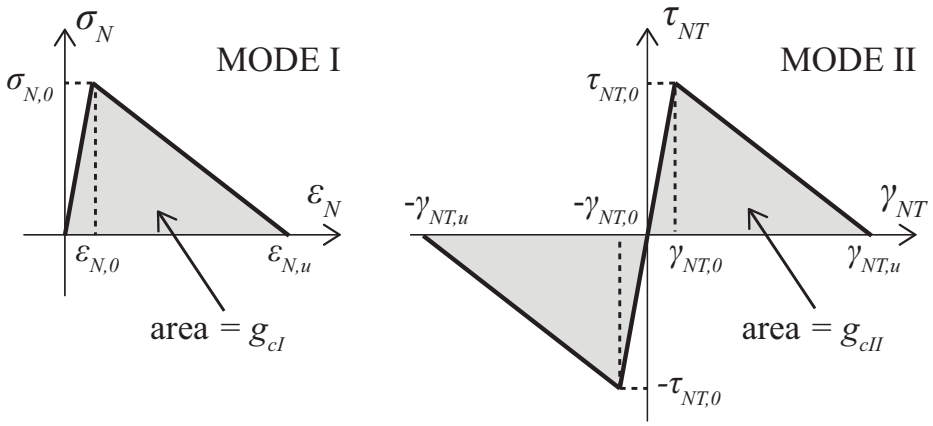

Figure 3.3: Mortar joints: constitutive laws for mode I and mode II.

on the basis of which the damage variable evolution law is stated as:

$$D = \max_{hist} \left\{ 0 \, , \min \left\{ 1, \frac{1}{\eta} \left(\frac{\beta}{1+\beta} \right) \right\} \right\} \tag{3.11}$$

with:

$$\eta = 1 - \frac{1}{\alpha^2} \left[\langle \varepsilon_N \rangle_+^2 \, \eta_N + (\gamma_{NT})^2 \eta_{NT} \right] \tag{3.12}$$

measuring the coupling of the two fracture modes and $\alpha = \sqrt{\langle \varepsilon_N \rangle_+^2 + (\gamma_{NT})^2}$ with the Macaulay's brackets $\langle \bullet \rangle_+$ selecting the positive part of the quantity $\bullet$.
As evident from Eq. (3.11), the damage variable D is evaluated as the maximum value attained during the loading history, so that to satisfy the thermodynamic irreversibility condition of the degrading process.
To govern the evolution of the inelastic slip strain γ_{NT}^p, modeling the frictional mechanisms at the interface between mortar and bricks and occurring only if damage is activated, the classical Coulomb yield function is adopted, that reads:

$$\varphi(\boldsymbol{\sigma}^d) = \mu \sigma_N^d + |\tau_{NT}^d| \tag{3.13}$$

being μ the friction parameter and $\boldsymbol{\sigma}^d$ the stress defined on the mortar joint damaged part (Sacco, 2009). Eventually, to completely solve the plastic problem,

the following non-associated flow rule is considered:

$$\dot{\gamma}^p_{NT} = \dot{\lambda}\frac{\tau^d_{NT}}{|\tau^d_{NT}|} \tag{3.14}$$

together with the classical loading-unloading Kuhn-Tucker conditions

$$\dot{\lambda} \geqslant 0, \quad \varphi(\boldsymbol{\sigma}^d) \leq 0, \quad \dot{\lambda}\varphi(\boldsymbol{\sigma}^d) = 0 \tag{3.15}$$

3.1.0.1 Nonlocal regularization

To overcome the mesh-dependency problem occurring when strain-softening constitutive laws are introduced in the FE formulation, a regularization technique, based on the nonlocal integral approach, is adopted. According to this formulation, the nonlocal strain $\bar{\boldsymbol{\varepsilon}}$ at point $\mathbf{x}$ of the k-th mortar joint is evaluated as:

$$\bar{\boldsymbol{\varepsilon}}(\mathbf{x}) = \frac{1}{\int_{\Omega^k}\psi(\mathbf{x},\mathbf{y})d\Omega^k(\mathbf{y})}\int_{\Omega^k}\psi(\mathbf{x},\mathbf{y})\boldsymbol{\varepsilon}(\mathbf{y})d\Omega^k(\mathbf{y}); \tag{3.16}$$

where Ω^k denotes the area of the mortar joint k. The weight function ψ, measuring the influence of the generic point placed at $\mathbf{y}$ on the analyzed point located at $\mathbf{x}$, is assumed as the classical Gaussian:

$$\psi(\mathbf{x},\mathbf{y}) = e^{-\left(\frac{\|\mathbf{x}-\mathbf{y}\|}{l_c}\right)^2} \tag{3.17}$$

being l_c the nonlocal radius related to the characteristic length of the mortar. To be noted is that no interaction between the different joints is accounted for.
Once the nonlocal strain in Eq. (3.16) is evaluated, this is used to define quantities η, β and α in Eqs. (3.10), (3.12) and, consequently, to solve the damage evolution problem.

3.1.1 Computational aspects

In this section computational aspects concerning the evaluation of the solution of the micromechanical problem are discussed. A new user FE is implemented in the FEAP code (Taylor, 2017), formulated on the basis of the presented gen-

eralized version of the constitutive law. Isoparametric quadrilateral 4-node FEs are introduced, each equipped with two translation displacement degrees of freedom, to model mortar and bricks. The adopted FE procedure is standard. First the strain vector $\boldsymbol{\varepsilon}_G$, in the global coordinate system is computed, starting from element nodal displacement $\mathbf{u}^e$. Matrix $\mathbf{L}^e$ is defined as $\mathbf{L}^e = \mathbf{D}_x\mathbf{N}^e$, where $\mathbf{N}^e$ contains the $2D$ displacement shape functions, referred to the 4 element nodes, while matrix $\mathbf{L}^e = \mathbf{D}_x\mathbf{N}^e$ contains their derivatives according to the 2D compatibility operator, $\mathbf{D}_x$. Then, the local strains are evaluated by applying the rotation inverse matrix $\mathbf{R}^{-1}$ defined in Eq. 3.4. Subsequently, the nonlocal strain $\bar{\boldsymbol{\varepsilon}}$ at point $\mathbf{x}$ of the k-th mortar joint is evaluated by using Eq. (3.16). Then the evolutionary problems of the damage and plastic variables governing the constitutive response are solved at each of the 2×2 quadrature points. To this aim, a predictor-corrector algorithm is followed. At the current iteration $k+1$, the strains are estimated. Based on these, the damage associated variable β^{k+1} is computed, together with parameter η^{k+1} governing the coupling of fracture modes I and II. Then, the damage variable D^{k+1} is updated. After that, the unilateral contact problem is solved by evaluating the Heaviside function $H(\varepsilon_N^{k+1})$ and c^{k+1} the contact vector. Finally, if the mortar is affected by the damaging process, the friction problem is resolved by adopting a prediction-correction technique. A trial prediction of the plastic strains is computed by setting their values equal to those evaluated at the previous time step t_n. The trial normal and shear stresses are then evaluated, based on which the trial yield function $f^{k+1,tr}$ is calculated. The correction phase is performed if $f^{k+1,tr} > 0$. Once the damage, the unilateral contact and the friction problems are solved, the values of the inelastic strains are updated. The scheme of the described solution algorithm is reported in Table 3.2. Lastly, the stress vector in the local coordinate system is computed and by using the rotation matrix $\mathbf{R}$, the global stress vector is obtain as $\boldsymbol{\sigma}_G = \mathbf{R}\boldsymbol{\sigma}$. The scheme of the described procedure is reported in Table 3.1.

1. Compute strains $\boldsymbol{\varepsilon}_G$ starting from displacements $\mathbf{u}^e$:
   $\boldsymbol{\varepsilon}_G = \mathbf{L}^e \mathbf{u}^e$
2. Evaluate strains $\boldsymbol{\varepsilon}$ in the material intrinsic - coordinate system :
   $\boldsymbol{\varepsilon} = \mathbf{R}^{-1} \boldsymbol{\varepsilon}_G$
3. Calculate the nonlocal damage associated variable $\bar{\boldsymbol{\varepsilon}}$ by using Eq.(3.16)
4. Solve damage-friction evolution problem according to Table 3.2
5. Compute stresses $\boldsymbol{\sigma}$:
   $\boldsymbol{\sigma} = \mathbf{C}^m (\boldsymbol{\varepsilon} - \boldsymbol{\pi})$
6. Evaluate stresses $\boldsymbol{\sigma}_G$:
   $\boldsymbol{\sigma}_G = \mathbf{R} \boldsymbol{\sigma}$

Table 3.1: Computational procedure for mortar.

3.2 Response of masonry walls

To validate the proposed FE suitable to describe masonry straight and curved geometry, loaded in-plane or out-of-plane, the results two experimental campaigns on walls loaded out-of-plane are considered, analyzing both the global load-displacement response and the damage distribution. The model has been tested to evaluate the mechanisms that are hierarchically the most recurrent. The numerically obtained results from the proposed micromechanical model have been compared with a multiscale model (Addessi et al., 2020a), formulated using the same constitutive law and experimental outcomes.

First, an experimental campaign conducted by (Bellini et al., 2017) is reproduced. Three masonry walls reinforced with FRCM (Fiber Reinforced Cementitious Matrix) composite materials, whose geometry is shown in Figure 3.4, have been tested. The test set-up was conceived to reproduce a six-point bending scheme; each wall was pinned at the bottom and top edge. Four equal forces were applied orthogonal to the wall plane utilizing distribution beams. Lateral edges of the wall were not restricted, and two rigid supports separated bottom and top edge from the hinges used to reproduce the supported configuration (Figure 3.6).

Iteration '$k+1$'
Damage evaluation - strains $\varepsilon_N^{k+1}, \quad \varepsilon_T^{k+1}, \quad \gamma_{NT}^{k+1}$ - damage associated variable β^{k+1} (Eq. (3.10)) - combination parameter of mode I and II η^{k+1} (Eq. (3.12)) - damage D^{k+1} (Eq. (3.11))
Unilateral effect evaluation if $\varepsilon_N^{k+1} \leq 0$ then $H\left(\varepsilon_N^{k+1}\right) = 0$ else $H\left(\varepsilon_N^{k+1}\right) = 1$ - inelastic contact vector $\mathbf{c}^{k+1}$ (Eq. (3.8))
Sliding friction plasticity evaluation if $D^{k+1} > 0$ - Prediction phase $\gamma_{NT}^{p,k+1,tr} = \gamma_{NT}^{p}$ -trial yield function $f^{k+1,tr} = \mu\, \sigma_N^{d^{k+1,tr}} + \lvert\tau_{NT}^{d^{k+1,tr}}\rvert$ -check sliding friction if $f^{k+1,tr} < 0 \Rightarrow \Delta\gamma_{NT}^{P} = 0$ else - Correction phase $\Delta\lambda^{k+1} = \frac{1}{G_m} f^{k+1,tr}$ with $\Delta\gamma_{NT}^{p,k+1} = \lambda^{k+1} \frac{\tau_{NT}^{d,k+1}}{\lvert\tau_{NT}^{d,k+1}\rvert}$

Table 3.2: Damage-friction solution procedure .

Each wall was subjected to an axial load equal to 60 kN applied through hydraulic jacks located at the top of the upper hinge.

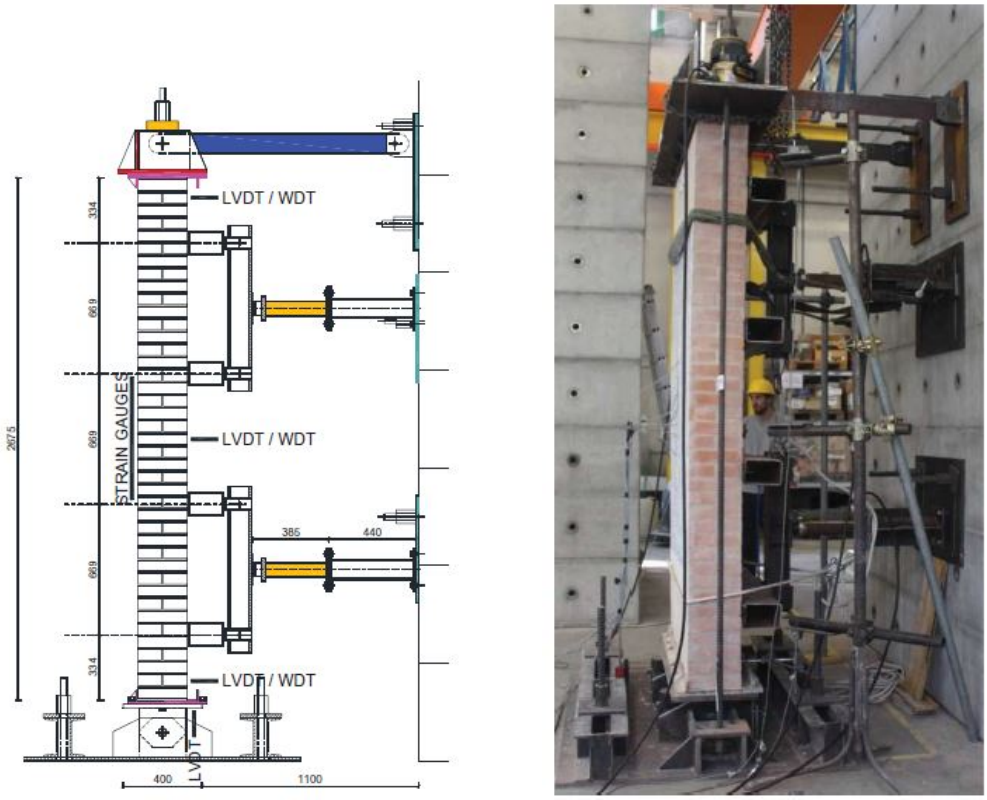

(a) (b)

Figure 3.4: Out-of-plane test set-up. (Bellini et al., 2018).

The test process was as follows:

- application of the axial load;
- installation of the FRCM reinforcement layer;
- application of the transverse forces, performing an initial loading cycle for a small maximum load level;
- transverse forces increased until specimen failure.

The wall investigates is denoted GFRCM-02. The numerical responses for an unreinforced wall with the same geometric/mechanical properties are also analyzed. Because of symmetry, only half of the wall is modeled. A plane stress formulation, above mentioned in section 3.1.1 with a 2D four-point quadrilateral FEs and within a 2x2 Gauss integration rule is adopted. The mechanical parameters used for brick and mortar are indicated in Table 3.3, deduced from the experimental measurements contained in the reference paper. The mortar nonlocal radius, l_c, is set equal to the joint thickness 25 mm, assumed as mortar characteristic length. The transverse forces are monotonically increased; that is, the initial loading cycle is neglected, as, in this loading phase, the wall remains in a linear elastic material range.

Mechanical material parameters

E^b [MPa]	E^m [MPa]	$\sigma_{N,0}$ [MPa]	$\tau_{NT,0}$ [MPa]	g_{cI} [MPa]	g_{cII} [MPa]	μ
10000	2550	0.34	0.7	2.1×10^{-2}	8.7×10^{-2}	0.5

Table 3.3: Material parameters for the bricks and mortar of the masonry wall.

Then, a FRCM reinforcement is considered. This last consisted of glass fiber grids embedded in a lime-based mortar layer, 6-10 mm thick, connected to the wall face experiencing tensile strains. Truss finite elements are used to model the reinforcing layer. An elasto-plastic with hardening constitutive law (see Figure 3.5) is chosen; thickness and equivalent mechanical parameters of the reinforcing layer are assumed as indicated in Table 3.4.

Mechanical FRCM parameters

Thickness [mm]	E_r [MPa]	σ_{or} [MPa]	H_r [MPa]
8.038	9856	0.8	43

Table 3.4: Mechanical parameters for the reinforcing layer of the masonry wall reinforced with FRCM.

In Figure 3.8 (a) and (b) a detail of FE discretization used for brick and mortar, for unreinforced and reinforced models is shown, respectively. In particular, the color blue indicates the brick material, whereas the other colors describe the

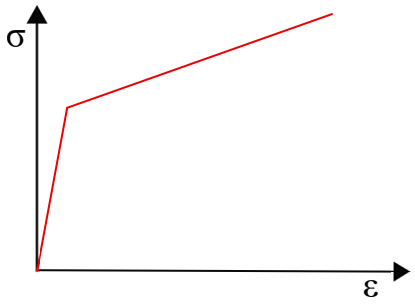

Figure 3.5: Elasto-plastic with hardening constitutive law for FRCM.

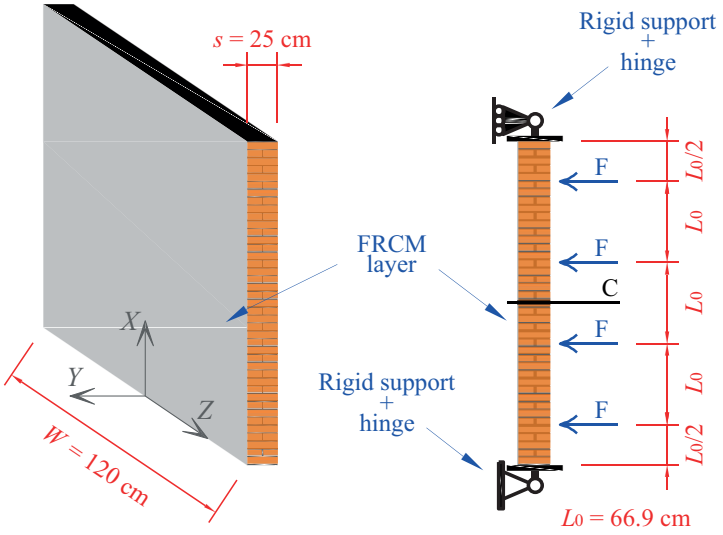

Figure 3.6: Geometry of the masonry wall reinforced with FRCM composite materials (Addessi et al., 2018).

mortar. The red lines represent the schematic boundary condition. In Figure 3.8 (b) the FRCM is represented by the green line.

Figure 3.7 shows the global response curve (red line) obtained with the proposed micromechanical model in terms of one applied transverse force versus mid-height deflection and compares it with that resulting from the multiscale approach (dashed line) proposed in Addessi et al. (2018) and with the experimental outcomes in Bellini et al. (2017) (blue line). The numerical micromechanical responses show a good agreement with the multiscale model and experimental outcomes for

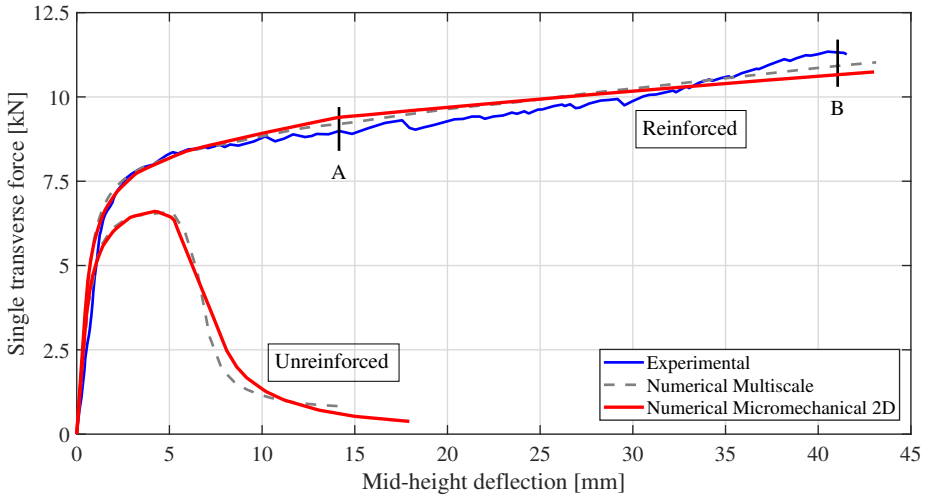

Figure 3.7: Global response curves for masonry wall reinforced with FRCM (adapted from Addessi et al. (2018)).

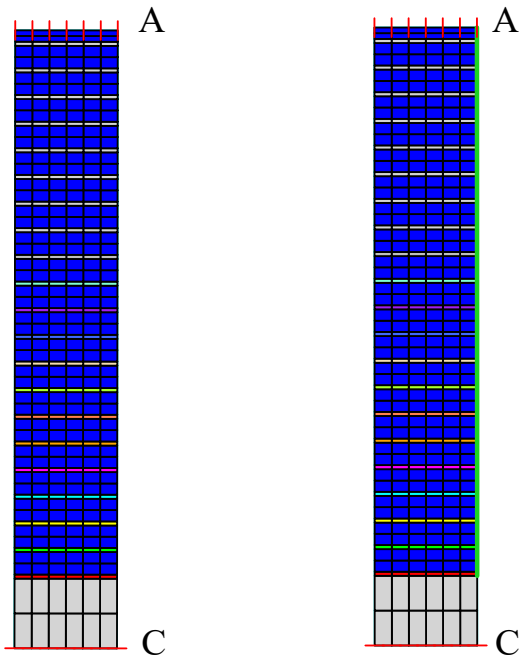

Figure 3.8: FE brick and mortar discretization for (a) unreinforced and (b) reinforced numerical model of the masonry walls (Bellini et al., 2018).

the reinforced wall. As addressed in Addessi et al. (2018), the FRCM composite layer installation increases wall resisting capacity, as correctly detected by the numerical model. For F $>$ 5 kN, the reinforcement prevents wall collapse, which occurs for a higher value of the applied load due to reinforcement failure. The mortar layer attached to the reinforcement starts cracking due to increasing load when wall deflection increases. Positions of the cracks initially correspond to the mortar joints at the mid-height zone, where tensile strains appear higher. Then, cracks propagate along the wall height. Therefore, the tensile stresses in the glass fiber grid progressively grow until its failure produces the wall collapse. Comparison the numerical simulation of the unreinforced wall obtained with the micromechanical and the multiscale model is also illustrated, showing a very good match.

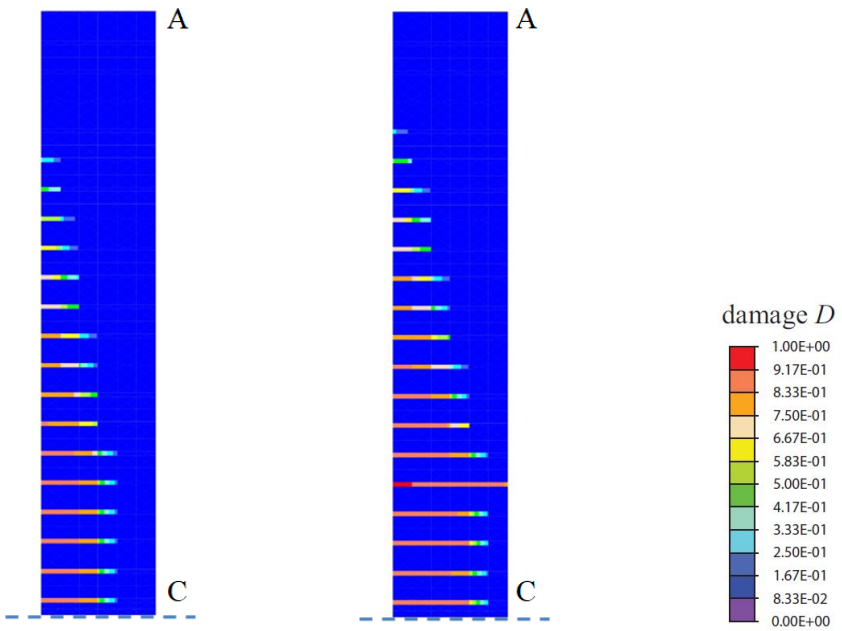

Figure 3.9: Distribution of the damage variable D with the proposed micromechanical model in the unreinforced wall (a) Mid - height deflection = 5 mm, (b) Mid - height deflection = 15 mm (c) damage color bar.

Figure 3.9 (a) and (b) shows the the distribution of the damage variable D

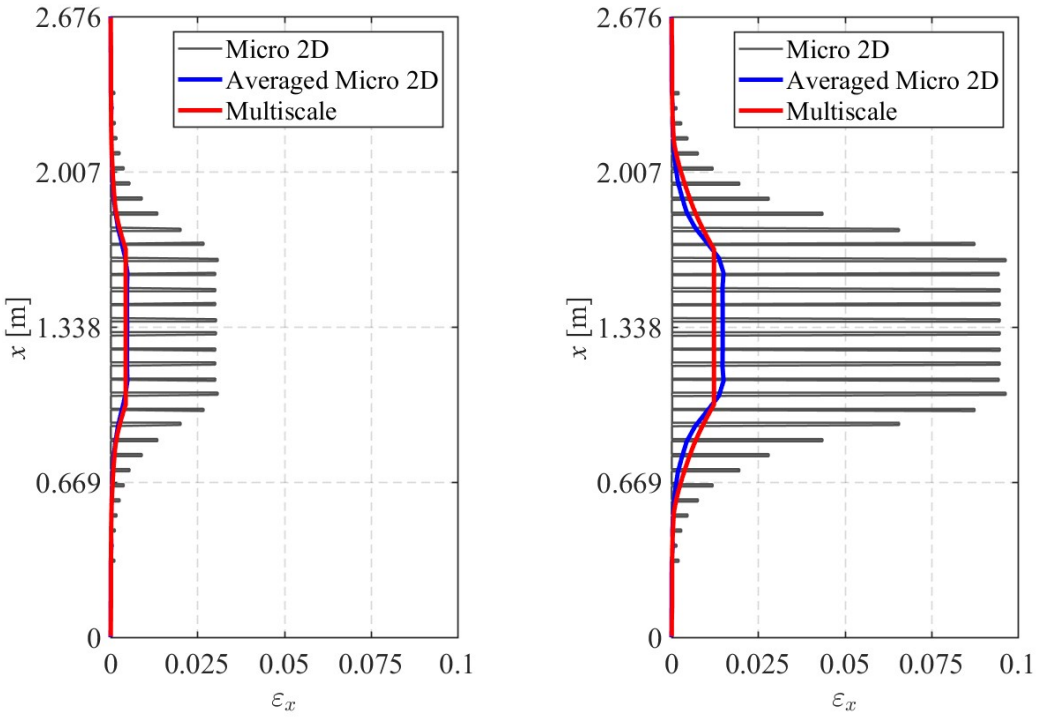

(a) Stage A

(b) Stage B

Figure 3.10: From (Addessi et al., 2018): masonry wall reinforced with FRCM composite materials: comparison of the vertical strains obtained with the micromechanical and multiscale models.

defined in Eq.(3.11) for the unreinforced wall, considering two different mid-height deflection values. The color bar (Figure 3.9 (c)) clearly indicates that damage can vary between 0 and 1, corresponding to the virgin and fully degraded material state. Lastly, in Figure 3.10, the estimated vertical strain distribution in the reinforcing layer for the micromechanical and multiscale models are plotted for stage A and B, i.e. the two loading steps indicated by the black line in Figure 3.7. The micromechanical model (gray lines) shows the real concentrations of the strains which localize in correspondence to the mortar joints. This strain localization first affects only a portion of the wall at mid-height (stage A) and then gradually extends along the entire wall (stage B).

The second considered application is from the experimental campaign conducted by Van der Pluijm (1999). A four-point out-of-plane bending response

of a masonry wall is studied and numerically modeled. Figure 3.11 shows the specimen geometry and boundary conditions. The top and bottom of the wall are supported at the middle of the outermost brick alignments, and two forces, distributed along the width, act orthogonally to the specimen plane. Tables 3.5 and 3.6 contain the adopted mechanical parameters for mortar and brick, deduced from the experimental measurements reported in Van der Pluijm (1999). The mortar nonlocal radius, l_c, is set equal to the joint thickness 13 mm, assumed as mortar characteristic length. Accounting for the specimen's symmetry, the micromechanical numerical model considers only one-half of the wall.

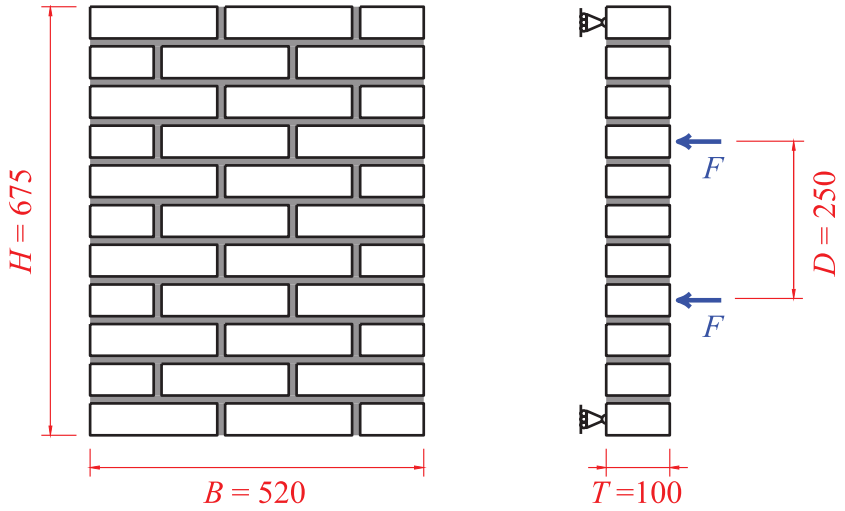

Figure 3.11: Four-point out-of-plane bending test of the masonry wall: specimen geometry (Van der Pluijm, 1999).

Mortar

E^m [MPa]	ν^m [MPa]	$\sigma_{N,0}$ [MPa]	$\tau_{NT,0}$ [MPa]	g_{cI} [MPa]	g_{cII} [MPa]	μ
5000	0.8	0.4	1.9	1.8×10^{-4}	1.5×10^{-4}	0.82

Table 3.5: Four-point out-of-plane bending test of the masonry wall: material parameters for mortar.

Bricks	
E^b [MPa]	ν^b [MPa]
16700	0.13

Table 3.6: Four-point out-of-plane bending test of the masonry wall: material parameters for bricks.

The structure is modeled in the flexure plane and discretized the bed mortar joints and the bricks with quadrilateral FEs having a uniform thickness. In Figure 3.12 a detail of FE discretization used for brick and mortar for the model is shown. In particular, the color blue indicates the brick material, whereas the green color describe the mortar. The red lines represent the schematic boundary condition.

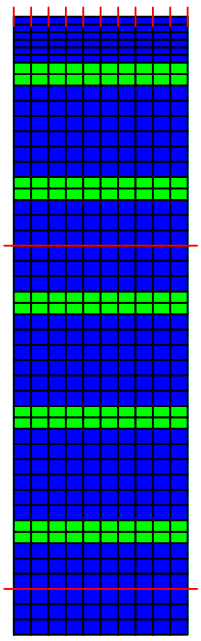

Figure 3.12: FE brick and mortar discretization for the numerical model of the masonry wall (Van der Pluijm, 1999).

The cross-section curvature K is estimated as the average value occurring in the central region where the moment is constant, following the proposal in Serpieri et al. (2017). The nonlinear response of the wall in terms of maximum bending moment m per unit width versus the corresponding cross-section curvature K is plotted in Figure 3.13. The numerical results for the proposed micromechanical

model (red line) are compared with the multiscale model (dashed line) and the experimental ones (blue line). The shaded area corresponds to the experimental confidence region. The upper and lower bound linear-parabola curves have been estimated by adopting the upper and lower confidence intervals for the parameters, also considered in Serpieri et al. (2017). The numerical curves are contained in the confidence area and satisfactorily describe the initial stiffness, the peak strength, and the collapse mechanisms of the wall. The difference between the numerical and the experimental curves mostly depends on the calibration of the material parameters, whose experimental measurements are considerably uncertain.

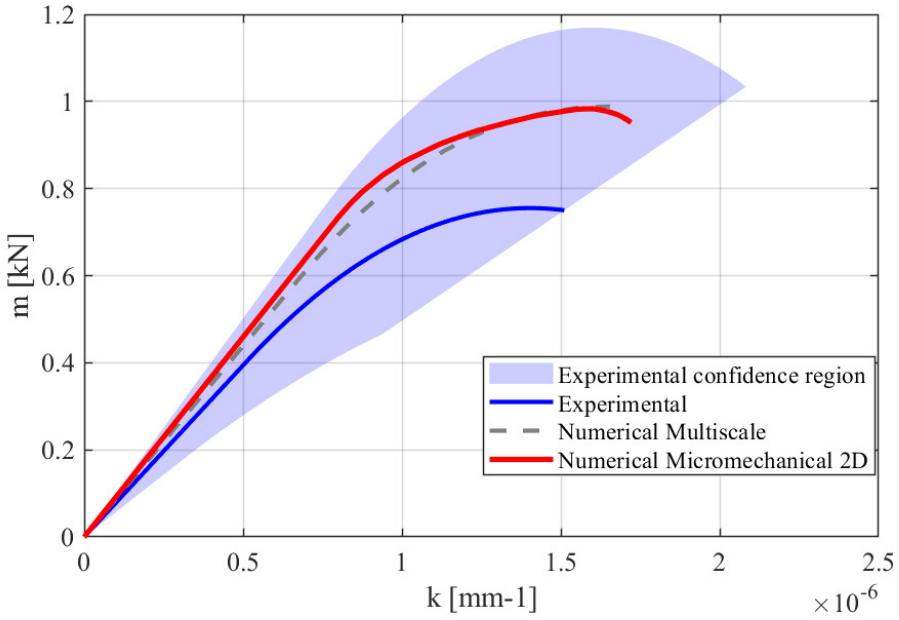

Figure 3.13: Adapted from Addessi et al. (2017), four-point out-of-plane bending test of the masonry wall: maximum moment m per unit width versus curvature K.

3.3 Response of unreinforced masonry arches

Subsequently, the static response of masonry arches to vertical eccentric loads is investigated in terms of global force-displacement curves and failure mechanisms.

First, the numerically obtained results are validated by comparison with experimental outcomes, referring to an experimental campaign carried out at University of Minho (Oliveira et al., 2010). Then, parametric numerical studies are performed to investigate the influence of geometry and material mechanical parameters on masonry arches nonlinear structural response.

3.3.1 Experimental-numerical comparison

The experimental campaign conducted by Oliveira et al. (2010) and finalized to evaluate the efficiency of strengthening solutions on the behavior of masonry arches is here considered, aiming at validating the accuracy and efficiency properties of the described micromechanical numerical procedure. Half-scaled unreinforced and strengthened specimens were tested under displacement control up to failure. The arches were built up with $100 \times 50 \times 25\,\text{mm}^3$ solid clay bricks and lime-based mortar with a constant intrados thickness of approximately 10 mm. The resulting geometry is shown in Figure 3.14 (b), being characterized by internal span of 1467 mm, internal radius $R = 750$ mm and arch thickness $t = 50$ mm. The out-of-plane width of the arch is equal to 450 mm. As for the loading conditions, a monotonically increasing vertical displacement s was applied at the nineteenth brick counted from the left arch impost, that is at about a quarter of the span.

Herein, the attention is focused on the two reference arches, called $US1$ and $US2$, tested with no strengthening. These exhibited a similar behavior in terms of failure mode with the formation of the typical four hinge mechanisms. However, some differences emerged between their global vertical load (F)-vertical displacement (s) curves, as evident from the blue dashed lines in Figure 3.15. These discrepancies, both appearing in the pre-peak stiffness and maximum load, were probably caused by variation of the mortar tensile strength.

The experimental response of these arches is here numerically reproduced, discretizing each brick and mortar joint with 5×3 and 5×1 FEs, respectively. The assumed material parameters are contained in Table 3.7, where E^i and G^i ($i = b, m$) denote the Young's and shear modulus, respectively. These are deduced by the experimental data reported in Oliveira et al. (2010) and the numerical simulation performed by Di Re et al. (2018). For both materials, the unit weight

(a)

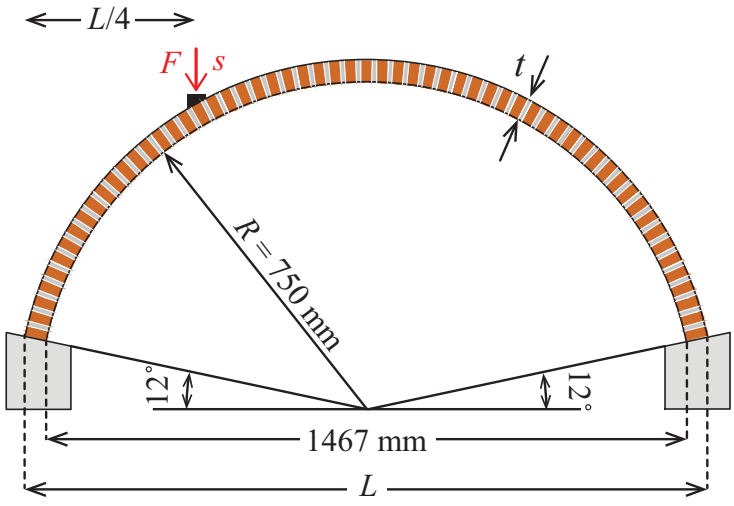

(b)

Figure 3.14: Circular arch tested by Oliveira et al. (2010): (a) Construction of the arch and (b) geometry and loading condition.

$\gamma = 17\,\mathrm{kN/m^3}$ is assumed.

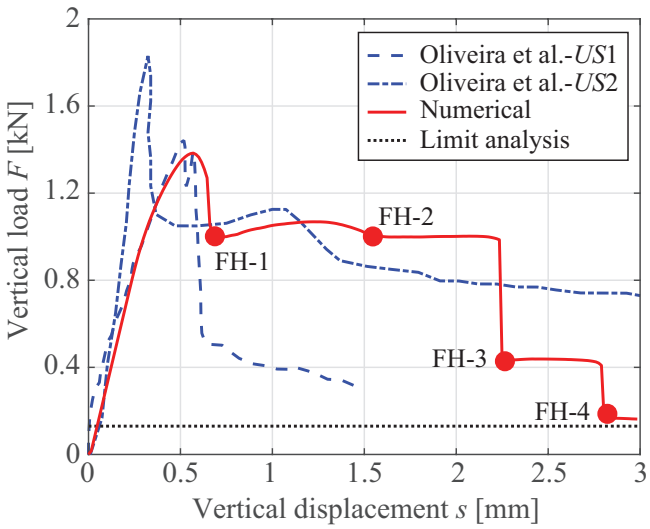

Figure 3.15: Comparison between numerical and experimental force-displacement response curves.

Elastic material parameters				
E^b [MPa]	G^b [MPa]	E^m [MPa]	G^m [MPa]	μ
5000	2083.3	1200	500	0.5774

Table 3.7: Elastic material parameters adopted for bricks and mortar.

Damage material parameters			
$\sigma_{N,0}$ [MPa]	$\tau_{NT,0}$ [MPa]	g_{cI} [MPa]	g_{cII} [MPa]
0.25	0.25	1.8×10^{-3}	1.25×10^{-3}

Table 3.8: Damage material parameters adopted for mortar.

The mortar nonlocal radius, l_c is set equal to the joint thickness 10 mm, assumed as mortar characteristic length.

Figure 3.15 compares the numerically obtained global curve, depicted with solid red line, with the experimental outcomes. It emerges a satisfactory agreement, as the peak load predicted by the numerical simulation is close to that experimentally evaluated for the $US1$ arch. On the numerical curve, circle red markers indicate points at which significant cracked sections arise, showing that the steep drops of the strength correspond to the onset of the flexural hinges. Indeed, according

to the experimental test, the failure mechanism involves the formation of hinges located, alternately, at the arch intrados and extrados. This is shown in detail in Figure 3.16, which compares the failure mechanism experimentally detected (Fig. 3.16 (a)) with the distribution of the damage variable D defined in Eq.(3.11) at the end of the numerical analysis, on the arch final deformed configuration (Fig. 3.16(b)). The color bar at the right of Figure 3.16 (b) clearly indicates that damage can vary between 0 and 1, corresponding to the virgin and fully degraded material state. Moreover, Figure 3.16 (b) shows the location of the four hinges, numbered according to the formation sequence (see Fig. 3.15), and a detail of the FE discretization used for brick and mortar.

Finally, it should be remarked that both numerical and experimental response curves in Figure 3.15 predict a peak load much higher than the collapse load evaluated by the classical limit analysis (indicated in Figure 3.15 with dashed black line). This interesting aspect will be investigated deeper in Section 3.3.3. However, this is caused by the not negligible tensile strength of the mortar, which moves away from the first hypothesis of the standard limit analysis. Anyway, when the failure mechanism is completed, that is, when all the four hinges are formed, the residual load approaches to the limit analysis collapse load.

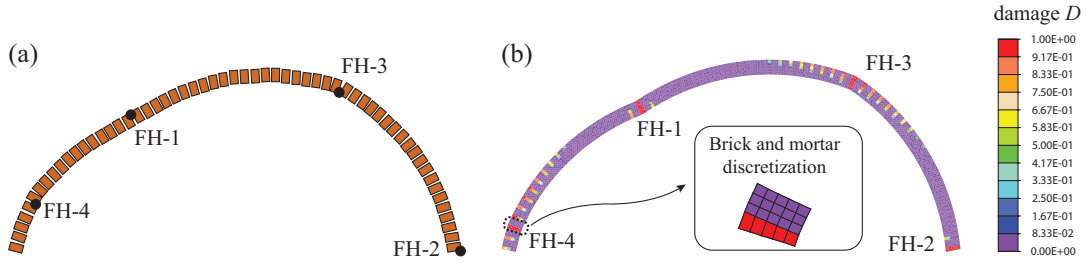

Figure 3.16: Circular arch tested by Oliveira et al. (2010): (a) experimental and (b) numerical failure mechanisms (FH = 'flexural hinge').

3.3.2 Effect of geometry

Starting from the results presented in the previous section, the arch geometry influence is investigated in the following. In particular, the thickness/internal radius ratio is varied, by considering four values of t/R ratio, that is 0.13, 0.20, 0.27

and 0.33. The analyses are performed assuming the same internal span (1467 mm) and internal radius (750 mm), thus only varying the thickness t and, consequently, the external radius. Moreover, the vertical displacement is always applied at the nineteenth brick counted from the left impost, mimicking the loading conditions in Figure 3.14 (b). The adopted material parameters are those contained in Table 3.7 and Table 3.8.

Figure 3.17(a) shows the vertical force (F)-vertical displacement (s) curves for all the analyzed cases, including the ratio $t/R = 0.07$ corresponding to that studied in Section 3.3.1. Different pre-peak stiffness emerge as a consequence of the increased thickness value, as well as different post-peak behavior. In particular, steeper softening branches occur with increasing ratio t/R. This is due to the variation of the collapse mechanism, which moves from four flexural hinges to a mixed mode involving both flexural and shear hinges, as schematically depicted in Figure 3.17 (b).

The final damage distributions in the arches deformed configuration are reported in Figure 3.18 (a-d), pointing out that the thicker arches, corresponding to $t/R = 0.27$ and $t/R = 0.33$, present voussoirs sliding near the load application point and at the right impost, together with a flexural hinge near the left impost. However, the structural responses are quite complex, as they show variation of the type of hinges during the loading history. Let us focus on the degrading process of the arch with $t/R = 0.33$, chosen as example. Before reaching the peak load, flexural hinges arise, placed near to the load application point and at the right impost, as clearly shown in Figure 3.19 (a) by the damage distribution evaluated at point A (corresponding to $s = 0.5$ mm) in Figure 3.17 (a). Then, a significant drop of the strength appears in the load-displacement response curve (see the black curve in Fig. 3.17 (a)), caused by the voussoirs sliding at the load application point and the formation of the flexural hinge near to the left impost. This modification of the collapse mode is evident from the damage map in Figure 3.19 (b), which refers to point B ($s = 0.7$ mm) in Figure 3.17 (a). The further increase of the applied displacement does not cause significant variation of the damage distribution and, consequently, a slight increase of the strength emerges in the load-displacement response curve characterized by the stiffness of the damaged arch. Finally, at the end of the loading history, another abrupt strength decay appears (point C in the

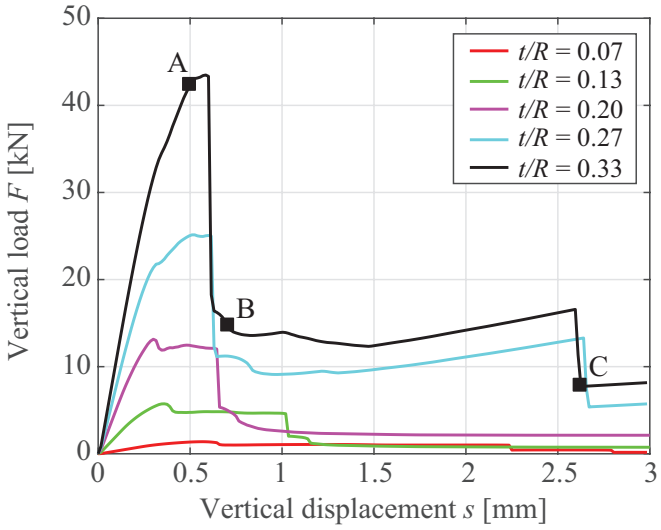

(a)

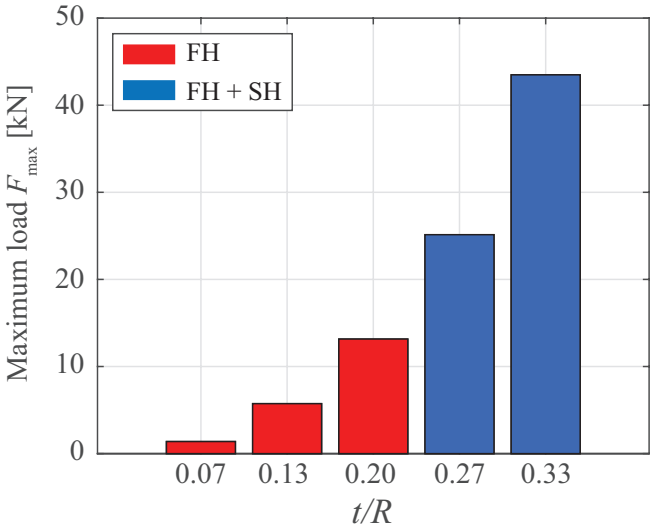

(b)

Figure 3.17: Effect of the t/R ratio: (a) load-displacement curves, (b) maximum load and failure mechanism (FH = 'flexural hinge', SH = 'shear hinge').

global response curve in Figure 3.17 (a)). Thi is due to the modification of the hinge at right impost, which changes from flexural to shear type leading to the final damage distribution depicted in Figure 3.18 (d).

To conclude, according to results presented in Misseri et al. (2018); Nodargi

et al. (2020), it clearly emerges the strong influence of the arch geometric properties on the failure mechanism formation and progression, moving from the classical flexural hinge mechanism to more complex mixed modes, also involving the formation of shear slidings.

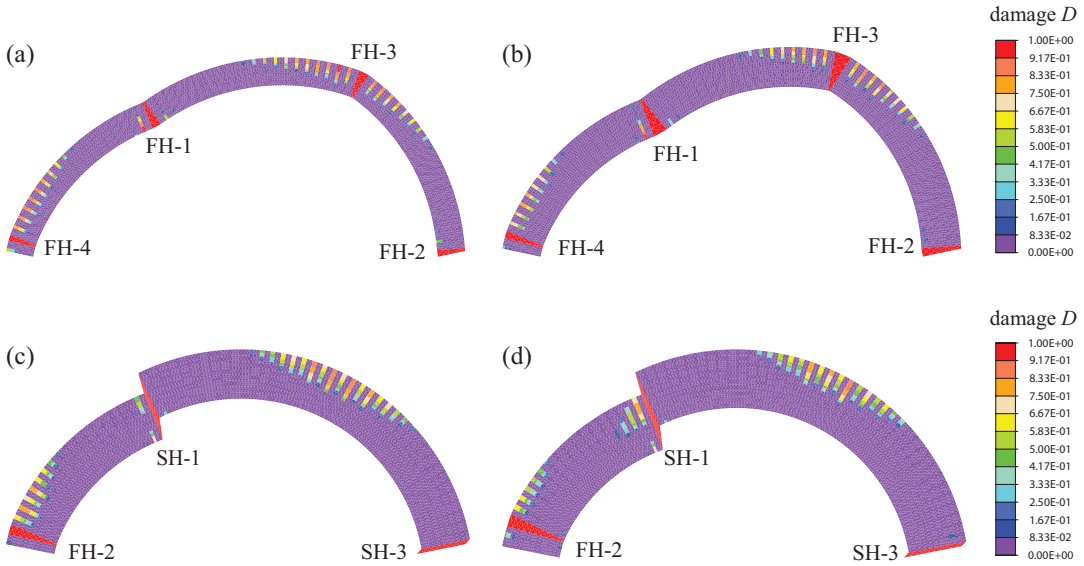

Figure 3.18: Distribution of the damage variable D for different values of t/R at the end of the analyses: (a) $t/R = 0.13$, (b) $t/R = 0.20$, (c) $t/R = 0.27$ and (d) $t/R = 0.33$. (FH = 'flexural hinge', SH = 'shear hinge').

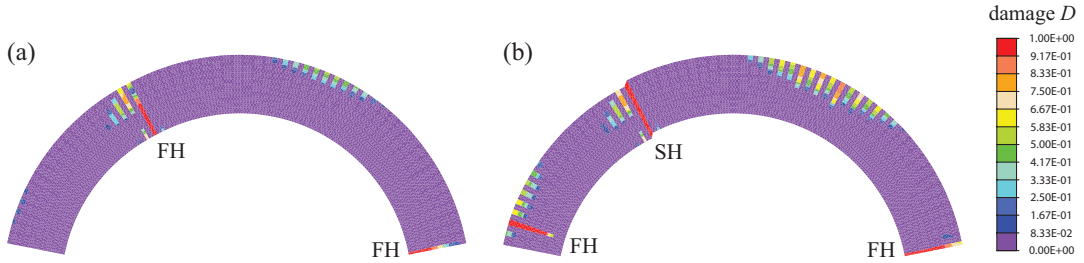

Figure 3.19: Distribution of the damage variable D for arch with with $t/R = 0.33$ at different values of the applied displacement s: (a) $s = 0.5\,\text{mm}$ and (b) $s = 0.7\,\text{mm}$. (FH = 'flexural hinge', SH = 'shear hinge')

3.3.3 Effect of material parameters

Some parametric analyses are here performed to investigate the influence of some relevant material parameters. Geometry ($t = 50\,\text{mm}$) and loading conditions adopted by Oliveira et al. (2010) are considered. Three sets of analyses are carried out: the first studies the effect of the material tensile strength $\sigma_{N,0}$, the second investigates the influence of the mode I fracture energy g_{cI} and the last analyzes the arch response as the friction coefficient μ varies.

Four values of the mortar tensile strength are considered, that is $\sigma_{N,0,r}/2$, $\sigma_{N,0,r}/4$, $\sigma_{N,0,r}/8$ and $\sigma_{N,0,r}/40$, being $\sigma_{N,0,r}$ the reference value contained in Table 3.7 and Table 3.8. The resulting response curves are plotted in Figure 3.20, together with the value of the collapse load resulting from the limit analysis approach. The curves are characterized, as expected, by a decreasing maximum value of the peak load $F_{\max}$, as the material tensile strength decreases. It is worth noting that the peak load approaches to the limit analysis collapse value when the tensile strength vanishes, according to the hypothesis of this last approach, considering zero tensile strength for masonry. Moreover, it appears that the load-displacement curve can approach to the limit value either from the top or the bottom (Lourenço, 2001; Cancelliere et al., 2010), depending on the material tensile strength characteristic. Thus, the shape of the global response curve is strongly influenced by the tensile constitutive response of the mortar, not only on the peak load value, but also on the post-peak behavior showing a more severe softening branch as the tensile strength grows.

As for the effect of the mode I fracture energy g_{cI}, three values are selected: $g_{cI,r}/4$, $g_{cI,r}/2$ and $g_{cI,r} \times 2$, with $g_{cI,r}$ the reference energy reported in Table 3.8. By observing the results shown in Figure 3.21 in terms of load-displacement curves, again it emerges that the peak load and the slope of the softening branch are strongly affected by the variation of g_{cI}. The green and violet curves, which refer to the lowest values of g_{cI}, show steep drops of the strength, whereas the light blue curve, which refers to the highest value of g_{cI}, presents a less severe softening branch. This is due to the different occurred collapse mechanism. Although, for all the analyzed cases, flexural failure modes are detected (see Figure 3.22 (a-c)), localized damaged zones appear for the lower values of g_{cI} (Figure 3.22 (a,b)).

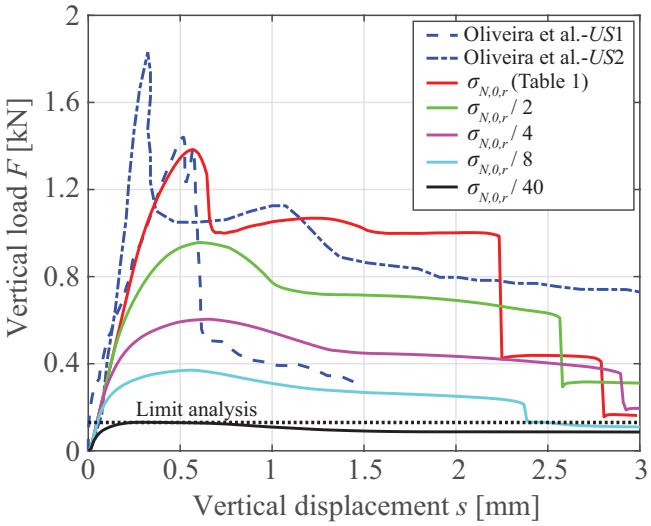

Figure 3.20: Material parameters effect: influence of the tensile strength.

Conversely, for the highest adopted value of the fracture energy, damage spreads around the regions where significant tensile strains occur (Figure 3.22 (b)). It is also interesting to note that the location of the hinges is modified by varying the fracture energy.

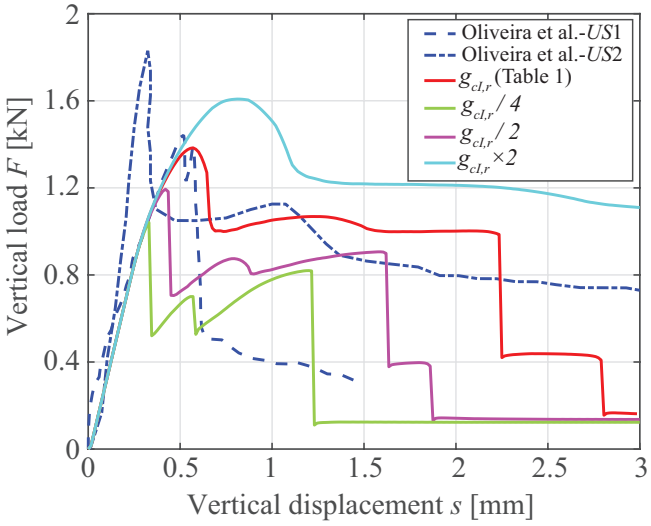

Figure 3.21: Material parameters effect: influence of mode I fracture energy.

.

Finally, the structural response is investigated considering different friction

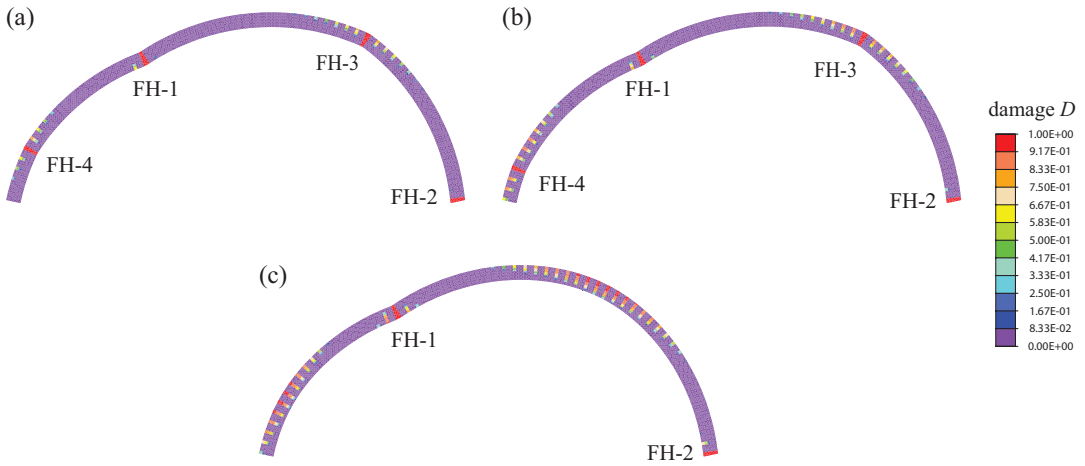

Figure 3.22: Distribution of the damage variable D at the end of the analyses for $t/R = 0.07$ and different values of g_{cI}: (a) $g_{cI} = g_{cI,r}/4$, (b) $g_{cI} = g_{cI,r}/2$ and (c) $g_{cI} = g_{cI,r} \times 2$.

coefficient values, chosen within a realistic range for masonry material. In detail, behavior of arches characterized by ratio $t/R = 0.27$ and $t/R = 0.33$, whose collapse mode involved shear sliding in case of $\mu = 0.5774$ (see Figure 3.18 (c,d)), is studied assuming $\mu = 0.5, 0.65, 0.7$. The other material parameters refer to those contained in Table 3.7 and Table 3.8. For the lowest value of μ, both arches show voussoirs sliding (Figure 3.23 (a,b)), similarly to the reference case of $\mu = 0.5774$. On the contrary, when the friction coefficient increases, the interlocking effect's increment can prevent the shear sliding mechanism and let flexural mode prevail. This phenomenon already appears in case of $\mu = 0.65$ for the thinner arch ($t/R = 0.27$) and it is obviously confirmed when $\mu = 0.7$ (Figure 3.23 (c,e). Instead, the failure mechanism of the thicker arch still involves voussoirs sliding in case of $\mu = 0.65$, testifying that effect of geometry prevails over that of friction (Figure 3.23 (d)). Then, setting $\mu = 0.7$, the flexural mechanism emerges, as evident from Figure 3.23 (f). To summarize, it appears that the friction coefficient value can strongly affect the overall arch response, as this can move the collapse mechanism from shear sliding to the classical four flexural hinges formation and vice-versa.

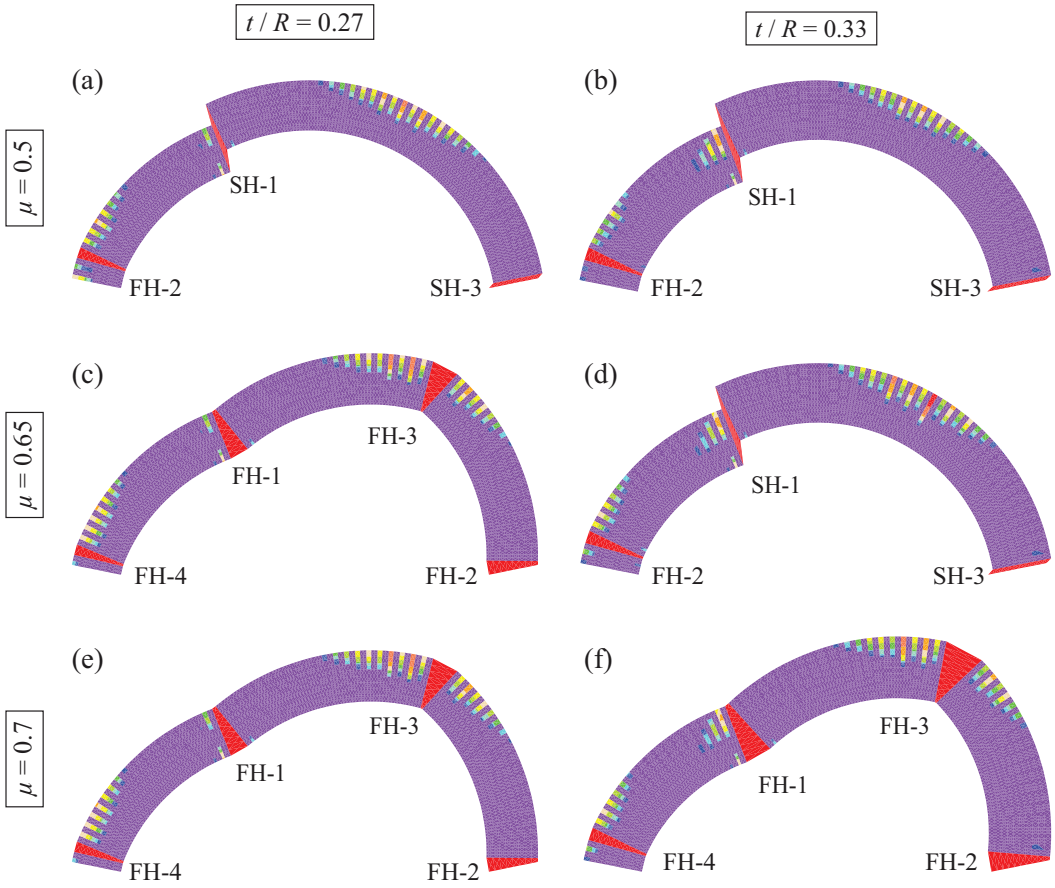

Figure 3.23: Distribution of the damage variable D at the end of the analyses for $t/R = 0.27$ (a,c,e) and $t/R = 0.33$ (b,d,f) and different values of μ: (a,b) $\mu = 0.5$, (c,d) $\mu = 0.65$ and (e,f) $\mu = 0.7$.

3.4 Summary

In this chapter a damage-plastic model for the micromechanical analysis of 2D masonry structures was described. First, the existing constitutive law was illustrated, and the main aspects related to the finite element implementation were presented. The numerical procedure has been properly formulated to study masonry structural elements characterized by general geometry and arrangement. To overcome mesh-dependency drawback, occurring in cases of strain-softening behavior, a nonlocal integral approach has been introduced in the FE procedure, thus overcoming localization problems. To validate the new element, a comparison

between numerical and experimental outcomes were performed for masonry walls. Two experimental campaigns (Bellini et al., 2017) and Van der Pluijm (1999) were reproduced. The results gave a very good agreement with the experimental and multiscale outcomes obtained with the model in Addessi et al. (2020a), formulated using the same constitutive law.

Then, the structural response of unreinforced masonry arches has been numerically analyzed. First, model efficiency and accuracy has been tested by reproducing the outcomes of experimentally tested arches (Oliveira et al., 2010). The resulting load-displacement response curve and failure mechanism showed a very good agreement with the experimental evidence. Subsequently, parametric analyses have been performed to investigate the effects of some relevant geometric and mechanical parameters. As concerns the influence of geometry, numerical tests have been carried out by varying the thickness/internal radius ratio from 0.07 to 0.33. It emerged that, as the ratio t/R increases, failure mechanism moves from four flexural hinges to a mixed mode involving both flexural and shear hinges, leading to a more brittle behavior. Indeed, literature studies (Di Carlo et al., 2018) confirm that arch geometric parameters permit to identify the possible failure mechanisms under seismic load conditions. Regarding the mechanical parameter effects, a strong influence of the mortar tensile strength and the mode I fracture energy has appeared on the trend of the global response, mainly affecting the collapse load value and the brittleness of the post-peak response. The adopted procedure has proved to reproduce the results coming from the limit analysis approach, when the assumptions of this last are approached. Moreover, it emerged that the arch collapse mechanism depends on the assumed friction coefficient value: for fixed geometry, the failure mode involving shear sliding changes into the flexural hinge mechanism, as friction increases. However, the limit value that determines the variation of the failure mode is a peculiar characteristic of each arch, being influenced by the coupled effect of geometry and friction.

Chapter 4

Macromechanical finite element modeling of masonry structures

This section explores the use of macromechanical approaches based on smeared crack models, implemented in DIANA (2019), for the monotonic and cyclic in-plane analysis of masonry panels. The numerical investigation is focused on two material macromechanical models, known as total strain cracking and crack and plasticity models. These showed some limitations when analyzing the behavior of masonry structures subjected to in-plane cyclic loading. A modified version of the Drucker-Prager model including cohesive softening is introduced in the crack and plasticity model to overcome these shortcomings. A suite of numerical simulations is performed referring to an experimental campaign on two masonry (squat and slender) panels (Anthoine et al., 1995). A comparison of distinctive features of flexural and shear response of these structural elements is addressed. The results derived from the two FE macro-models are compared with the experimental outcomes, highlighting the effects of geometry, stiffness degradation, and post-peak energy dissipation. Furthermore, a comparison with the damage-plastic macromechanical model proposed in Gatta et al. (2018) is performed.

4.1 Smeared crack constitutive models

The simplicity of the smeared crack approach captured the attention of the scientific community, and most of the FE codes have adopted this approach. In such a context, as earlier mentioned, this study investigates the use of macromechanical constitutive models to analyze the nonlinear degrading response of masonry structures.

The study focuses on two material constitutive laws belonging to the class of the so-called smeared crack models (Rots, 1988; De Borst and Nauta, 1985), known as total strain cracking and crack and plasticity, which will be described below.

4.1.1 Total strain cracking model

The Total Strain Rotating Crack (TSRC) model is used in this study. This computes the stress as a function of the strain and follows a smeared approach to describe the fracture process. According to the rotating concept, the crack directions are updated to rotate with the principal directions and to be aligned with them during loading history. The constitutive model based on total strain is developed along the lines of the modified compression field theory, originally proposed by Vecchio and Collins (1986). The three-dimensional extension of this theory was proposed by Selby (1995), whose theoretical description was the basis of the implementation in Diana. The basic concept of the TSRC model is that the stress vector is evaluated referring to the intrinsic reference system of the crack. As described in Feenstra (1993), agreeing to the definition of total formulation, the constitutive model is developed in terms of strains. Here, a two dimensional formulation is considered. As described in Section 2.3.2, an additive decomposition of the incremental total strain vector is assumed into an elastic, reversible, part $\Delta\boldsymbol{\varepsilon}^e$ and an inelastic, irreversible, part $\Delta\boldsymbol{\varepsilon}^c$. Thus, the incremental strain vector is given by:

$$\Delta\boldsymbol{\varepsilon} = \Delta\boldsymbol{\varepsilon}^e + \Delta\boldsymbol{\varepsilon}^c \tag{4.1}$$

The corresponding incremental stress vector is expressed as:

$$\Delta\boldsymbol{\sigma} = \mathbf{D}^e \Delta\boldsymbol{\varepsilon}^e \tag{4.2}$$

with $\mathbf{D}^e$ the linear-elastic stiffness matrix.

The co-rotational formulation is generally correlated to the elasticity-based total strain crack model (Rots, 1988; Willam et al., 1989). In this model, the co-rotational formulation is applied to assume that the local constitutive model, which describes the relation between the local stress and strain vectors, is converted into the global coordinate system with the transformation matrix defined by the principal directions of the strain vector.

The incremental strain vector in the global coordinate system is expressed as $\Delta\boldsymbol{\varepsilon}$, which is transformed into the incremental strain vector in the intrinsic coordinate $\Delta\boldsymbol{\varepsilon}_l$, where l indicates the local system (n, t) following the crack directions, with the strain transformation matrix $\mathbf{N}$:

$$\Delta\boldsymbol{\varepsilon}_l = \mathbf{N}\Delta\boldsymbol{\varepsilon} \tag{4.3}$$

In a co-axial rotating concept the strain transformation matrix $\mathbf{N}$ depends on the current strain vector, whereas in a fixed concept, the strain transformation matrix is fixed upon cracking. The strain transformation matrix $\mathbf{N}$ results:

$$\mathbf{N} = \begin{bmatrix} c_{xn}^2 & c_{yn}^2 & c_{xn}c_{yn} \\ c_{xt}^2 & c_{yt}^2 & c_{xt}c_{yt} \\ 2c_{xn}c_{xt} & 2c_{yn}c_{yt} & c_{xn}c_{yt} + c_{yn}c_{xt} \end{bmatrix} \tag{4.4}$$

with c_{xn} the cosine between the i and j axis. The constitutive model has to be formulated in the local coordinate system in the form:

$$\Delta\boldsymbol{\sigma}_l = \mathbf{D}(\boldsymbol{\varepsilon}_l)\Delta\boldsymbol{\varepsilon}_l \tag{4.5}$$

with $\mathbf{D}(\boldsymbol{\varepsilon}_l)$ the tangent stiffness matrix. The updated incremental stress vector in the global coordinate system is finally given by:

$$\Delta\boldsymbol{\sigma} = \mathbf{N}^T \Delta\boldsymbol{\sigma}_l \ . \tag{4.6}$$

The constitutive model before cracking is usually assumed to be governed by a

linear-elastic model. After crack initiation the Poisson effect is generally neglected and the Poisson ratio is set equal to zero. The post-crack behavior is then described by an orthotropic, uncoupled, stiffness matrix, i.e.

$$\begin{bmatrix} \Delta\sigma_{nn} \\ \Delta\sigma_{tt} \\ \Delta\tau_{nt} \end{bmatrix} = \begin{bmatrix} E_n & 0 & 0 \\ 0 & E_t & 0 \\ 0 & 0 & \beta G \end{bmatrix} = \begin{bmatrix} \Delta\varepsilon_{nn} \\ \Delta\varepsilon_{tt} \\ \Delta\gamma_{nt} \end{bmatrix} \tag{4.7}$$

The smeared fracture process is activated when the maximum principal stress at the material point exceeds the tensile strength (see Figure 4.1).

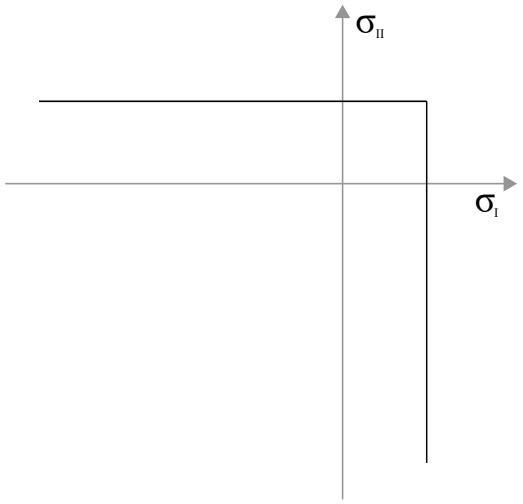

Figure 4.1: Failure surface in principal stress space.

During loading, the masonry is subjected to tensile and compressive stresses, resulting in cracking and crushing of the material. Different tensile and compressive functions, based on fracture energy, can be adopted (DIANA, 2019). The shape of softening branch in the stress-strain law controls the cracking phenomenon, being governed by the fracture energy parameter of the material given by the area under the stress-strain diagram. Two values are introduced for the fracture energy parameters, i.e. G_t and G_c that are associated, respectively, with the tensile and compression behavior. In this study, an exponential law governs the softening branch in tension and a hardening-softening parabolic law the post-peak response in compression. Herein, fracture energy values are estimated following the indications in Lourenço (2010).

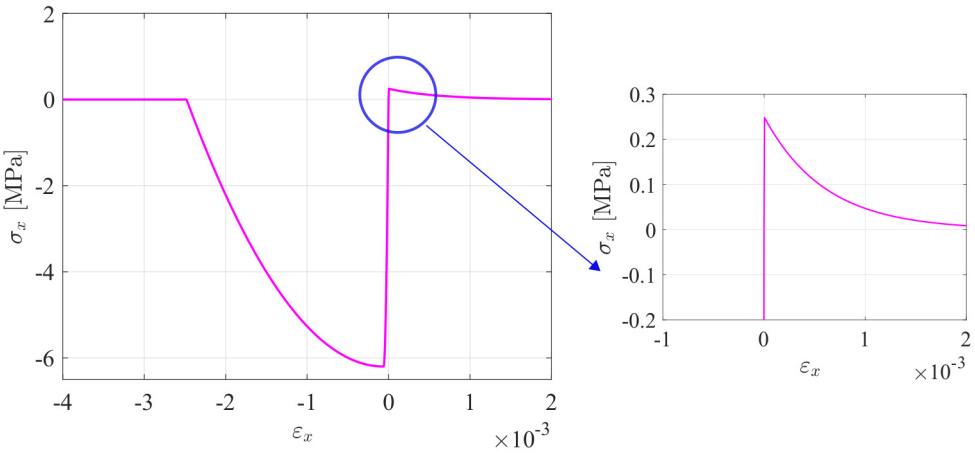

Figure 4.2: Masonry stress-strain law: tensile and compressive law for TSRC model.

The modeling of the shear behavior is also introduced in the fixed crack and combined rotating to fixed crack where the shear stiffness is usually reduced after cracking. A possible formulation (DIANA, 2019) is based on the definition of a constant shear stiffness reduction, i.e.,

$$G^{cr} = \beta G \tag{4.8}$$

with β the shear retention factor, $0 \leq \beta \leq 1$. For the rotating crack model the shear retention factor can be assumed equal to one.

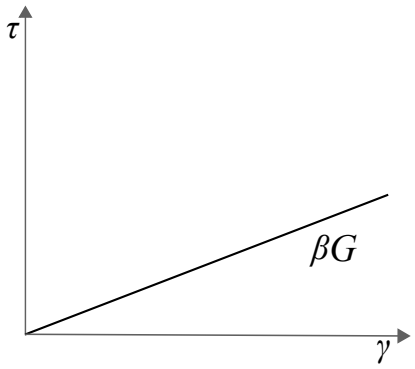

Figure 4.3: Constant shear retention for TSRC model.

In an incremental-iterative solution scheme, the equilibrium between the inter-

nal force vector and the external load vector is achieved with a Newton-Raphson iterative procedure. For this purpose, the constitutive model should also define the stiffness matrix, which is utilized to reach equilibrium. In Diana, two approaches to the stiffness matrix are used: the secant and the tangent stiffness matrix. The first approach has proved to be robust and stable in structures with extensive cracking. The latter has shown superiority in the analysis, where localized cracking and crack propagation are the most important phenomena.

4.1.2 Crack and plasticity model

The Crack and Plasticity (CP) model is based on the smeared crack approach used to simulate the tensile cracking behavior, whereas the Drucker-Prager plasticity model is adopted to simulate the compressive response. The CP model can be categorized as a multi-directional fixed smeared crack model with an elastic-plastic constitutive law in compression. According to the multi-directional fixed crack formulation, and differently from the fixed smeared crack model where only one fixed crack can form at each point, more than one crack is allowed to form.

A brief description of the constitutive law is given starting from the multi-directional fixed crack model that rules the tensile behavior. The first model was probably proposed by Litton (1974), even since many other researchers, for instance, De Borst and Nauta (1985) and Rots (1988) started to use it.

Here, an additive decomposition of the incremental total strain vector is assumed into an elastic, reversible, part $\Delta\boldsymbol{\varepsilon}^e$ and an inelastic, irreversible, part $\Delta\boldsymbol{\varepsilon}^c$. The incremental strain vector is given by:

$$\Delta\boldsymbol{\varepsilon} = \Delta\boldsymbol{\varepsilon}^e + \Delta\boldsymbol{\varepsilon}^c \tag{4.9}$$

The incremental strain vector in Eq.4.9 refers to the global coordinate axes. The sub-decomposition of the incremental crack strain $\Delta\boldsymbol{\varepsilon}^c$ gives the possibility of modeling several cracks that simultaneously occur and appears as:

$$\Delta\boldsymbol{\varepsilon}^c = \Delta\boldsymbol{\varepsilon}^{c1} + \Delta\boldsymbol{\varepsilon}^{c2} + ... \tag{4.10}$$

where $\Delta\boldsymbol{\varepsilon}^{c1}$ is the incremental global crack strain owing to a primary crack, $\Delta\boldsymbol{\varepsilon}^{c2}$

is that owing to a secondary crack and so on. As highlighted in Rots (1988), the essence of this approach is that at each fixed crack is assigned its own local incremental crack strain vector $\Delta\boldsymbol{\varepsilon}_l^{ci}$, its own incremental traction vector $\Delta\boldsymbol{\sigma}_l^{ci}$, where l indicates the local system and its own transformation matrix $\mathbf{N}^i$, and i indicates the i-th crack. The relation between local and global incremental crack strains for a single fixed crack reads:

$$\Delta\boldsymbol{\varepsilon}^{ci} = \mathbf{N}^i \Delta\boldsymbol{\varepsilon}_l^{ci} \tag{4.11}$$

with $\mathbf{N}^i$ being the transformation matrix accounting for the orientation of the crack. For a two dimensional configuration $\mathbf{N}^i$ is equal to:

$$\mathbf{N}^i = \begin{bmatrix} l_x^{i2} & l_x^i l_y^i \\ m_x^{i2} & m_x^i m_y^i \\ 2l_x^i m_x^i & l_x^i m_y^i + l_y^i m_x^i \end{bmatrix} \tag{4.12}$$

where l_x^i and m_x^i form a vector which indicates the direction of the local n-axis expressed in the global coordinates.

Lastly, the relation between the incremental global stress $\Delta\boldsymbol{\sigma}^i$ and the local incremental traction can be derived to be:

$$\Delta\boldsymbol{\sigma}_l^{ci} = \mathbf{N}^{iT} \Delta\boldsymbol{\sigma}^i \tag{4.13}$$

Considering that:

$$\Delta\boldsymbol{\sigma}^i = \mathbf{D}^{ei} \Delta\boldsymbol{\varepsilon}^{ei} \tag{4.14}$$

where $\mathbf{D}^{ei}$ is the linear-elastic stiffness matrix, it is also possible to obtain a relation between the local incremental crack strain and the incremental crack traction:

$$\Delta\boldsymbol{\sigma}_l^{ci} = \mathbf{D}^{ci} \Delta\boldsymbol{\varepsilon}_l^{ci} \tag{4.15}$$

where $\mathbf{D}^{ci}$ is the 2×2 crack matrix.

It is convenient to assemble these single-crack vectors and matrices into:

$$\Delta\tilde{\boldsymbol{\varepsilon}}_l{}^c = \begin{bmatrix} \Delta\boldsymbol{\varepsilon}_l^{c1} & \Delta\boldsymbol{\varepsilon}_l^{c2} & .... \end{bmatrix}^T \tag{4.16}$$

$$\Delta\tilde{\boldsymbol{\sigma}}_l{}^c = \left[\Delta\boldsymbol{\sigma}_l^{c1} \quad \Delta\boldsymbol{\sigma}_l^{c2} \quad ....\right]^T \tag{4.17}$$

$$\tilde{\mathbf{N}} = \left[\mathbf{N}^1 \quad \mathbf{N}^2 \quad ....\right]^T \tag{4.18}$$

in which $\tilde{}$ denotes the assembly of multi-directional cracks. Replacing of Eq.4.11 into Eq.4.10 yields:

$$\Delta\boldsymbol{\varepsilon}^c = \tilde{\mathbf{N}}\Delta\tilde{\boldsymbol{\varepsilon}}_l{}^c \tag{4.19}$$

which is the incremental strain for the multiple-crack equivalent of Eq.4.11. In a similar way, the single-crack traction-strain relation Eq.4.13 can be expanded for an equivalent multiple-crack as:

$$\Delta\tilde{\boldsymbol{\sigma}}_l{}^c = \tilde{\mathbf{D}}^c\Delta\tilde{\boldsymbol{\varepsilon}}_l{}^c \tag{4.20}$$

By properly combination of the equations above reported (4.9, 4.11, 4.13, 4.14, 4.15), the overall stress-strain relation is given by:

$$\Delta\boldsymbol{\sigma} = [\mathbf{D}^e - \mathbf{D}^e\tilde{\mathbf{N}}[\tilde{\mathbf{D}}^c + \tilde{\mathbf{N}}^T\mathbf{D}^e\tilde{\mathbf{N}}]^{-1}\tilde{\mathbf{N}}^T\mathbf{D}^e]\Delta\boldsymbol{\varepsilon} \ . \tag{4.21}$$

A more accurate and detailed description of a fixed single-crack formulation will be given in Chapter 5, according to the new element implementation formulated in FEAP (Taylor, 2017).

In the multi-directional fixed crack model, implemented in Diana, the first crack is formed perpendicular to the direction of the maximum principal stress. After that, another crack is allowed to form if the tensile strength is again overcome by the maximum principal stress and if the angle between the existing crack and the direction of the maximum principal stress exceeds a certain value, i.e. the threshold angle that is usually set to be 30° (Rots, 1988).

As a concern of the compressive response, Drucker-Prager plasticity model is briefly described. The yield condition of Drucker-Prager is a smooth approximation of the Mohr-Coulomb yield surface, described by a conical surface in the principal stress space. The formulation is given by:

$$f(\boldsymbol{\sigma}, \boldsymbol{\eta}, \kappa) = \sqrt{\frac{1}{2}(\boldsymbol{\sigma} - \boldsymbol{\eta})^T \mathbf{P}(\boldsymbol{\sigma} - \boldsymbol{\eta}) + \alpha_f \boldsymbol{\pi}^T(\boldsymbol{\sigma} - \boldsymbol{\eta}) - \beta \bar{c}(\kappa)} \tag{4.22}$$

with $\bar{c}(\kappa)$ the cohesion as a function of the internal state variable κ, and η is the back stress. $\mathbf{P}$ and $\boldsymbol{\pi}$ are the projection matrix and projection vector, respectively. The scalar quantities α_f and β are given by:

$$\alpha_f = \frac{2sin\phi(\kappa)}{3 - sin\phi(\kappa)}, \quad \beta = \frac{6cos\phi_0}{3 - sin\phi} \tag{4.23}$$

The internal friction angle ϕ is also a function of the internal state variable. Its initial value is given by ϕ_0. The flow rule is given by a general non-associated flow rule $g \neq f$, with the plastic potential given by:

$$g(\boldsymbol{\sigma}, \boldsymbol{\eta}, \kappa) = \sqrt{\frac{1}{2}(\boldsymbol{\sigma} - \boldsymbol{\eta})^T \mathbf{P}(\boldsymbol{\sigma} - \boldsymbol{\eta}) + \alpha_g \boldsymbol{\pi}^T(\boldsymbol{\sigma} - \boldsymbol{\eta})} \tag{4.24}$$

with the scalar α_g defined by the dilatancy angle ψ:

$$\alpha_g = \sqrt{\frac{2sin\psi(\kappa)}{3 - sin\psi(\kappa)}} \tag{4.25}$$

The plastic strain vector flow rule results as:

$$\dot{\varepsilon_p} = \dot{\lambda}\left\{\frac{\mathbf{P}(\boldsymbol{\sigma} - \boldsymbol{\eta})}{2\,\Psi} + \alpha_g \boldsymbol{\pi}\right\} \tag{4.26}$$

whit the scalar Ψ defined by:

$$\Psi = \sqrt{\frac{1}{2}(\boldsymbol{\sigma} - \boldsymbol{\eta})^T \mathbf{P}(\boldsymbol{\sigma} - \boldsymbol{\eta})} \tag{4.27}$$

The evolution of back stress $\boldsymbol{\eta}$ is given as:

$$\dot{\boldsymbol{\eta}} = \frac{2}{3}(1 - \gamma)\frac{\beta}{1 + 2\alpha_f \alpha_g}\frac{\delta \bar{c}}{\delta \kappa}\dot{\kappa}\left\{\frac{\mathbf{P}(\boldsymbol{\sigma} - \boldsymbol{\eta})}{2\,\Phi} + \alpha_g \boldsymbol{\pi}\right\} \tag{4.28}$$

where γ is a scalar parameter which acts only in the cohesion hardening. The role of the internal state variable κ in the plastic process is given by the hardening hypothesis. For the Drucker-Prager yield condition, only the strain hardening

hypothesis is considered. A more detailed description will be given in the next section 4.1.3. A strain-hardening is introduced in the model to overcome some shortcomings of the described classical model in reproducing masonry's real response.

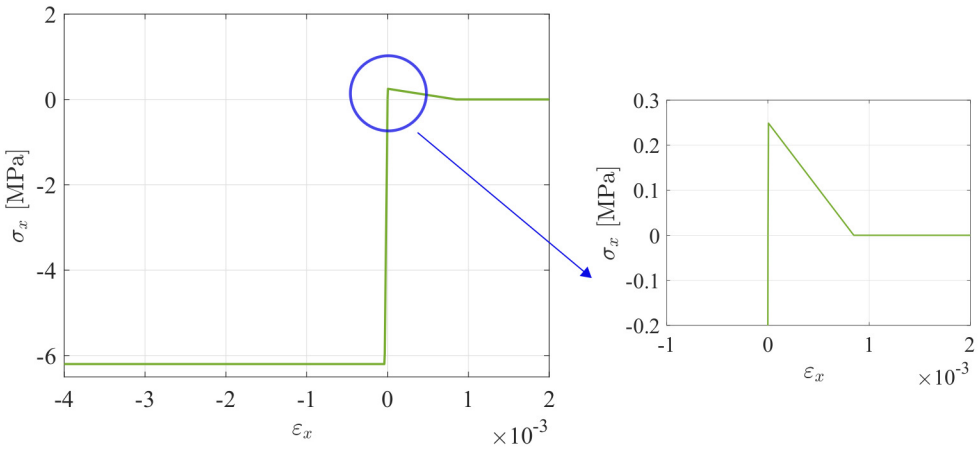

Figure 4.4: Masonry stress-strain law: tensile and compressive law for CP model.

Lastly, as for the TSRC model, the cracking phenomenon is governed by the shape of the tensile softening, depending on the fracture energy G_t. For this study, post-peak tensile stresses decrease following a linear law (see Figure 4.4). The Drucker - Prager plastic model described before controls the compressive response (see Figure 4.4). The numerical investigation, presented in 4.1.4, highlights that the two material macromechanical models, TSRC and CP, show some limitations when analyzing the behavior of masonry structures subjected to in-plane cyclic loading. In particular, the numerical models cannot describe the hysteretic dissipation mechanisms, which is the area under the experimental cyclic curves, particularly relevant for the nonlinear response of the squat panels. A modified version of the Drucker-Prager model, including cohesive softening, is introduced and described in the following.

4.1.3 Modified crack and plasticity model

The shortcomings of the described CP model, limiting its capability to reproduce the real response of masonry are overcome, with the modified version proposed in the following. In particular, with the aim of describing the degrading phenomena also in compression, a cohesive softening is introduced in the Drucker-Prager model, giving rise to the so-called Modified Crack and Plasticity model (MCP). The compressive softening law is empirically included in the Drucker-Prager model with strain hardening, whereas the tensile response still follows a bi-linear branch. Consequently, the hardening-cohesion function in Figure 4.8 is implemented and added in the existing model, thus modifying the compressive response of the CP model.

In the case of strain hardening, the relation between the internal state variable κ and the plastic stains is given in the principal space by:

$$\dot{\kappa} = \sqrt{\frac{2}{3}(\dot{\varepsilon}_1^{p2} + \dot{\varepsilon}_2^{p2})} \tag{4.29}$$

with

$$\begin{bmatrix} \dot{\varepsilon}_1^p \\ \dot{\varepsilon}_2^p \end{bmatrix} = \dot{\lambda}\left(\frac{1}{2\Phi}\begin{bmatrix} 2\sigma_1 - \sigma_2 \\ -\sigma_1 + 2\sigma_2 \end{bmatrix} + \alpha_g \begin{bmatrix} 1 \\ 1 \end{bmatrix}\right) \tag{4.30}$$

Equation 4.29 can be elaborated in:

$$\dot{\kappa} = \dot{\lambda}\sqrt{1 + 2\alpha_g^2} \tag{4.31}$$

The derivation for a hardening- cohesion function with constant friction (ϕ_0) and dilatancy angle (ψ_0) equal to 30° and the strain hardening hypothesis is presented. Starting from a simple uni-axial test (see Figure 4.5), adopting a total strain constitutive law (see Section 4.1.1), it was possible to build the $\bar{c} - \kappa$ relation to add in the CP model. First, using the mechanical parameters reported in Table 4.1, the relation between σ_1 and total strain ε_1 is shown in Figure 4.6.

Figure 4.7 shows the uni-axial stress-plastic strain diagram. With the assumption $\sigma_1 \leq 0$, the uni-axial plastic strain rate is given by:

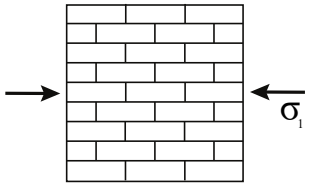

Figure 4.5: Uni-axial test .

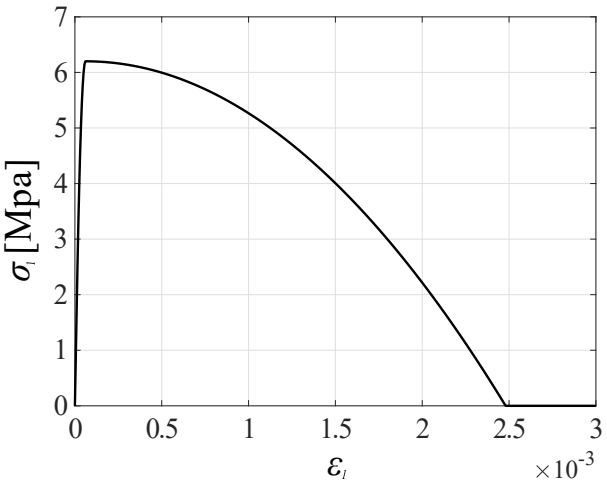

Figure 4.6: Uni-axial stress strain diagram $\sigma_1 - \varepsilon_1$.

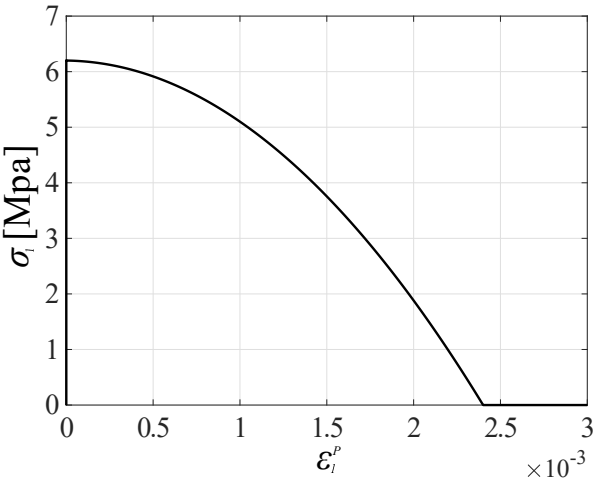

Figure 4.7: Uni-axial stress strain diagram $\sigma_1 - \varepsilon_1^p$.

$$\dot{\varepsilon}_1^p = -\dot{\lambda}(1 - \alpha_g) \tag{4.32}$$

The value of $\dot{\varepsilon}_1^p$ is obtained. Once defined α_g, following Eq. 4.25, it is possible to determine the relation between the uni-axial and internal state variable for a strain hardening hypothesis:

$$\dot{\kappa} = -\frac{\sqrt{1 + 2\alpha_g^2}}{1 - \alpha_g}\dot{\varepsilon}_1^p \tag{4.33}$$

Once fixed $\dot{\kappa}$, κ, which here takes on the hardening variable's meaning, is finally defined. Lastly, if the friction angle is constant, the relation between the uni-axial stress $\sigma_1 = -f_c$ and the equivalent cohesion $\bar{c}$ is given by:

$$\bar{c} = f_c\frac{1 - \alpha_f}{\beta} = f_c\frac{1 - sin\phi_0}{2cos\phi_0} \tag{4.34}$$

Then, the hardening - cohesion function is obtained and shown in Figure 4.8. Before adding the evaluated function in the CP model to analyze more complex cases, simple tests were performed to assess its efficiency. Indeed, Figure 4.9 shows the masonry stress-strain law adopted for the MCP model. It is interesting to note that an elastic-plastic law does not yet govern the compressive behavior, but, as we wanted, a strain-softening model is started.

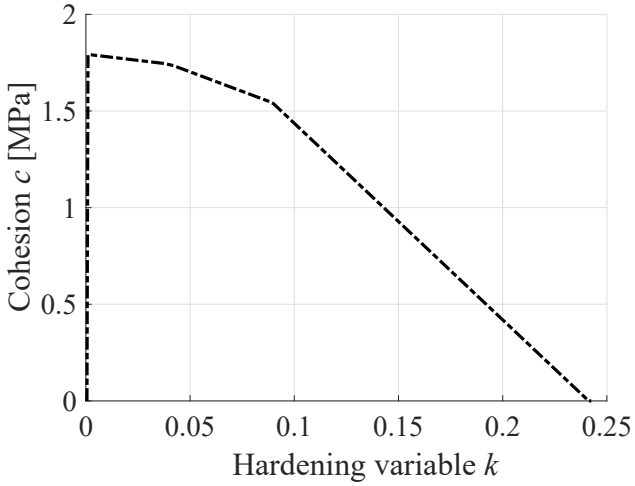

Figure 4.8: Cohesion hardening function.

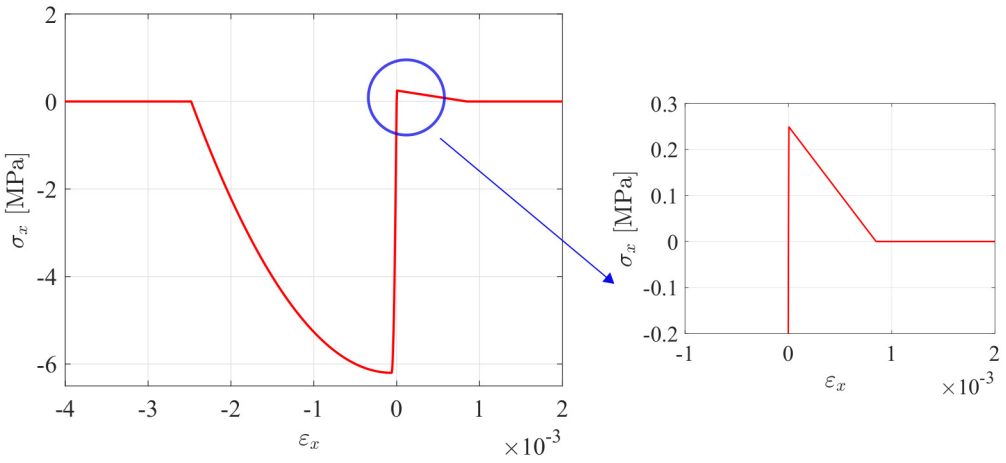

Figure 4.9: Masonry stress-strain law: tensile and compressive law for MCP model.

4.1.4 Numerical application

The experimental campaign conducted by Anthoine et al. (1995) is here considered (Figure 4.10). Two solid clay panels, characterized by different height/width ratio and assuming same boundary conditions, are investigated (Figure 4.11). The bottom side of the walls is completely restrained, while the top side is prevented from rotating. The panels are first subjected to a vertical force equal to 150 kN, kept constant during the test. Then, a cyclic horizontal displacement history is applied on a steel beam rigidly connected to the top of the walls. The lateral displacement is imposed quasi-statically and is characterized by a cyclically increasing amplitude. Two or three cycles are performed for each amplitude. The geometry of the panels is shown in Figures 4.11 (a) and (b) with the thickness equal to 250 mm.

The experimental response of these panels is compared with the numerical prediction of the macromechanical models described before. A 2D 4-point quadrilateral FEs based on a plane stress formulation and a 2x2 Gauss integration rule is adopted. A mesh made of 10x20 FEs is used for the high panel, while 10x14 FEs are adopted for the low panel. To overcome the mesh-dependency of the FE solution, the smeared crack models presented above, TRSC and CP, employ a fracture energy regularization (see Section 2.4.2). The mechanical parameters used in the

FE models deduced from Magenes and Calvi (1997) are contained in Table 4.1, where E is the Young's modulus, ν the Poisson ratio, σ_t and σ_c are the tensile and compressive strength values, respectively, G_t and G_c the value of tensile and compressive fracture energy terms chosen according to Lourenço (2010), and Γ is the masonry mass density. For the CP model, the other mechanical parameters (c and ϕ_0 deduced from Eq.4.34 and ψ_0 suggested by Rots (1988)) need to be defined, see Table 4.2.

E [MPa]	ν	σ_t [MPa]	σ_c [MPa]	G_t [N/mm]	G_c [N/mm]	Γ $[T/mm^3]$
1700	0.15	0.25	6.2	0.015	1	$1.652e^{-9}$

Table 4.1: Mechanical parameters adopted for TSRC and CP models.

c [MPa]	ϕ_0 [rad]	ψ_0 [rad]
1.7898	0.5236	0

Table 4.2: Additional mechanical parameters adopted for CP models.

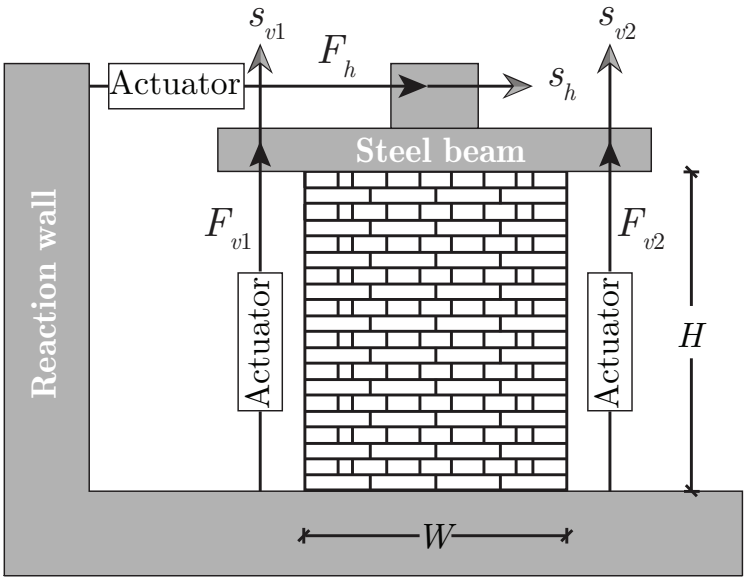

Figure 4.10: Experimental campaign: setup from Anthoine et al. (1995).

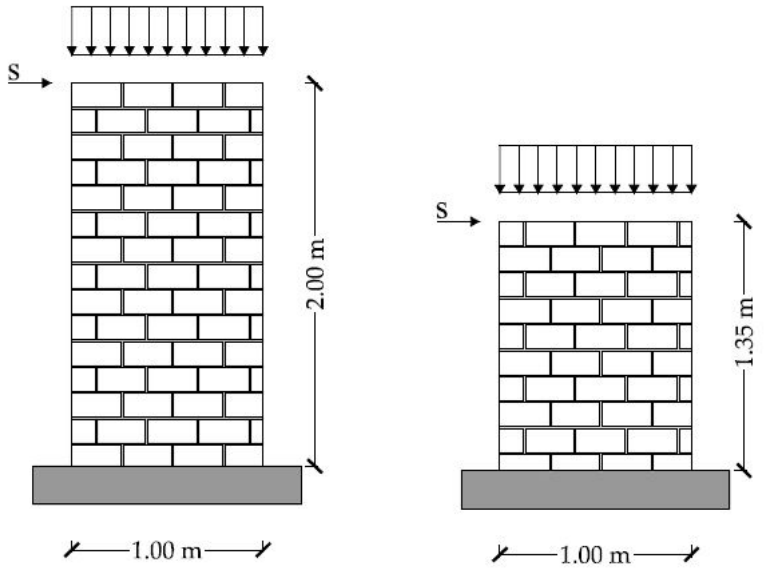

Figure 4.11: Geometry of the (a) high and (b) low panel.

Following the experimental loading history, a vertical force equal to 150 kN is applied and kept constant during the test. Then, a monotonic horizontal displacement history is imposed on the top of the walls. The results are monitored in terms of global in-plane response curve, meaning the envelope capacity curve, by depicting the total base shear versus the horizontal applied displacement. Figure 4.12 shows the comparison between the numerically obtained curves (red dashed and blue dashed-point curves) and the envelopes (black star symbols) corresponding to the cyclic experimental response for the high (Figure 4.12(a)) and low (Figure 4.12(b)) panels. Although some differences emerge between the two models, the numerical results are in a quite good agreement with the experimental ones. The TSRC model (blue dashed-point curves) gives a smoother nonlinear response, whereas the CP (red dashed curves) shows sudden drops due to crack's formation. Moreover, in the case of the squat (low) panel, the TSRC also shows a sudden brittle strength loss that is not clear for the CP model.

Regarding the cyclic tests performed within the selected experimental campaign, the cyclic displacement-history shown in Figure 4.13 is applied to the two

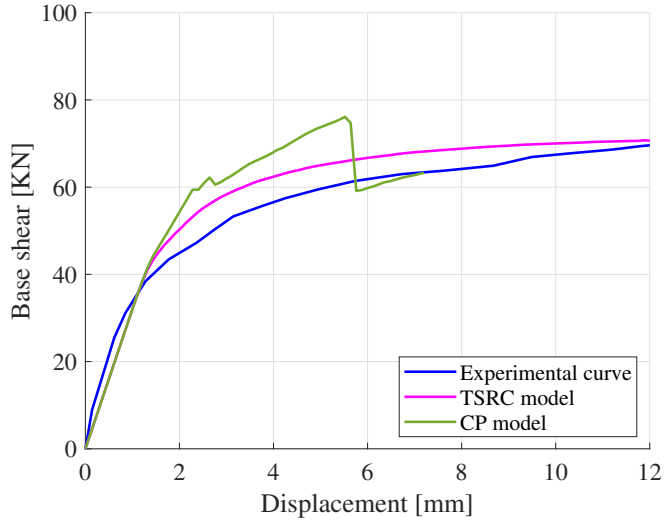

(a)

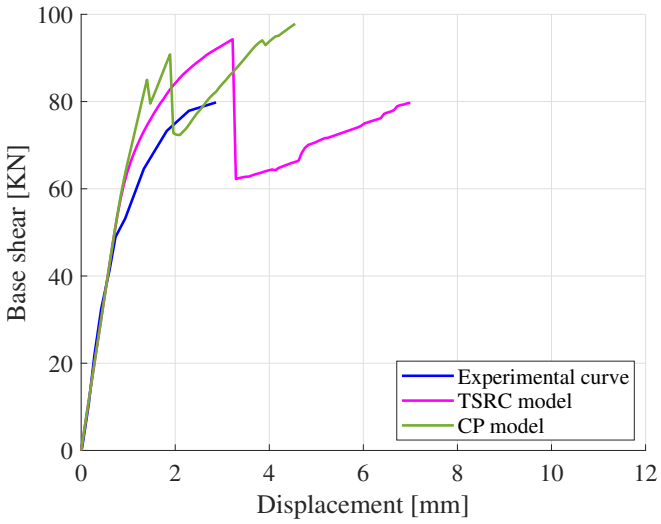

(b)

Figure 4.12: Comparisons between experimental and numerical (TSRC and CP) force-displacement response curve under monotonic loading: (a) high (slender) panel, and (b) low (squat) panel.

panels. The results obtained with the two FE models, the TSRC (blue dashed-point curves) and CP (red dashed curves) models, are presented in Figures 4.14 and Figure 4.15 and compared with the experimental outcomes (black star sym-

bols) for high and low panels in terms of force-displacement global curve.

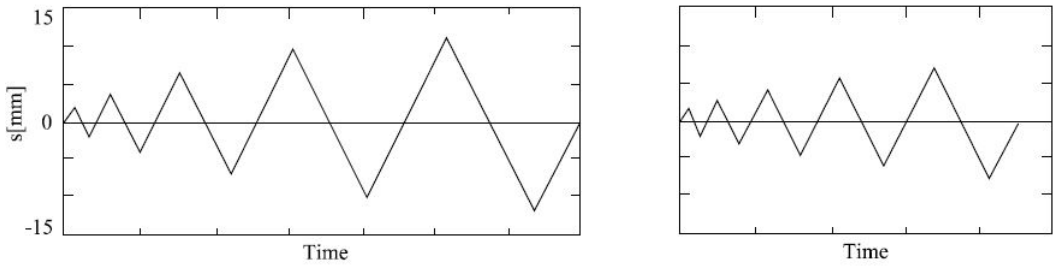

(a) (b)

Figure 4.13: Cyclic displacementet history applied to high (a) and low (b) panel.

Figure 4.14 shows a different trend for the global response curves of both models. It can be explained by the different damage mechanisms that arise during the evolution of the numerical and experimental tests. Indeed, the low wall shows a brittle failure response, with the formation of shear diagonal crack in the middle of the panel. The height-to-length aspect ratio of the geometry has a significant influence on the failure mode of masonry walls under cyclic action in the above respects.

A shear mechanism characterizes the response of the low panel; in converse the high wall shows a flexural failure with the formation of large damaged zones located at the top and bottom sides. Although the monotonic numerical analyses seem to reproduce well the damage mechanisms occurring in the two panels (Figures 4.16 and 4.17), the comparison of the numerical and the cyclic experimental results is not very satisfactory. In particular, the numerical models are unable to describe the hysteretic dissipation mechanisms, which is the area under the experimental cyclic curves, particularly relevant for the nonlinear response of the low panel.

To overcome the latter limitation of both models in matching the experimental response, the modified version of the CP formulation, i.e. the MCP model, is adopted as introduced in Section 4.1.3.

Figure 4.18 shows the comparison between the results obtained with the MCP model (magenta dashed curves) and the experimental outcomes (black star symbols) for both the panels. The numerical results obtained for the high panel

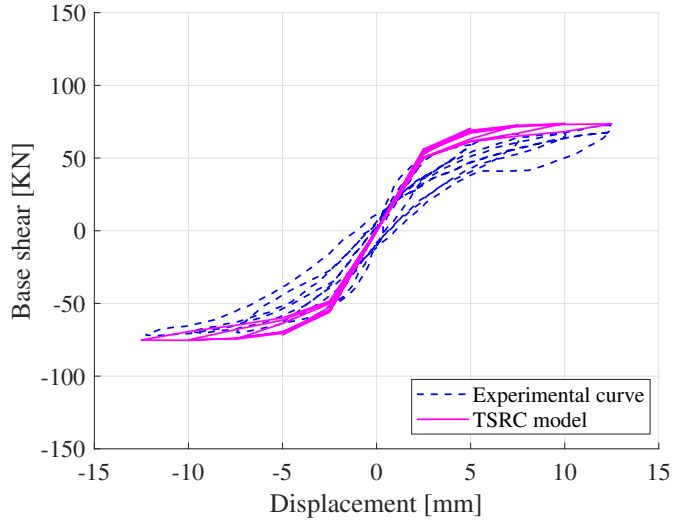

(a)

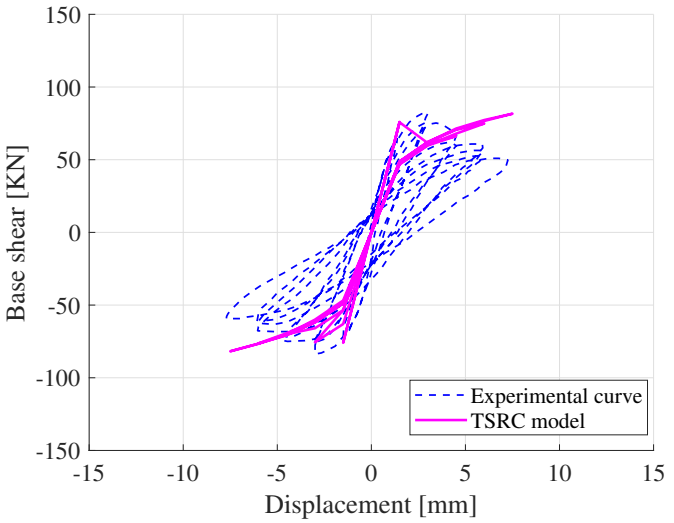

(b)

Figure 4.14: Comparison between experimental and numerical (TSRC) force-displacement response curve under cyclic loading :(a) high and (b) low panel.

correlates now better with the experimental response. Yet, the advantage of using the MCP model is less evident in the case of low panel. To be noted is that, in this model, the plasticity evolution is controlled by the cohesion that is, by itself, ruled by the compressive strength. Therefore, an experimental compressive

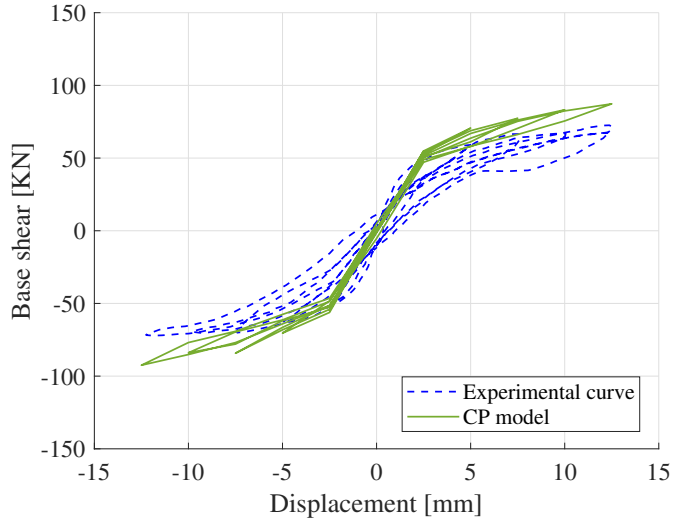

(a)

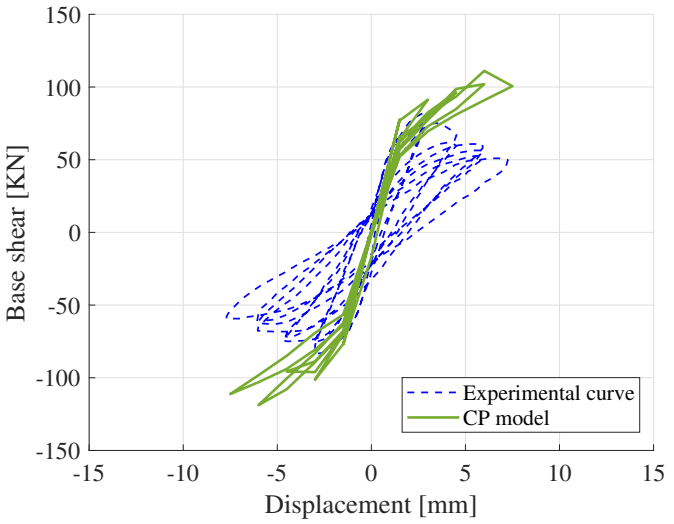

(b)

Figure 4.15: Comparison between experimental and numerical (CP) force-displacement response curve under cyclic loading :(a) high and (b) low panel.

strength value, the effect of plasticity is not properly taken into account during the dissipation process. Instead, an experimental cohesion value, numerical results are more consistent with the experimental ones, although the compressive strength threshold seems to be unrealistic. This issue deserves further investigations.

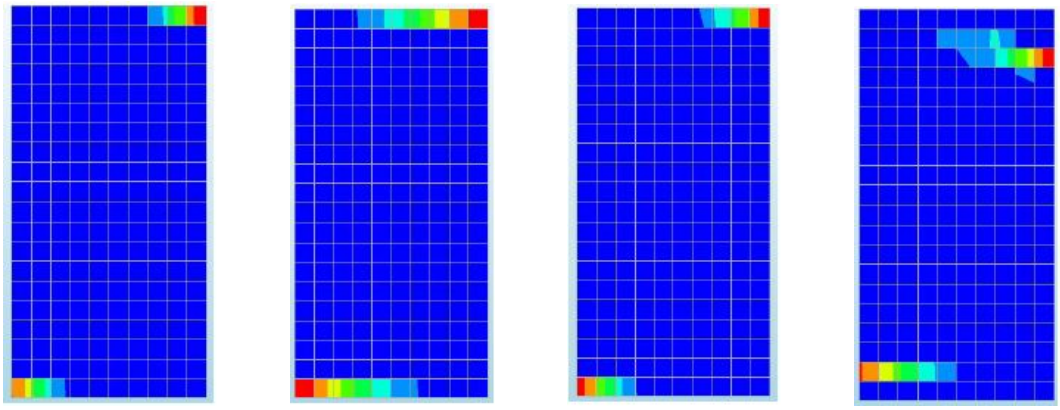

(a) (b) (c) (d)

Figure 4.16: Crack patterns for the high (slender) wall: (a) TRSC s=2 mm; (b) TRSC s=12 mm;(c) CP s=2 mm; and (d) CP s= 6 mm.

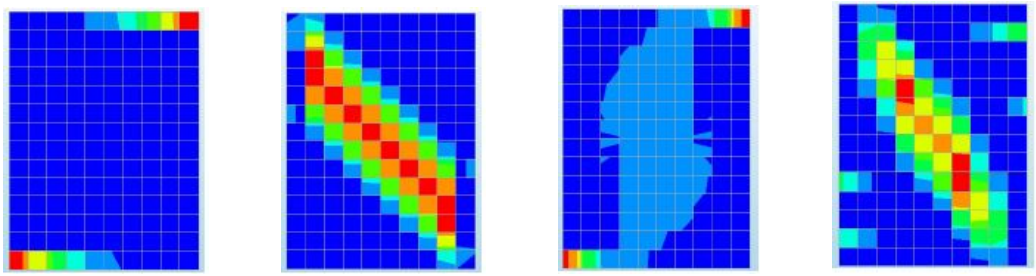

(a) (b) (c) (d)

Figure 4.17: Crack patterns for the low (squat) wall: (a) TRSC s=2 mm; (b) TRSC s=7 mm;(c) CP s=2 mm; and (d) CP s= 4 mm

Furthermore, a comparison with the macromechanical continuum damage-plastic model presented in Gatta et al. (2018) is performed (Figure 4.19). The damage-plastic model reproduces better the experimental responses, especially for the low wall. Indeed, this satisfactorily describes the energy dissipation effect due to shear mechanisms occurring in the panel. A different plasticity formulation is used here to reproduce better the global response that characterizes the failures, usually grown for the masonry structures.

Regarding the crack patterns (Figure 4.20), both the MCP and the damage-plastic CDP models are able to describe the distinctive features of flexural and

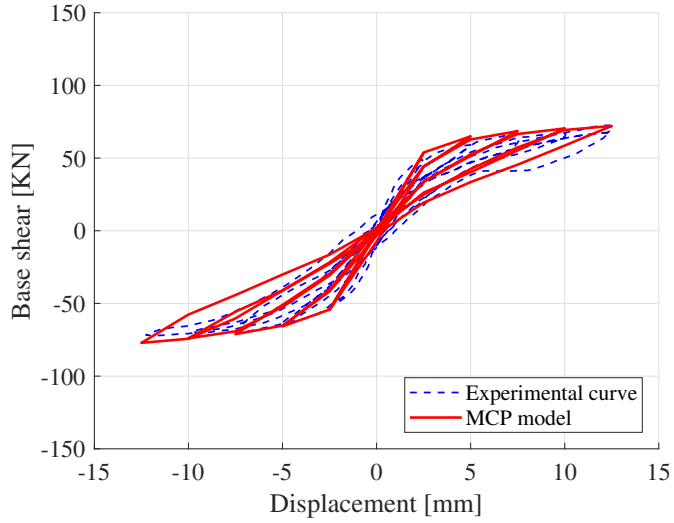

(a)

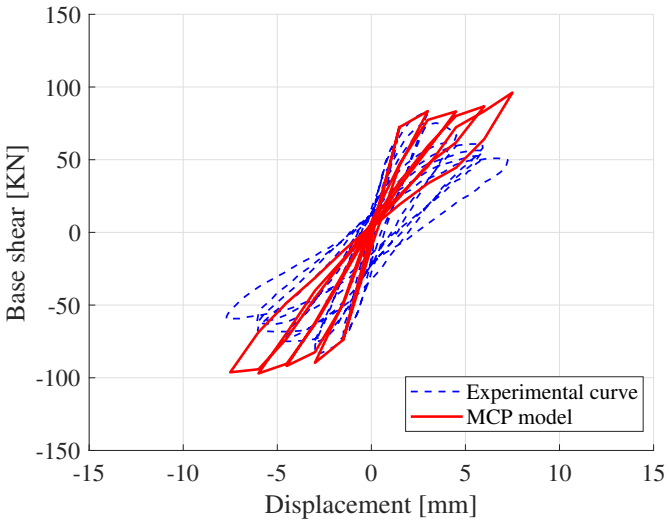

(b)

Figure 4.18: Comparison between experimental and numerical (MCP) force-displacement response curve under cyclic loading :(a) high and (b) low panel.

shear response shown by the high and low masonry panels, although the latter model gives more spread damaged in respect to the MCP. This is due to the different way that both models describe the degrading behavior of masonry, that is by means of the introduction of a continuum damage variable or adopting a smeared

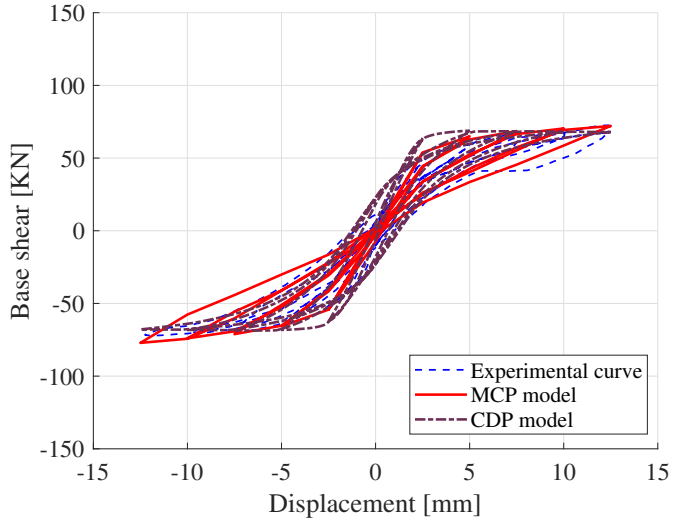

(a)

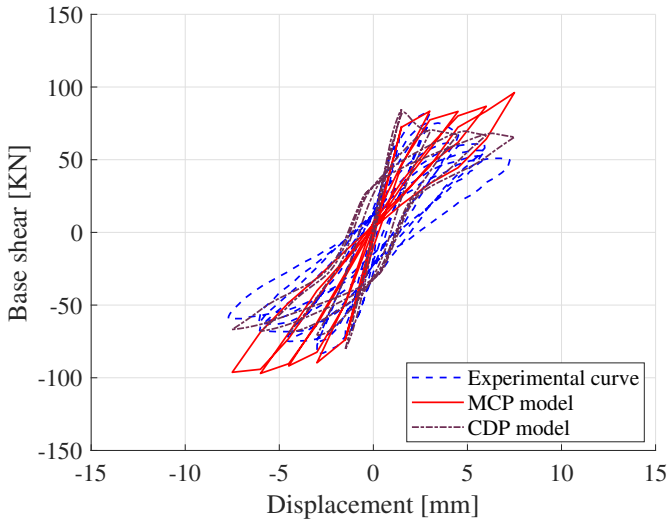

(b)

Figure 4.19: Comparison between experimental and numerical (MCP and CDP) force-displacement response curve under cyclic loading :(a) high and (b) low panel.

crack formulation, as well as to the different regularization technique used, fracture energy regularization for the smeared crack models and non-local integral approach for the damage-plastic continuum model. Concerning the regularization issues topic, detailed analyses will be made in Chapter 5.

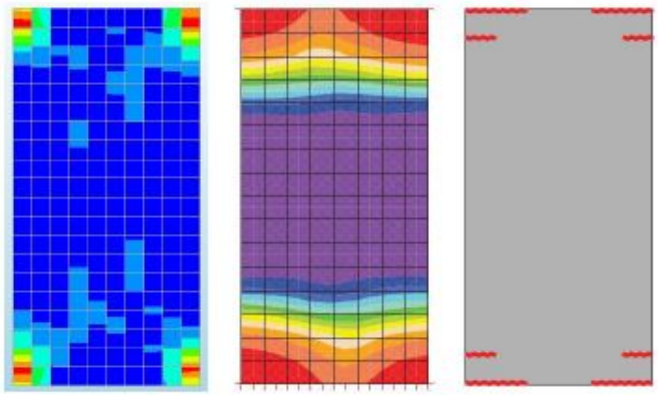

(a)

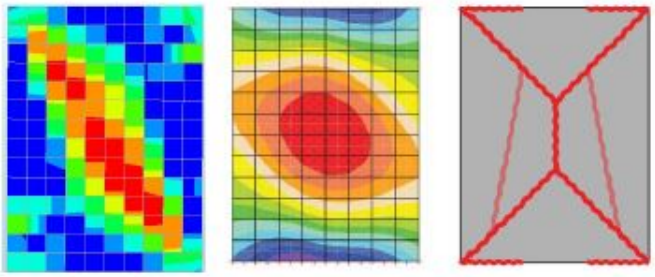

(b)

Figure 4.20: Ispra (a) high and (b) low wall: crack distribution, at the end of the analyses, for the MCP model (first column) implemented in DIANA code (DIANA, 2019), distribution of the damage for the CDP model (second column) implemented in FEAP code (Taylor, 2017) and experimental failure paths (third column) from Anthoine et al. (1995).

4.2 Summary

The structural response of two masonry panels experimentally tested by Anthoine et al. (1995) has been numerically reproduced through different macromechanical FE models: (i) based on the smeared crack approach; and (ii) based on a continuum damage-plastic model. In particular, the use of these two macro-modeling techniques for the cyclic in-plane response prediction of these masonry panels was explored. A fracture energy regularization technique was used for the smeared crack models and a non-local integral approach for the continuum damage-plastic model. Two material constitutive macro-models, known as Total Strain Cracking

(TSRC) and Crack and Plasticity (CP), have been used to simulate the response of the two panels. These have different geometries and, therefore, different damage paths. Indeed, a shear mechanism characterized the behavior of the low panel. In converse, a flexural rocking response distinguished the high wall with the formation of large damaged zones located at the top and bottom sides. The numerical models have showed some shortcomings, i.e. although the numerical analyses have showed a good agreement reproducing the damage mechanisms, the comparisons in terms of force-displacement curves were not completely satisfactory. Regarding the TSRC model, the numerical results were consistent with the model formulation built just with a cracking constitutive law. Conversely, although the CP model is based on a coupled cracking-plastic constitutive law, its formulation presents some limitations when taking into account the effect of plasticity during the dissipation process. The latter issues were somehow solved through a modified version of the Drucker-Prager model (MCP) by including an implemented cohesive softening law in the existing CP model. For the high wall, the numerical results correlate better with the experimental output with respect to the CP and TSRC models. For the low wall, the correlation was still not very satisfactory and other modifications are required. Lastly, a comparison between the MCP model, categorized as a smeared crack model, and a CDP macromechanical continuum damage-plastic model (Gatta et al., 2018) was performed. This latter sophisticated model, where damage and plasticity are coupled, proved to be more capable to reproduce the experimental outcomes in terms of force-displacement global curve.

Chapter 5

Regularized smeared crack model

In this chapter, the implementation of a single-fixed smeared crack model in FEAP code (Taylor, 2017) into a finite element procedure is illustrated. Details about the computational aspects are provided. To avoid the well-known numerical problems typical of finite element models, due to strain localization and subsequent spurious mesh sensitivity, two different approaches are used: fracture energy and nonlocal integral regularization. Analyses of typical structures, used to prove the robustness and stability of these two approaches, are presented. A comparison between them is shown.

5.1 A single-fixed smeared crack model

Following the strategy adopted in Sena-Cruz (2005) formulation, the single-fixed smeared crack model is described. As mentioned above, in Section 2.3.2, after crack initiation, the basic assumption of smeared crack model is the decomposition of the incremental strain vector $\Delta\boldsymbol{\varepsilon}$, into an incremental crack strain vector, $\Delta\boldsymbol{\varepsilon}^c$, and an incremental elastic strain vector, $\Delta\boldsymbol{\varepsilon}^e$, and thus:

$$\Delta\boldsymbol{\varepsilon} = \Delta\boldsymbol{\varepsilon}^e + \Delta\boldsymbol{\varepsilon}^c \tag{5.1}$$

Herein, a two dimensional formulation is considered. A local coordinate system is defined with axes n and t, being the crack normal and tangential directions, respectively.

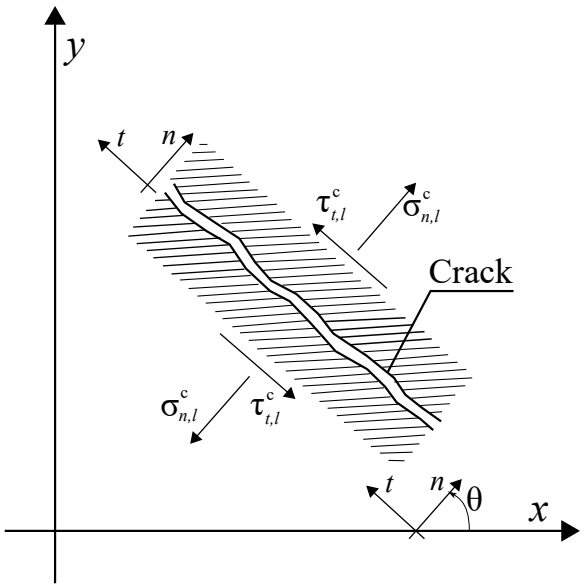

Figure 5.1: Crack stresses, relative displacements and local coordinate system of the crack (adapted from Sena-Cruz (2005)).

Hence, the incremental crack strain vector $\Delta\boldsymbol{\varepsilon}_l^c$ in the local system is defined as:

$$\Delta\boldsymbol{\varepsilon}_l^c = \begin{bmatrix} \Delta\varepsilon_{n,l}^c & \Delta\gamma_{t,l}^c \end{bmatrix}^T \tag{5.2}$$

The incremental crack strain vector in the global coordinate system $\Delta\boldsymbol{\varepsilon}^c$ has the following three components:

$$\Delta\boldsymbol{\varepsilon}^c = \begin{bmatrix} \Delta\varepsilon_x^c & \Delta\varepsilon_y^c & \Delta\gamma_{xy}^c \end{bmatrix}^T \tag{5.3}$$

The transformation matrix $\mathbf{N}$ of the incremental crack strain vector from the global system to the local reads:

$$\mathbf{N} = \begin{bmatrix} \cos^2\theta & \sin^2\theta & 2\sin\theta\cos\theta \\ -\sin\theta cos\theta & \sin\theta cos\theta & \cos^2\theta - \sin^2\theta \end{bmatrix} \tag{5.4}$$

and

$$\mathbf{N}^T = \begin{bmatrix} \cos^2\theta & -\sin\theta\cos\theta \\ \sin^2\theta & \sin\theta cos\theta \\ 2\sin\theta cos\theta & \cos^2\theta - \sin^2\theta \end{bmatrix} \tag{5.5}$$

hence the incremental global crack strain is defined by:

$$\Delta\boldsymbol{\varepsilon}^c = \mathbf{N}^T \Delta\boldsymbol{\varepsilon}_l^c \tag{5.6}$$

being θ the angle between x and n (see Figure 5.1). The incremental local crack stress vector $\Delta\boldsymbol{\sigma}_l^c$ is defined by:

$$\Delta\boldsymbol{\sigma}_l^c = \begin{bmatrix} \Delta\sigma_{n,l}^c & \Delta\tau_{t,l}^c \end{bmatrix}^T \tag{5.7}$$

where $\Delta\sigma_{n,l}^c$ and $\Delta\tau_{t,l}^c$ are the incremental crack normal and shear stresses, respectively. The relationship between $\Delta\boldsymbol{\sigma}_l^c$ and the incremental stress vector $\Delta\boldsymbol{\sigma}$ can be defined as:

$$\Delta\boldsymbol{\sigma}_l^c = \mathbf{N}\Delta\boldsymbol{\sigma} \tag{5.8}$$

Assuming linear elastic behavior for the undamaged material, the constitutive relationship between $\Delta\boldsymbol{\varepsilon}^e$ and $\Delta\boldsymbol{\sigma}$ is given by:

$$\Delta\boldsymbol{\sigma} = \mathbf{D}^e \Delta\boldsymbol{\varepsilon}^e \tag{5.9}$$

where $\mathbf{D}^e$ is the linear elastic constitutive matrix defined as:

$$\mathbf{D}^e = \frac{E}{(1-\nu^2)} \begin{bmatrix} 1 & \nu & 0 \\ \nu & 1 & 0 \\ 0 & 0 & \frac{(1-\nu)}{2} \end{bmatrix} \tag{5.10}$$

being E and ν the Young's modulus and Poisson ratio of the material, respectively. In a similar way, a relationship between $\Delta\boldsymbol{\sigma}_l^c$ and $\Delta\boldsymbol{\varepsilon}_l^c$ is established to simulate the crack opening and the shear sliding using a crack constitutive matrix $\mathbf{D}^c$

$$\Delta\boldsymbol{\sigma}_l^c = \mathbf{D}^c \Delta\boldsymbol{\varepsilon}_l^c \tag{5.11}$$

where $\mathbf{D}^c$ is a 2×2 matrix including mode I and mode II crack fracture parameters. Starting from incorporating the equations 5.1 and 5.6 into equation 5.9 yields, by combining the equations, a constitutive law of the cracked material is obtained:

$$\Delta\boldsymbol{\sigma} = \mathbf{D}^e(\Delta\boldsymbol{\varepsilon} - \mathbf{N}^T\Delta\boldsymbol{\varepsilon}_l^c) \tag{5.12}$$

Pre-multiplying both members of equation 5.12 by $\mathbf{T}$ leads to:

$$\mathbf{N}\Delta\boldsymbol{\sigma} = \mathbf{N}\mathbf{D}^e\Delta\boldsymbol{\varepsilon} - \mathbf{N}\mathbf{D}^e\mathbf{N}^T\Delta\boldsymbol{\varepsilon}_l^c \tag{5.13}$$

Substituting equation 5.9 into the left side of equation 5.13 yields reads as:

$$\Delta\boldsymbol{\sigma}_l^c + \mathbf{N}\mathbf{D}^e\mathbf{N}^T\Delta\boldsymbol{\varepsilon}_l^c = \mathbf{N}\Delta\boldsymbol{\sigma}\Delta\boldsymbol{\varepsilon} \tag{5.14}$$

Including equation 5.11 into the left side of equation 5.14, the following equation defining the incremental crack strain vector in the local system is obtained:

$$\Delta\boldsymbol{\varepsilon}_l^c = (\mathbf{D}^c + \mathbf{N}\mathbf{D}^e\mathbf{N}^T)^{-1}\mathbf{N}\mathbf{D}^e\Delta\boldsymbol{\varepsilon} \tag{5.15}$$

The inclusion of equation 5.15 in equation 5.12 leads to the constitutive law of the cracked material, which reads:

$$\Delta\boldsymbol{\sigma} = (\mathbf{D}^e - \mathbf{D}^e\mathbf{N}^T(\mathbf{D}^c + \mathbf{N}\mathbf{D}^e\mathbf{N}^T)^{-1}\mathbf{N}\mathbf{D}^e)\Delta\boldsymbol{\varepsilon} \tag{5.16}$$

or

$$\Delta\boldsymbol{\sigma} = \mathbf{D}^{cc}\Delta\boldsymbol{\varepsilon} \tag{5.17}$$

where $\mathbf{D}^{cc}$ is the following constitutive matrix for the cracked material:

$$\mathbf{D}^{cc} = \mathbf{D}^e - \mathbf{D}^e\mathbf{N}^T(\mathbf{D}^c + \mathbf{N}\mathbf{D}^e\mathbf{N}^T)^{-1}\mathbf{N}\mathbf{D}^e \tag{5.18}$$

In the present model the crack constitutive matrix $\mathbf{D}^c$ is assumed to be diagonal:

$$\mathbf{D}^c = \begin{bmatrix} D_I^c & 0 \\ 0 & D_{II}^c \end{bmatrix} \tag{5.19}$$

In this matrix D_I^c and D_{II}^c are the mode I and mode II stiffness modulus associated with the crack behavior. Evaluation of these will be described in the following sections, distinguishing the computational procedure on the basis of the adopted regularization technique. The crack-dilatancy effect and shear-normal stress coupling is not considered in the present approach. The shear-normal stress coupling, however, may be simulated indirectly, allowing non-orthogonal cracks to form and relating D_{II}^c with the crack normal strain.

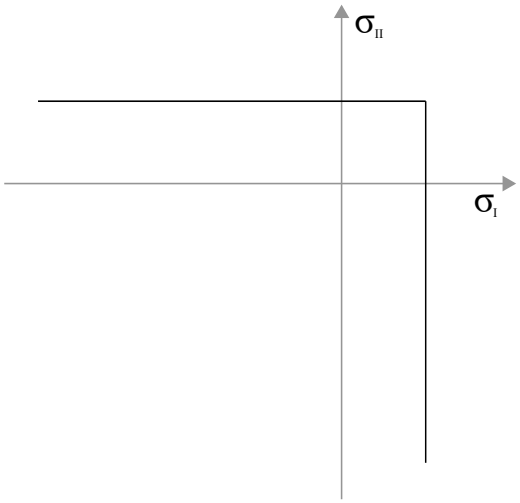

Figure 5.2: Rankine yield surface in the 2D principal stress space.

The crack initiation in the present model is governed by the Rankine yield surface (see Figure 5.2), i.e., when the maximum principal stress σ_I, exceeds the uni-axial tensile strength, f_{ct}, the crack is formed.

5.1.1 Fracture energy regularization

According to Rots (1988) in the local system, the relation between the crack stress $\sigma_{n,l}^c$ and the crack strain $\varepsilon_{n,l}^c$ in the normal direction can be written as follows:

$$\sigma_n^c = f_t y\left(\frac{\varepsilon_{n,l}^c}{\varepsilon_{n,l,ult}^c}\right) \tag{5.20}$$

in which f_t is the tensile strength and $\varepsilon_{n,l,ult}^c$ the ultimate crack strain. The general function y represents the actual softening. If the softening behavior on

the constitutive level is related to the mode I fracture energy G_f^I through an equivalent length or crack bandwidth denoted as h (as mentioned in section 2.4.2), the following relation can be derived:

$$G_f^I = h \int_{\varepsilon_{n,l}^c=0}^{\varepsilon_{n,l}^c=\infty} \sigma_{n,l}^c(\varepsilon_{n,l}^c) d\varepsilon_{n,l}^c \tag{5.21}$$

Substitution of equation 5.20 into equation 5.21 results:

$$G_f^I = h f_t \int_{\varepsilon_{n,l}^c=0}^{\varepsilon_{n,l}^c=\infty} y\left(\frac{\varepsilon_{n,l}^c}{\varepsilon_{n,l,ult}^c}\right) d\varepsilon_{n,l}^c \tag{5.22}$$

with the assumption that f_t is a constant. Change from the variable $\varepsilon_{n,l}^c$ to:

$$x = \left(\frac{\varepsilon_{n,l}^c}{\varepsilon_{n,l,ult}^c}\right) \tag{5.23}$$

and consequently $d\varepsilon_{n,l}^c = \varepsilon_{n,l,ult}^c dx$ it appears as:

$$G_f^I = h f_t \left(\int_{x=0}^{x=\infty} y dx\right) \varepsilon_{n,l,ult}^c \tag{5.24}$$

where the ultimate crack strain $\varepsilon_{n,l,ult}^c$ is finite and it reads as:

$$\varepsilon_{n,l,ult}^c = \frac{1}{\alpha} \frac{G_f^I}{h f_t} \tag{5.25}$$

with the factor α determined by the following integral:

$$\alpha = \int_{x=0}^{x=\infty} y(x) dx \tag{5.26}$$

The ultimate crack strain $\varepsilon_{n,l,ult}^c$ is a material property, which can be calculated from the tensile strength f_t, the fracture energy G_f^I and the element area represented by the equivalent length h. As mentioned in section 2.4.2, the correct value of h is influenced by the mesh size and the inclination of the crack band. Based on this type of evidence and on numerical experiments, Rots (1988) suggested certain rules for choosing the equivalent element size h, for several typical situations. A more rigorous approach was developed by Oliver (1989). These two method will be investigated with the following numerical applications.

For this model, a linear tension softening is chosen (see Figure 5.3).

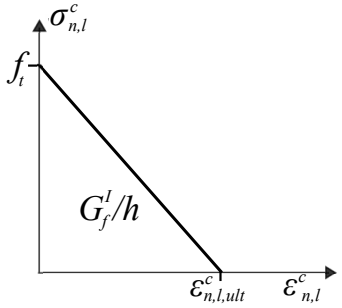

Figure 5.3: Linear tension softening.

The relation of the crack stress is given by:

$$\frac{\sigma^c_{n,l}}{f_f} = \begin{cases} 1 - \frac{\varepsilon^c_{n,l}}{\varepsilon^c_{n,l,ult}} & if \quad 0 < \varepsilon^c_{n,l} < \varepsilon^c_{n,ult} \\ 0 & if \quad \varepsilon^c_{n,l,ult} < \varepsilon^c_{n,l} < \infty \end{cases} \tag{5.27}$$

where

$$\varepsilon^c_{n,l,ult} = 2\frac{G^I_f}{hf_t} \tag{5.28}$$

and it is possible to define the mode I crack stiffness (see Eq. 5.19) as follows:

$$D^c_I = -\frac{f_t^2 h}{2G^I_f} \tag{5.29}$$

5.1.2 Nonlocal regularization

According to the regularization technique, based on the nonlocal integral approach, the nonlocal integral definition of the crack strain variable is introduced:

$$\Delta\bar{\boldsymbol{\varepsilon}}^c_l(\mathbf{x}) = \frac{1}{\int_{\Omega_r}\psi(\mathbf{x},\mathbf{s})d\Omega_r(\mathbf{s})}\int_{\Omega_r}\psi(\mathbf{x},\mathbf{s})\Delta\boldsymbol{\varepsilon}^c_l(\mathbf{s})d\Omega_r(\mathbf{s}) \tag{5.30}$$

where $\Delta\bar{\boldsymbol{\varepsilon}}^c_l$ is the nonlocal quantity at point $\mathbf{x}$, and $\Delta\boldsymbol{\varepsilon}^c_l$ is the corresponding local variable at the generic point located at $\mathbf{s}$ lying in the neighborhood of $\mathbf{x}$. The weight function ψ, measuring the influence of the generic point placed at $\mathbf{s}$ on the

analyzed point located at $\mathbf{x}$, is assumed as the classical Gaussian function:

$$\psi(\mathbf{x}, \mathbf{s}) = e^{-\left(\frac{\|\mathbf{x}-\mathbf{s}\|}{l_c}\right)^2} \tag{5.31}$$

being l_c the nonlocal radius related to the material internal characteristic length. Once the nonlocal strain in equation (5.30) is evaluated, this is used to solve the crack evolution problem. For this model, a linear tension softening is chosen (see Figure 5.4).

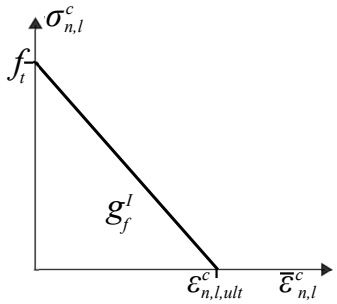

Figure 5.4: Linear tension softening.

The crack stress is given by:

$$\frac{\sigma^c_{n,l}}{f_f} = \begin{cases} 1 - \frac{\bar{\varepsilon}^c_{n,l}}{\varepsilon^c_{n,l,ult}} & if \qquad 0 < \bar{\varepsilon}^c_{n,l} < \varepsilon^c_{n,ult} \\ 0 & if \qquad \varepsilon^c_{n,l,ult} < \varepsilon^c_{n,l} < \infty \end{cases} \tag{5.32}$$

where,

$$\varepsilon^c_{n,l,ult} = 2\frac{g^I_f}{f_t} \tag{5.33}$$

and it is possible to define the mode I crack stiffness (see Eq. 5.19) as follows:

$$D^c_I = -\frac{f_t^2}{2g^I_f} \tag{5.34}$$

The modeling of the shear behavior is also introduced following the procedure described in section 4.1.1. Thus, the mode II crack stiffness modulus results as:

$$D^c_{II} = \frac{\beta}{1-\beta}G \tag{5.35}$$

5.1.3 Computational aspects

In this section computational aspects concerning the evaluation of the solution of the macromechanical problem are discussed. A user FE is implemented in the FEAP code (Taylor, 2017), formulated on the basis of the presented version of the constitutive law. Isoparametric quadrilateral 4-node FEs are introduced, each equipped with two translation displacement degrees of freedom, to model the material. The adopted FE procedure is standard. First the strain vector $\boldsymbol{\varepsilon}$, in the global coordinate system is computed, starting from element nodal displacement $\mathbf{u}^e$. Matrix $\mathbf{L}^e$ is defined as $\mathbf{L}^e = \mathbf{D}_x\mathbf{N}^e$, where $\mathbf{N}^e$ contains the $2D$ displacement shape functions, referred to the 4 element nodes, while matrix $\mathbf{L}^e = \mathbf{D}_x\mathbf{N}^e$ contains their derivatives according to the 2D compatibility operator, $\mathbf{D}_x$. Then, the stresses are evaluate (see Eq.5.9) by using the linear elastic constitutive matrix $\mathbf{D}^e$ defined in equation 5.10. Subsequently, according to the crack initiation in the present model, that is governed by the Rankine yield surface (see Figure 5.2), the maximum principal stress σ_I is calculated. If σ_I exceeds the uniaxial tensile strength,f_t, the crack is formed. Then the evolutionary problem of the crack governing the constitutive response is solved at each of the 2×2 quadrature points.

1. Compute strains $\boldsymbol{\varepsilon}$ starting from displacements $\mathbf{u}^e$:
   $\boldsymbol{\varepsilon} = \mathbf{L}^e\mathbf{u}^e$

2. Compute elastic stresses $\boldsymbol{\sigma}^e$:
   $\boldsymbol{\sigma}^e = \mathbf{D}^e\boldsymbol{\varepsilon}^e$

3. Calculate the maximum principal stress σ_I:

   if σ_I exceeds the uniaxial tensile strength f_t then solve crack evolution problem described above by using equations 5.6, 5.19 and 5.15 (fracture energy or nonlocal approach).

4. Compute stresses $\boldsymbol{\sigma}$ by using equation 5.17.

Table 5.1: Computational procedure for the model.

5.2 Numerical applications

To investigate localization and regularization issues, two classical numerical examples are selected analyzed by using the non regularized model that regularized with fracture energy, and the nonlocal integral regularized model. The first example concerns a variable cross section beam (see Figure 5.5).

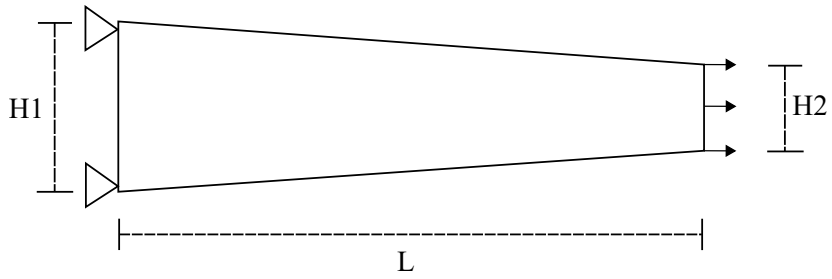

Figure 5.5: Variable cross section beam: geometry and load condition.

The mechanical parameters of the model are given in the Table 5.2, where E and ν denote the Young's modulus and Poisson coefficient, respectively.

E [MPa]	ν	σ_n [MPa]	G_f^I [N/mm]	g_f^I[MPa]
30000	0.2	3	0.3	9×10^{-4}

Table 5.2: Mechanical parameters adopted for the models.

The behavior of the variable-height beam subjected to an imposed displacement u at the end section is analyzed. The particular geometry of the beam induces the localization of deformations and damage in the region close to the end section, which is the one with the lowest height. The geometric characteristics are reported in Table 5.3.

$H1$ [mm]	$H2$ [mm]	L [mm]
100	50	500

Table 5.3: Geometry parameters adopted for the models.

Figure 5.6 shows the load-displacement curves obtained with the non regularized model. Three different discretizations made of 25, 50, and 100 elements are chosen, showing the dependence of the numerical solution on the number of elements adopted.

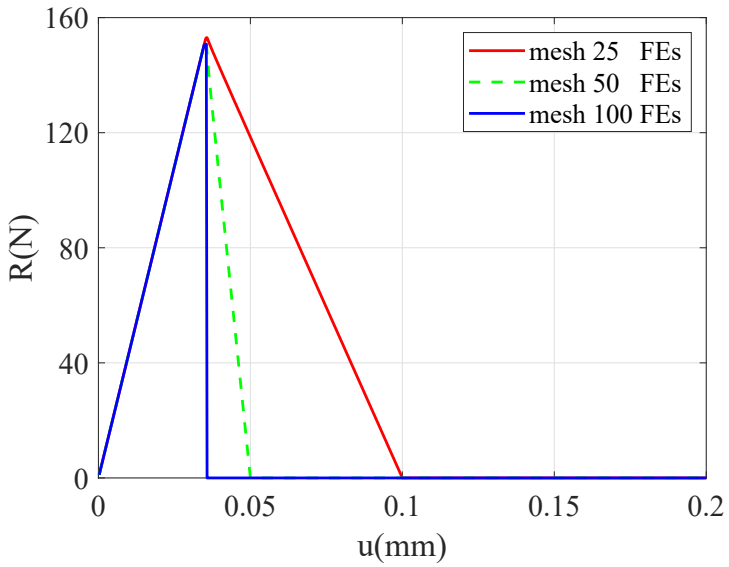

Figure 5.6: Non regularized load-displacement curves.

Subsequently, the analyses, performed with the fracture energy regularized model are provided. As mentioned above, the correct value of h is influenced by the mesh size and the inclination of the crack band to the mesh lines. Here, two methods are investigated. The first was suggested by Rots (1988), and for a linear two-dimensional element this is $h = \sqrt{2A}$, where A is the total area of the element. For this application, A is equal to the area of the last element, where crack occurs. In figure 5.7 the load-displacement curves are reported. The same previous meshes of 25, 50, and 100 elements are considered still showing a dependence of the numerical solution on the number of the elements adopted.

A more rigorous approach was developed by Oliver (1989). Different values of the equivalent crack length are defined for quadrilateral and triangular linear elements related to different crack patterns (see Figure 5.8). For this application, the h value is defined as following:

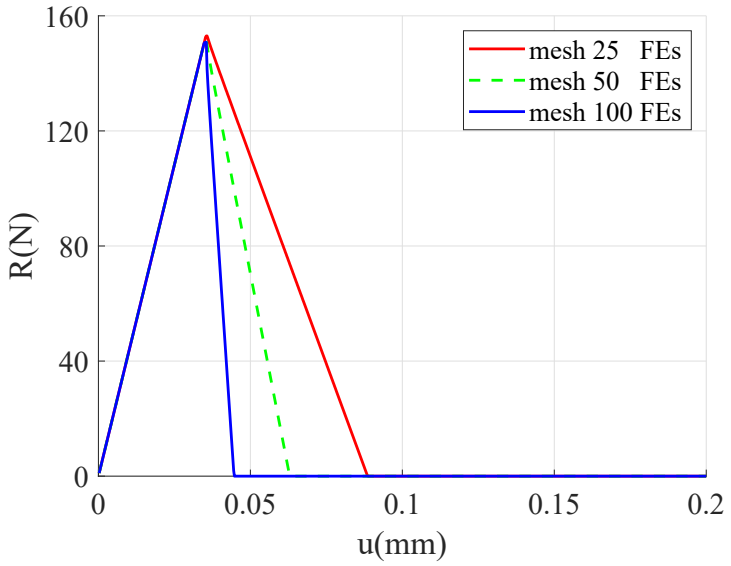

Figure 5.7: Fracture energy regularization using Rots' method (Rots, 1988): load-displacement curves.

$$h = \frac{A}{d} \tag{5.36}$$

where A, in this case, is equal to the area of the last element and d (referring to Figure 5.8) reads:

$$d = \frac{(y_3 - y_2) + (y_4 - y_1)}{2} \tag{5.37}$$

In figure 5.9 the load-displacement curves are given. The three different discretizations of 25, 50, and 100 elements are considered showing the independence of the numerical solution on the number of elements adopted. This method better avoids the numerical problem and the effectiveness of the regularization technique can be seen. To be noted is that the crack propagation remains concentrated in the last element (see Figure 5.10).

At the end, figure 5.11 presents the results obtained by adopting the non-local integral regularized model with the three different discretizations showing the almost complete independence of the numerical solution from the number of elements adopted, with $l_c = 30\ mm$. As shown in figure 5.12, in this case the

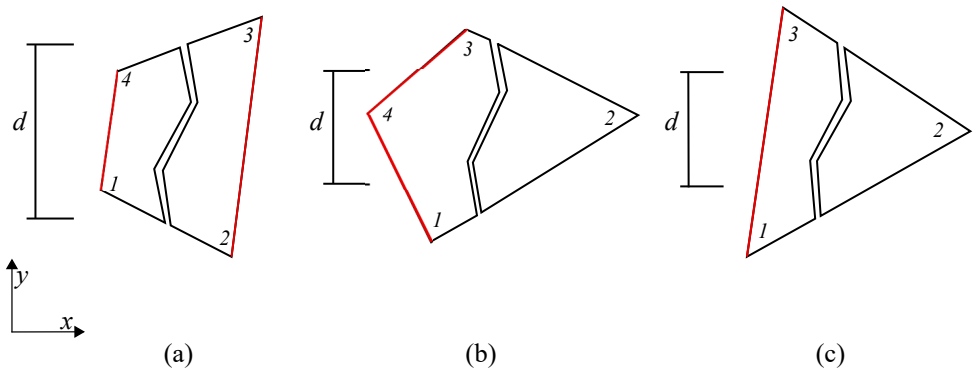

Figure 5.8: Explicit values of the equivalent crack length for quadrilateral and triangular linear elements related to different crack patterns (adapted from Oliver (1989)).

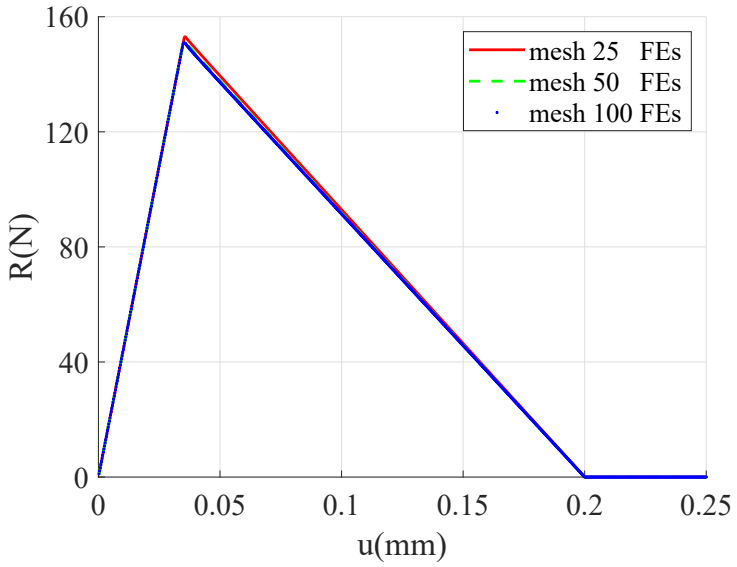

Figure 5.9: Fracture energy regularization using Oliver' method (Oliver, 1989): load-displacement curves.

crack propagation also involves the elements adjacent to the last one, giving an objective measure of the cracked zone.

In the second example the response of the weak element beam shown in figure 5.13 is studied. The mechanical parameters of the model are reported in Table 5.4.

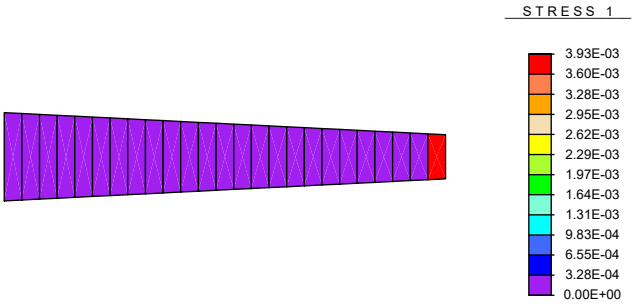

(a) mesh 25 FEs

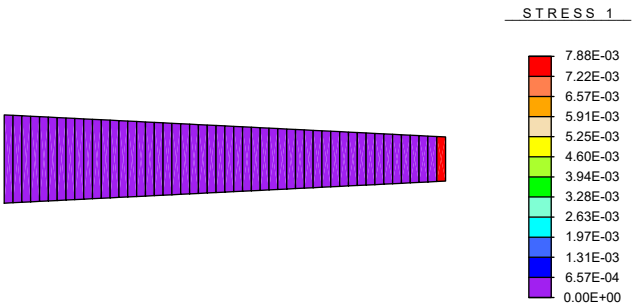

(b) mesh 50 FEs

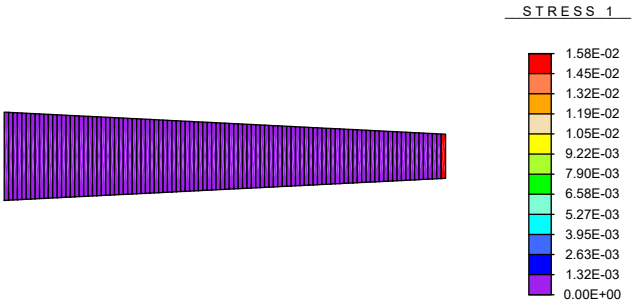

(c) mesh 100 FEs

Figure 5.10: Crack strain patterns with fracture energy regularization for u = 0.1 *mm*: (a) mesh 25 FEs (b) mesh 50 FEs and (c) mesh 100 FEs.

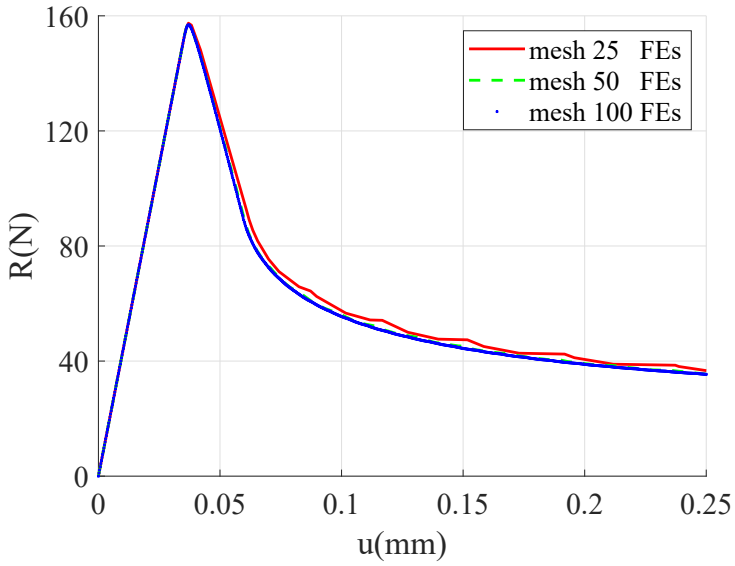

Figure 5.11: Nonlocal integral regularized smeared-crack model: load-displacement curves.

E [MPa]	ν	σ_n [MPa]	G_f^I [N/mm]	g_f^I[MPa]
1700	0.15	0.25	0.012	2×10^{-4}

Table 5.4: Mechanical parameters adopted for the models.

The week element beam is subjected to an imposed displacement u at the end section is analyzed. The central element is made weaker than the others by assigning it a Young's modulus $\tilde{E}$ equal to $0.9E$. The geometric characteristics are reported in Table 5.5.

H [mm]	L [mm]
50	500

Table 5.5: Geometry parameters adopted for the models.

The localization of the deformations and crack is induced in the area of the weak central element. Figure 5.14 shows the load-displacement curves obtained with the non regularized model. Three different discretizations of 25, 50, and 100

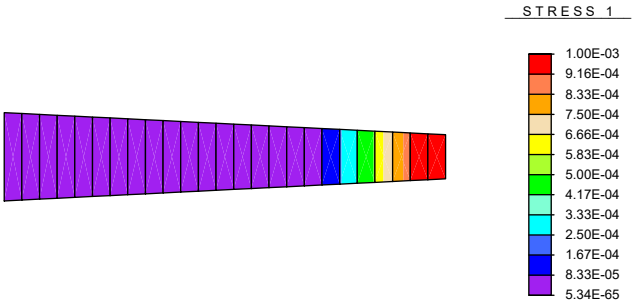

(a) mesh 25 FEs

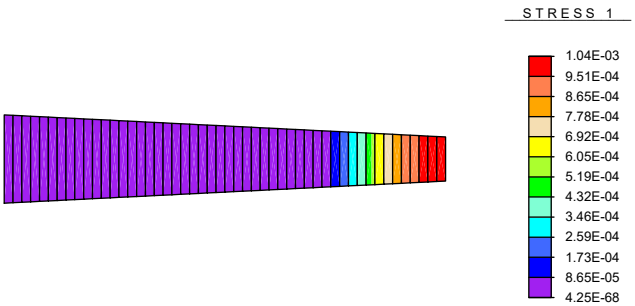

(b) mesh 50 FEs

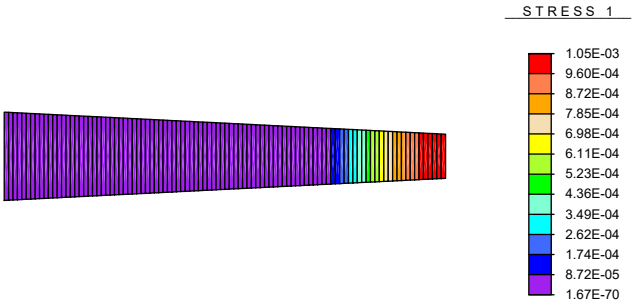

(c) mesh 100 FEs

Figure 5.12: Crack strain patterns with nonlocal integral regularization for u = 0.1 *mm*: (a) mesh 25 FEs (b) mesh 50 FEs and (c) mesh 100 FEs.

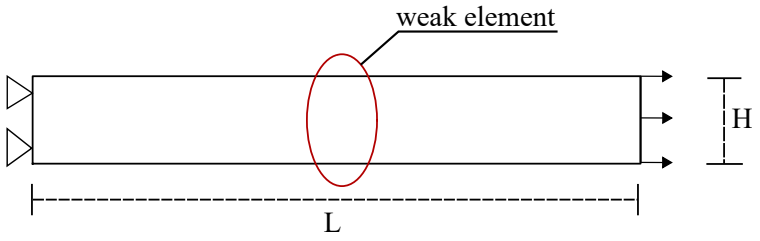

Figure 5.13: Weak element beam: geometry and load condition.

elements are chosen, showing the dependence of the numerical solution on the number of elements adopted.

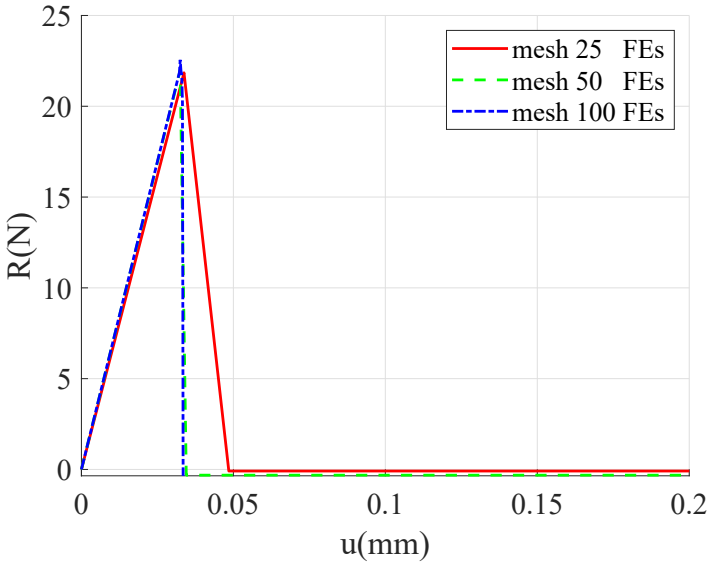

Figure 5.14: Non regularized load-displacement curves.

Subsequently, the analyses, performed with the fracture energy regularized model are provided. In figure 5.15 the load-displacement curves referring to the adoption Rots' method (Rots, 1988) are reported. The above three different discretizations are considered showing a dependence of the numerical solution on the number of elements adopted.

In figure 5.16 the load-displacement curves are given, by using the approach developed by Oliver (1989). The results obtained by adopting the three different discretizations of 25, 50, and 100 elements show the independence of the numerical solution on the number of elements adopted. Also for this second example,

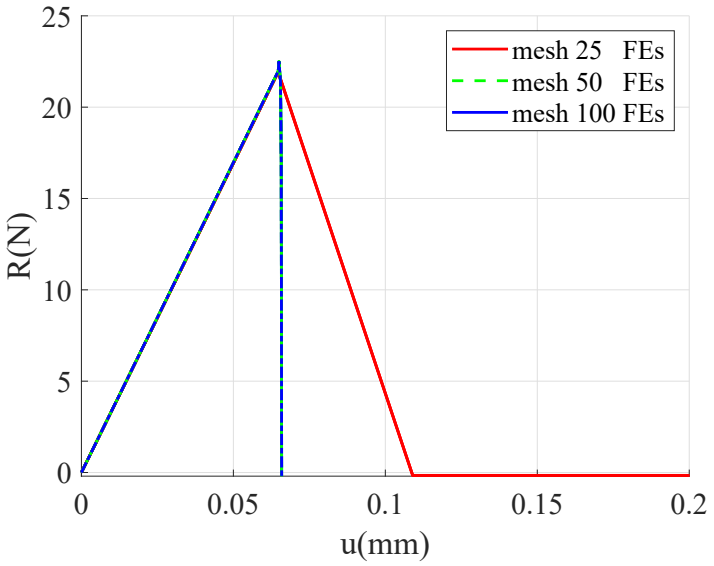

Figure 5.15: Fracture energy regularization using Rots' method (Rots, 1988): load-displacement curves.

this method better avoids the numerical problem and the effectiveness of the regularization technique can be noticed. The crack propagation is located just in the weaker central element (see Figure 5.18).

Figure 5.17 presents the results obtained by adotping the nonlocal integral regularized model with three different discretizations of 25, 50, and 100 elements, respectively, showing the almost complete independence of the numerical solution from the number of elements adopted. The adopted characteristic length is $l_c = 20\ mm$. As shown in figure 5.19 the crack propagation also involves the elements adjacent to the weaker central one, giving an objective measure of the cracked zone.

5.3 Summary

A single-fixed smeared crack model was implemented in the FEAP code (Taylor, 2017) into a finite element procedure. Details about the computational aspects were also provided. To avoid the well-known numerical problems typical of finite element models, due to strain localization and subsequent spurious mesh sensi-

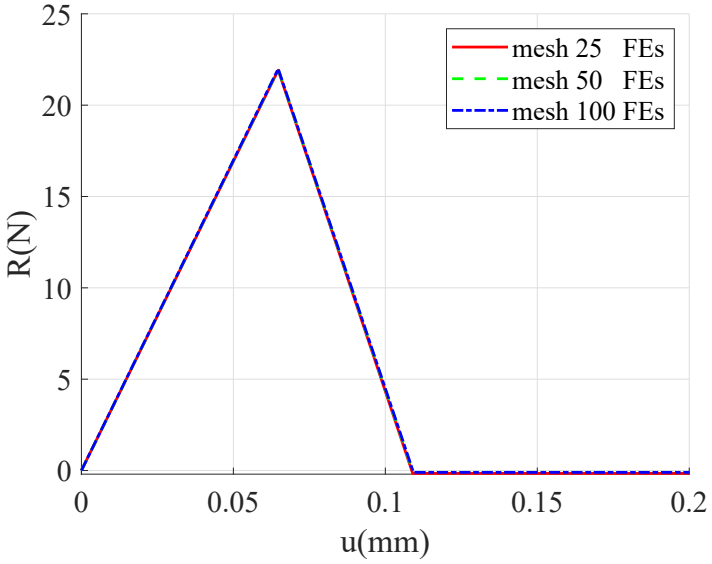

Figure 5.16: Fracture energy regularization using Oliver' method (Oliver, 1989): load-displacement curves.

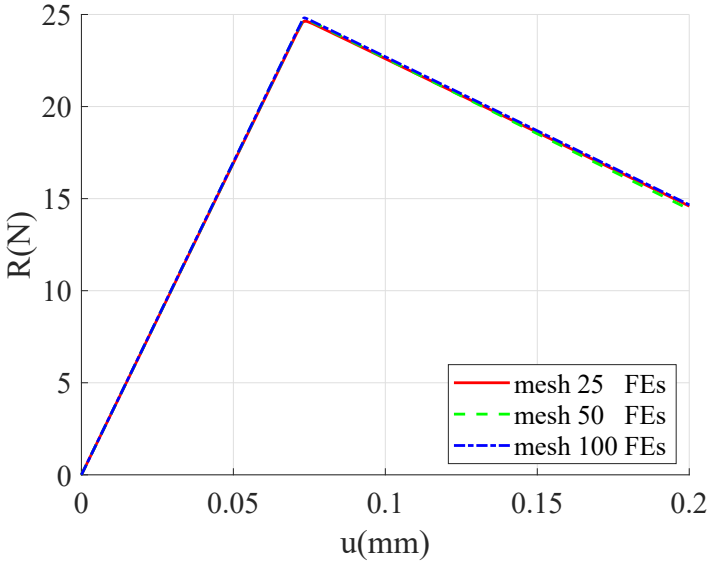

Figure 5.17: Nonlocal integral regularized smeared-crack model: load-displacement curves.

tivity, two different approaches were used: fracture energy and nonlocal integral regularization. Regarding the first approach it emerged that the choice of the

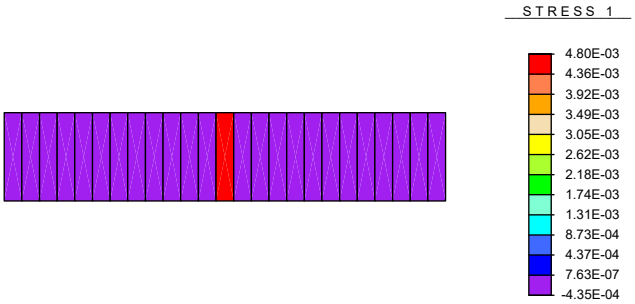

(a) mesh 25 FEs

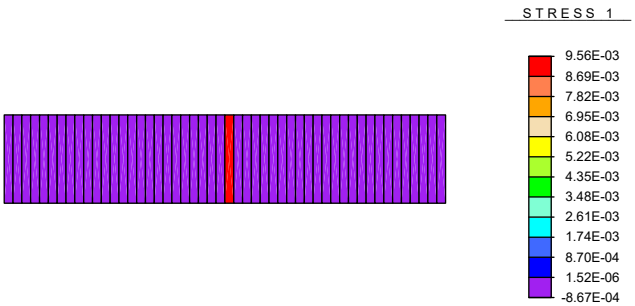

(b) mesh 50 FEs

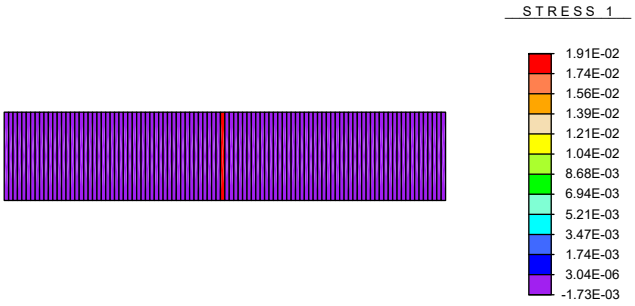

(c) mesh 100 FEs

Figure 5.18: Crack strain patterns with fracture energy regularization for u = 0.1 *mm*: (a) mesh 25 FEs (b) mesh 50 FEs and (c) mesh 100 FEs.

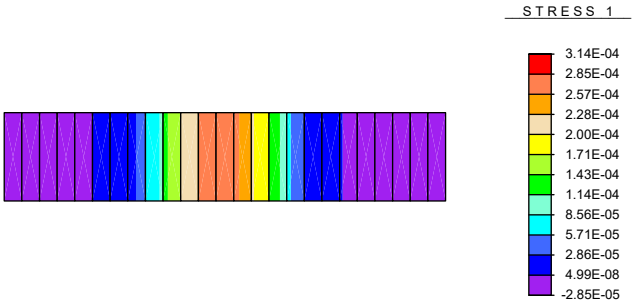

(a) mesh 25 FEs

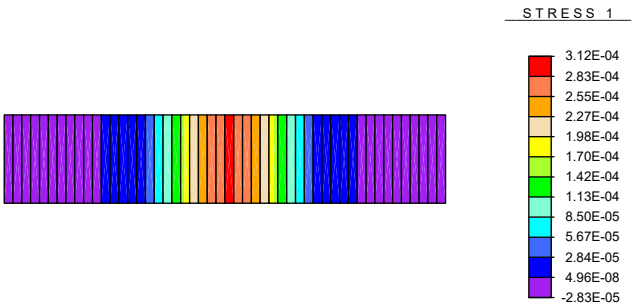

(b) mesh 50 FEs

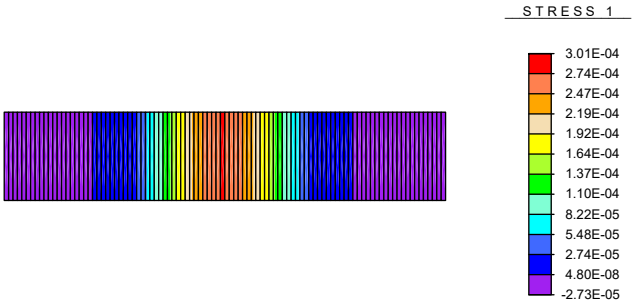

(c) mesh 100 FEs

Figure 5.19: Crack strain patterns with nonlocal integral regularization for u = 0.1 *mm*: (a) mesh 25 FEs (b) mesh 50 FEs and (c) mesh 100 FEs.

equivalent element size h is a difficult task. The Rot's method (Rots, 1988) was not able to show satisfactory mesh independence of the numerical results. The technique developed by Oliver (1989) better avoids the numerical problem, and the effectiveness of the regularization technique was obtained. Lastly, the nonlocal regularization, consisting of introducing a nonlocal variable associated with the crack strain, was proved to be effective. Indeed, the numerical results obtained from both the examples, using the nonlocal crack model, showed complete mesh independence of the numerical solutions and a realist crack propagation.

Chapter 6

Conclusive remarks

The principal goal of this research was the investigation of finite element modeling of masonry structures at different scales and the study of micromechanical and macromechanical constitutive laws able to describe, accurately, the nonlinear masonry behavior.

However, as emphasized in Chapter 2, some recurrent features can be identified, such as the strongly nonlinear material response, the anisotropic behavior, and different collapse mechanisms relating to the main structures, thus walls and arches. To numerically capture such nonlinear phenomena and collapse mechanisms, the scientific literature proposes several modeling strategies, analyses and possible constitutive laws.

Herein, first in Chapter 3 a damage-plastic model for the micromechanical analysis of 2D masonry structures, formulated to study masonry structural elements characterized by general geometry and arrangement, was presented. The model was implemented in a finite element procedure, which adopts a nonlocal integral formulation to provide objective numerical results in case of strain-softening. Moreover, a predictor-corrector procedure, based on the splitting method, is adopted to solve the nonlinear evolution problem of damage and plasticity variables. To validate the model, a comparison between numerical and experimental outcomes was performed for masonry walls. Then, the structural response of unreinforced masonry arches has been numerically analyzed. First, model efficiency and accuracy has been tested by reproducing the outcomes of experimentally

tested arches (Oliveira et al., 2010). Subsequently, parametric analyses have been performed to investigate the effects of some relevant geometric and mechanical parameters. As concerns the influence of geometry, numerical tests have been carried out by varying the thickness/internal radius ratio. It emerged that, as the ratio t/R increases, failure mechanism moves from four flexural hinges to a mixed mode involving both flexural and shear hinges, leading to a more brittle behavior. Regarding the mechanical parameter effects, a strong influence of the mortar tensile strength and the mode I fracture energy has appeared on the trend of the global response, mainly affecting the collapse load value and the brittleness of the post-peak response. The adopted procedure has proved to well reproduce the results coming from the limit analysis approach, when the assumptions of this last are approached. Moreover, it emerged that the arch collapse mechanism depends on the assumed friction coefficient value: for fixed geometry, the failure mode involving shear sliding changes into the flexural hinge mechanism, as friction increases. However, the limit value that determines the variation of the failure mode is a peculiar characteristic of each arch, being influenced by the coupled effect of geometry and friction.

Subsequently, in Chapter 4, the use of macromodeling techniques based on smeared crack constitutive laws for the cyclic in-plane response prediction of masonry panels was explored. Two material constitutive macro-models, known as total strain cracking and crack and plasticity, have been used to simulate the response of a low and a high panel. These have different geometries and, therefore, different damage paths. A shear mechanism characterized the behavior of the low panel, conversely, a flexural rocking response distinguished the high wall with the formation of large damaged zones located at the top and bottom sides. The numerical models showed some shortcomings, i.e. although the numerical analyses showed a good agreement reproducing the damage mechanisms, the comparisons in terms of force-displacement curves were not completely satisfactory. Regarding the total strain cracking model, the numerical results were consistent with the model formulation built just with a cracking constitutive law. Conversely, although the crack and plasticity model is based on a coupled cracking-plastic constitutive law, its formulation presents some limitations when taking into account the effect of plasticity during the dissipation process. The latter issues were

somehow solved through a modified version of the Drucker-Prager model by including an implemented cohesive softening law in the existing crack and plasticity model. For the high wall, the numerical results correlate better with the experimental output with respect to the crack and plasticity and total strain cracking models. For the low wall, the correlation was still not very satisfactory and other modifications are required.

Lastly, a single-fixed smeared crack model was implemented to avoid the well-known numerical problems typical of finite element models, due to strain localization and subsequent spurious mesh sensitivity. Two different approaches were used: fracture energy and nonlocal integral regularization. Regarding the first approach it emerged that the choice of the equivalent element size h is a difficult task. The Rot's method (Rots, 1988) was not able to show satisfactory mesh independence of the numerical results. The technique developed by Oliver (1989) better avoids the numerical problem, and the effectiveness of the regularization technique was obtained. However the nonlocal regularization, consisting of introducing a nonlocal variable associated with the crack strain, was effective. Indeed, the numerical results obtained from both the examples showed complete mesh independence of the numerical solutions and a realist damage distribution.

To conclude, present and future developments are listed here:

- other experimental campaigns on masonry arches and/or complex structures may be chosen to analyze different geometries and loading conditions and investigate the applicability of damage-friction model on different types of masonry;

- other experimental campaigns on masonry panels and/or larger structures, may be considered to further validate the capabilities of the smeared crack numerical models to reproduce the masonry response under cyclic-loading conditions and to better understand its advantages and limitations. Furthermore, the analyzed constitutive models can be enriched, in particular the modified crack and plasticity formulation, through rigorous mechanically based modifications inspired by continuum damage-plastic models;

- masonry panels and/or complex structures may be chosen to prove the ro-

bustness and stability of fracture energy and nonlocal integral regularization. These strategies are needed to account efficiently for the highly nonlinear behavior of the masonry material and to avoid localized structural response.

Bibliography

Abbaneo, S., Baronio, G., Binda, L., Tiraboschi, C., 1993. Murature in pietra: classificazione ed indagini preliminari per la scelta e la progettazione delle miscele di iniezione. Convegno "Murature, Sicurezza, recupero , 185–222.

Addessi, D., 2000. Modelli di danno regolarizzati per materiali fragili. Sapienza, Università di Roma, Italy. Ph.D. thesis .

Addessi, D., 2014. A 2D Cosserat finite element based on a damage-plastic model for brittle materials. Computers & Structures 135, 20–31.

Addessi, D., Di Re, P., Sacco, E., 2017. A micro-macro homogenization for modeling the masonry out-of-plane response, in: XXIII AIMETA Congresso Associazione Italiana di Meccanica Teorica e Applicata, Salerno, Italy.

Addessi, D., Di Re, P., Sacco, E., 2020a. Micromechanical and multiscale computational modeling for stability analysis of masonry elements. Engineering Structures 211, 110428.

Addessi, D., Liberatore, D., Masiani, R., 2015. Force-based beam finite element (fe) for the pushover analysis of masonry buildings. International Journal of Architectural Heritage 9, 231–243.

Addessi, D., Liberatore, D., Nocera, M., 2020b. Damaging behavior of masonry arch bridges: Analysis of 'ponte delle torri'in spoleto, italy. Journal of Earthquake Engineering , 1–26.

Addessi, D., Marfia, S., Sacco, E., 2002. A plastic nonlocal damage model. Computer Methods in Applied Mechanics and Engineering 191, 1291–1310.

Addessi, D., Sacco, E., 2011. Cauchy and Cosserat equivalent continua for the multiscale analysis of periodic masonry walls, in: Zavarise, G., Wriggers, P. (Eds.), Trends in Computational Contact Mechanics. Springer Berlin Heidelberg. volume 58 of *Lecture Notes in Applied and Computational Mechanics*, pp. 253–268.

Addessi, D., Sacco, E., 2012. A multi-scale enriched model for the analysis of masonry panel. International Journal of Solids and Structures 49, 865–880.

Addessi, D., Sacco, E., 2014. A kinematic enriched plane state formulation for the analysis of masonry panels. European Journal of Mechanics-A/Solids 44, 188–200.

Addessi, D., Sacco, E., 2016a. Enriched plane state formulation for nonlinear homogenization of in-plane masonry wall. Meccanica 51, 2891–2907.

Addessi, D., Sacco, E., 2016b. Nonlinear analysis of masonry panels using a kinematic enriched plane state formulation. International Journal of Solids and Structures 90, 194–214.

Addessi, D., Sacco, E., 2018. Homogenization of heterogeneous masonry beams. Meccanica 53, 1699–1717.

Addessi, D., Sacco, E., Di Re, P., 2018. Multi-scale analysis of masonry structures, in: Proceedings of the International Masonry Society Conferences, pp. 307–323.

Alfano, G., Rosati, L., Valoroso, N., 2000. A numerical strategy for finite element analysis of no-tension materials. International journal for numerical methods in engineering 48, 317–350.

Alshebani, M.M., Sinha, S.N., 2000. Stress-strain characteristics of brick masonry under cyclic biaxial compression. Journal of Structural Engineering 126, 1004–1007.

Angelillo, M., 1994. A finite element approach to the study of no-tension structures. Finite elements in analysis and design 17, 57–73.

Anthoine, A., 1995. Derivation of the in-plane elastic characteristics of masonry through homogenization theory. International journal of solids and structures 32, 137–163.

Anthoine, A., Magonette, G., Magenes, G., 1995. Shear-compression testing and analysis of brick masonry walls. Proceedings of the 10th European Conference on Earthquake Engineering, Balkema, Rotterdam , 1657–1662.

Atkinson, R., Amadei, B., Saeb, S., Sture, S., 1989. Response of masonry bed joints in direct shear. Journal of Structural Engineering 115, 2276–2296.

Backes, H., 1985. On the behavior of masonry under tension in the direction of the bed joints. Dissertation, Aachen University of Technology, Aachen, Germany .

Baggio, C., Trovalusci, P., 2000. Collapse behaviour of three-dimensional brick-block systems using non-linear programming. Structural Engineering and Mechanics 10, 181.

Bažant, Z.P., 1984. Imbricate continuum and its variational derivation. Journal of Engineering Mechanics 110, 1693–1712.

Bazant, Z.P., Belytschko, T.B., Chang, T.P., et al., 1984. Continuum theory for strain-softening. Journal of Engineering Mechanics 110, 1666–1692.

Bažant, Z.P., Jirásek, M., 2002. Nonlocal integral formulations of plasticity and damage: survey of progress. Journal of engineering mechanics 128, 1119–1149.

Bažant, Z.P., Oh, B.H., 1983. Crack band theory for fracture of concrete. Matériaux et construction 16, 155–177.

Bažant, Z.P., Pijaudier-Cabot, G., 1988. Nonlocal continuum damage, localization instability and convergence .

Becchi, A., Foce, F., 2002. Degli archi e delle volte: arte del costruire tra meccanica e stereotomia .

Bélidor, B.F., 1729. La Science des ingénieurs.

Bellini, A., Incerti, A., Bovo, M., Mazzotti, C., 2018. Effectiveness of frcm reinforcement applied to masonry walls subject to axial force and out-of-plane loads evaluated by experimental and numerical studies. International Journal of Architectural Heritage 12, 376–394.

Bellini, A., Incerti, A., Mazzotti, C., 2017. Out-of-plane strengthening of masonry walls with frcm composite materials, in: Key engineering materials, Trans Tech Publ. pp. 158–165.

Berto, L., Saetta, A., Scotta, R., Vitaliani, R., 2002. An orthotropic damage model for masonry structures. International Journal for Numerical Methods in Engineering 55, 127–157.

Betti, M., Vignoli, A., 2011. Numerical assessment of the static and seismic behaviour of the basilica of santa maria all'impruneta (italy). Construction and Building Materials 25, 4308–4324.

Binda, L., Gambarotta, L., Lagomarsino, S., Modena, C., 1999. A multilevel approach to the damage assessment and seismic improvement of masonry buildings in italy. Seismic damage to masonry buildings , 170–195.

Binda, L., Penazzi, D., Baronio, G., Tedeschi, C., 2000. Caratteristiche delle murature in pietra e mattoni ai fini dell'individuazione di opportune tecniche di riparazione. CNR-GNDT.

Binda, L., Penazzi, D., Saisi, A.E., 2003. Historic masonry buildings: Necessity of a classification of structures and masonries for the adequate choice of analytical model, in: 6th International Symp. Computer Methods in Structural Masonry (STRUMAS VI), Computers & Geotechnics Ltd. pp. 168–173.

Binda, L., Saisi, A., 2001. State of the art of research on historic structures in italy. Dept. of structural engineering, Politecnico of Milan, Italy .

Binda, L., Saisi, A.E., 2002. Conservazione degli edifici storici. il miglioramento strutturale e la compatibilità tra i materiali e la struttura originaria .

Blaauwendraad, J., 1985. Realisations and restrictions: Application of numerical models to concrete structures, in: Finite element analysis of reinforced concrete structures, ASCE. pp. 557–578.

Blaauwendraad, J., Grootenboer, H., 1981. Essentials for discrete crack analysis. IABSE Reports 34, 263–272.

Brasile, S., Casciaro, R., 2009. Multilevel approach for brick masonry walls–part iii: A strategy for free vibration analysis. Computer methods in applied mechanics and engineering 198, 3934–3943.

Bruggi, M., Taliercio, A., 2015. Analysis of no-tension structures under monotonic loading through an energy-based method. Computers & Structures 159, 14–25.

Calderini, C., Cattari, S., Lagomarsino, S., 2009. In-plane strength of unreinforced masonry piers. Earthquake engineering & structural dynamics 38, 243–267.

Caliò, I., Marletta, M., Pantò, B., 2012. A new discrete element model for the evaluation of the seismic behaviour of unreinforced masonry buildings. Engineering Structures 40, 327–338.

Cancelliere, I., Imbimbo, M., Sacco, E., 2010. Experimental tests and numerical modeling of reinforced masonry arches. Engineering Structures 32, 776–792.

Cardani, G., Binda, L., 2013. Guidelines for the masonry quality evaluation in built heritage, in: BH2013-Built Heritage 2013 Monitoring Conservation Management, Citeseer. pp. 1–6.

Carocci, C.F., 2001. Guidelines for the safety and preservation of historical centres in seismic areas. Historical constructions , 145–166.

Cavalagli, N., Cluni, F., Gusella, V., 2011. Strength domain of non-periodic masonry by homogenization in generalized plane state. European Journal of Mechanics A/Solids 30, 113–126.

Cecchi, A., Milani, G., Tralli, A., 2005. Validation of analytical multiparameter homogenization models for out-of-plane loaded masonry walls by means of the finite element method. Journal of engineering mechanics 131, 185–198.

Červenka, J., Bažant, Z.P., Wierer, M., 2005. Equivalent localization element for crack band approach to mesh-sensitivity in microplane model. International Journal for Numerical Methods in Engineering 62, 700–726.

Chen, S.Y., Moon, F., Yi, T., 2008. A macroelement for the nonlinear analysis of in-plane unreinforced masonry piers. Engineering Structures 30, 2242–2252.

Ciocci, M.P., Sharma, S., Lourenço, P.B., 2018. Engineering simulations of a super-complex cultural heritage building: Ica cathedral in peru. Meccanica 53, 1931–1958.

Comi, C., Perego, U., 2001. Fracture energy based bi-dissipative damage model for concrete. International journal of solids and structures 38, 6427–6454.

Cordebois, J., et al., 1982. Endommagement anisotrope en élasticité et plasticité .

Coulomb, C., 1773. Essai sur une application des regles des maximis et minimis a quelques problemes de statique rdlatifs a l'architecture, mem. Acad. Roy. Pres. Divers Savants , 343–382.

Couplet, P., 1729. De la poussée des voûtes. Histoire de l'Académie Royale des Sciences 79, 117.

Couplet, P., 1730. Seconde partie de l'examen de la poussée des voûtes. Mémoires de l'Académie Royale des Sciences Paris , 117–141.

Cundall, P.A., 1971. A computer model for simulating progressive, large-scale movement in blocky rock system, in: Proceedings of the International Symposium on Rock Mechanics, 1971.

Da Porto, F., Valluzzi, M.R., Modena, C., 2003. Investigations for the knowledge of multi-leaf stone masonry walls, in: Proceedings of the First International Congress on Construction History, p. 24th.

D'Altri, A.M., Sarhosis, V., Milani, G., Rots, J., Cattari, S., Lagomarsino, S., Sacco, E., Tralli, A., Castellazzi, G., de Miranda, S., 2019. Modeling strategies

for the computational analysis of unreinforced masonry structures: Review and Classification. Archives of Computational Methods in Engineering 26, 1–33.

Danyzy, A., 1732. Méthode générale pour déterminer la résistance qu'il faut opposer à la poussée des voûtes. Histoire de la Société Royale des Sciences établie à Montpellier 2, 40–56.

D'Ayala, D., 2004. Unreinforced brick masonry construction. University of Bath, United Kingdom .

De Bellis, M., Addessi, D., 2011. A Cosserat based multi-scale model for masonry structures. International Journal for Multiscale Computational Engineering 9, 543–563.

De Borst, R., 1991. Simulation of strain localization: a reappraisal of the cosserat continuum. Engineering computations .

De Borst, R., Nauta, P., 1985. Non-orthogonal cracks in a smeared finite element model. Engineering Computations 2 (3), 35-46.(1985) .

Di Carlo, F., Coccia, S., Rinaldi, Z., 2018. Collapse load of a masonry arch after actual displacements of the supports. Archive of Applied Mechanics 88, 1545–1558.

Di Re, P., Addessi, D., Sacco, E., 2018. A multiscale force-based curved beam element for masonry arches. Computers & Structures 208, 17–31.

DIANA, 2019. User's manual of displacement analyzer finite element software package, release 10.3. diana fea, delft, https://dianafea.com/manuals/d103/diana.html. .

Drucker, D., 1954. Coulomb friction, plasticity and plastic analysis of limit loads. J. appl. Mech. 21, 7–1.

Drysdale, R., Vanderkeyl, R., Hamid, A., 1982. Shear strength of brick masonry joints, in: Proc. 5 th Int. Brick Masonry Conf.(VIBMaC) held in Washington, DC, 5-10 Oct., 1979. Edited by J. A. Wintz and A. H. Yorkdale. McLean, Virginia, p. 106.

Feenstra, P.H., 1993. Computational aspects of biaxial stress in plain and reinforced concrete. PhD thesis, Delft University of Technology .

Frézier, A.F., 1737. La théorie et la pratique de la coupe de pierres et des bois pour la construction des voûtes et autres parties des bâtiments civils et militaires, ou traité de stéréotomie à l'usage de l'architecture. Strasbourg/Paris: Charles-Antoine Jombert .

Gambarotta, L., Lagomarsino, S., 1997. Damage models for the seismic response of brick masonry shear walls part ii: the continuum model and its application. Earthquake Engineering and Structural Dynamics 26, 441–462.

Ganz, H., Thürlimann, B., 1982. Tests on the biaxial strength of masonry. Rep. No. 7502 3.

Gatta, C., 2019. Masonry nonlinear response: modeling and analysis of the effects of damaging mechanisms. Sapienza, Università di Roma, Italy. Ph.D. thesis .

Gatta, C., Addessi, D., Vestroni, F., 2018. Static and dynamic nonlinear response of masonry walls. International Journal of Solids and Structures 155, 291–303.

Gilbert, M., Casapulla, C., Ahmed, H., 2006. Limit analysis of masonry block structures with non-associative frictional joints using linear programming. Computers & structures 84, 873–887.

Giuffrè, A., 1993a. Safety and conservation of historical centers. Bari: Editori Laterza .

Giuffrè, A., 1993b. Sicurezza e conservazione dei centri storici. Il caso Ortigia , 279.

Giuffrè, A., 1994. Seismic safety and strengthening of historical buildings and urban fabrics, in: Proceedings of the 10th World Conference on Earthquake Engineering, pp. 6583–6596.

Greco, F., Leonetti, L., Luciano, R., Blasi, P.N., 2016. An adaptive multiscale strategy for the damage analysis of masonry modeled as a composite material. Composite Structures 153, 972–988.

Greco, F., Leonetti, L., Luciano, R., Trovalusci, P., 2017. Multiscale failure analysis of periodic masonry structures with traditional and fiber-reinforced mortar joints. Composites Part B: Engineering 118, 75–95.

Gregory, D., 1697. Catenaria. Phil. Trans, 19(231) , 637–652.

Griffith, M.C., Vaculik, J., Lam, N., Wilson, J., Lumantarna, E., 2007. Cyclic testing of unreinforced masonry walls in two-way bending. Earthquake Engineering & Structural Dynamics 36, 801–821.

Heyman, J., 1966. The stone skeleton. International Journal of Solids and Structures 2, 249 – 279.

Heyman, J., Jacques, H., 1998. Structural analysis: a historical approach. Cambridge University Press.

Hilsdorf, H.K., 1969. Investigation into the failure mechanism of brick masonry loaded in axial compression. Designing engineering and constructing with masonry products , 34–41.

Hofmann, P., Stockl, S., 1986. Tests on the shear-bond behaviour in the bed-joints of masonry. MASONRY INT. Masonry Int. , 1.

Iannuzzo, A., 2018. A new rigid block model for masonry structures.Università degli Studi di Napoli Federico II. Ph.D. thesis.

Jirásek, M., 2002. Objective modeling of strain localization. Revue française de génie civil 6, 1119–1132.

Jirásek, M., 2011. Damage and smeared crack models, in: Numerical modeling of concrete cracking. Springer, pp. 1–49.

Kachanov, L.M., 1958. Rupture time under creep conditions .

Karapitta, L., Mouzakis, H., Carydis, P., 2011. Explicit finite-element analysis for the in-plane cyclic behavior of unreinforced masonry structures. Earthquake engineering & structural dynamics 40, 175–193.

Kooharian, A., 1952. Limit analysis of voussoir (segmental) and concrete archs, in: Journal Proceedings, pp. 317–328.

La Hire, P., 1695. Traité de mécaniqueo: ou l'on explique tout ce qui est nécessaire dans la pratique the arts, les propriétés des corps pesants lesquelles ont un plus grand usage dans la physique. Paris: de l'Imprimerie Royale et se vend chez Jean Anisson. .

La Hire, P., 1712.). sur la construction des voûtes dans les édifices. Mémoires de l'Académie Royale des Sciences. , 69–77.

Lagomarsino, S., Penna, A., Galasco, A., Cattari, S., 2013. Tremuri program: an equivalent frame model for the nonlinear seismic analysis of masonry buildings. Engineering structures 56, 1787–1799.

Leibniz, G.W., 1691. De solutionibus problematis catenarii vel funicolaris. Ada Eruditorum , 435–439.

Lemaitre, J., 1985. A continuous damage mechanics model for ductile fracture .

Lemos, J.V., 2007. Discrete element modeling of masonry structures. International Journal of Architectural Heritage 1, 190–213.

Leonetti, L., Greco, F., Trovalusci, P., Luciano, R., Masiani, R., 2018. A multiscale damage analysis of periodic composites using a couple-stress/cauchy multidomain model: Application to masonry structures. Composites Part B: Engineering 141, 50–59.

Liberatore, D., Addessi, D., Sangirardi, M., 2017. A force-based macroelement for the nonlinear dynamic analysis of masonry buildings, in: AIMETA 2017 XXIII conference. The Italian Association of Theoretical and Applied Mechanics, Salerno, Italy.

Liberatore, D., Addessi, D., Sangirardi, M., 2019. An enriched bouc-wen model with damage. European Journal of Mechanics-A/Solids 77, 103771.

Litton, R.W., 1974. A contribution to the analysis of concrete structures under cyclic loading. Ph.D. thesis, University of California, Berkeley .

Lloberas-Valls, O., Rixen, D., Simone, A., Sluys, L.J., 2012. Multiscale domain decomposition analysis of quasi-brittle heterogeneous materials. International Journal for Numerical Methods in Engineering 89, 1337–1366.

Lourenço, P.B., 1996. Computational Strategies for Masonry Structures. Ph.D. thesis. Delft University of Technology.

Lourenço, P.B., De Borst, R., Rots, J.G., 1997. A plane stress softening plasticity model for orthotropic materials. International Journal for Numerical Methods in Engineering 40, 4033–4057.

Lourenço, P.B., Rots, J.G., 1997. Multisurface interface model for analysis of masonry structures. Journal of Engineering Mechanics 123, 660–668.

Lourenço, P.B., 1998. Experimental and numerical issues in the modelling of the mechanical behaviour of masonry .

Lourenço, P.B., 2001. Analysis of historical constructions: from thrust-lines to advanced simulations. Historical constructions , 91–116.

Lourenço, P.B., 2010. Recent advances in masonry modelling: micromodelling and homogenisation, in: Multiscale modeling in solid mechanics: computational approaches. World Scientific, pp. 251–294.

Lourénço, P.B., De Borst, R., Rots, J.G., 1997. A plane stress softening plasticity model for orthotropic materials. International Journal for Numerical Methods in Engineering 40, 4033–4057.

Lourenço, P.B., Oliveira, D.V., Roca, P., Orduña, A., 2005. Dry joint stone masonry walls subjected to in-plane combined loading. Journal of Structural Engineering 131, 1665–1673.

Lourenço, P.J.B.B., 1997. Computational strategies for masonry structures. .

Magenes, G., Calvi, G., 1997. In-plane seismic response of brick masonry walls. Earthquake Engineering and Structural Dynamics 26, 1091–1112.

Mamaghani, I.H., Aydan, Ö., Kajikawa, Y., 1999. Analysis of masonry structures under static and dynamic loading by discrete finite element method. Doboku Gakkai Ronbunshu 1999, 1–12.

Masiani, R., Trovalusci, P., 1996. Cosserat and cauchy materials as continuum models of brick masonry. Meccanica 31, 421–432.

McNary, W.S., Abrams, D.P., 1985. Mechanics of masonry in compression. Journal of Structural Engineering 111, 857–870.

Melbourne, C., Wang, J., Tomor, A.K., 2007. A new masonry arch bridge assessment strategy (smart), in: Proceedings of the Institution of Civil Engineers-Bridge Engineering, Thomas Telford Ltd. pp. 81–87.

Michon, F., 1848. Tables et formules pratiques pour l'établissement des voûtes cylindriques. Mémorial de l'Officier du Génie 15, 7–117.

Milani, G., 2011. Simple lower bound limit analysis homogenization model for in- and out-of-plane loaded masonry walls. Construction and Building Materials 25, 4426–4443.

Minga, E., Macorini, L., Izzuddin, B.A., 2018. A 3d mesoscale damage-plasticity approach for masonry structures under cyclic loading. Meccanica 53, 1591–1611.

Misseri, G., DeJong, M.J., Rovero, L., 2018. Experimental and numerical investigation of the collapse of pointed masonry arches under quasi-static horizontal loading. Engineering Structures 173, 180–190.

Mistler, M., Anthoine, A., Butenweg, C., 2007. In-plane and out-of-plane homogenisation of masonry. Computers & Structures 85, 1321–1330.

Naraine, K., Sinha, S., 1991. Cyclic behavior of brick masonry under biaxial compression. Journal of Structural Engineering 117, 1336–1355.

Navier, C., 1833-38. Résumé des leçons données à l'ecole des ponts et chaussées, sur l'application de la mécanique à l'établissement des construcions et des machines. deuxième édition corrigée et augmentée (3 vols). Paris: Carilian-Goeury .

Nodargi, N.A., Intrigila, C., Bisegna, P., 2020. Limit analysis of dry masonry block assemblages with non-associative frictional joints, in: AIP Conference Proceedings, AIP Publishing LLC. p. 020033.

Oliveira, D., Lourenço, P.B., 2004. Implementation and validation of a constitutive model for the cyclic behaviour of interface elements. Computers & Structures 82, 1451–1461.

Oliveira, D.V., 2003. Experimental and numerical analysis of blocky masonry structures under cyclic loading .

Oliveira, D.V., Basilio, I., Lourenço, P.B., 2010. Experimental behavior of FRP strengthened masonry arches. Journal of Composites for Construction 14, 312–322.

Oliver, J., 1989. A consistent characteristic length for smeared cracking models. International Journal for Numerical Methods in Engineering 28, 461–474.

Orduña, A., Lourenço, P.B., 2005. Three-dimensional limit analysis of rigid blocks assemblages. part i: Torsion failure on frictional interfaces and limit analysis formulation. International Journal of Solids and Structures 42, 5140–5160.

Page, A., 1981. The biaxial compressive strength of brick masonry. Proceedings of the Institution of Civil Engineers 71, 893–906.

Page, A., 1983. The strength of brick masonry under biaxial tension-compression. International journal of masonry construction 3, 26–31.

Page, A.W., 1978. Finite element model for masonry. Journal of the Structural Division, New York: ASCE 104, 1267–1285.

Peerlings, R.H., de Borst, R., Brekelmans, W.M., De Vree, J., 1996. Gradient enhanced damage for quasi-brittle materials. International Journal for numerical methods in engineering 39, 3391–3403.

Pelà, L., Cervera, M., Roca, P., 2013. An orthotropic damage model for the analysis of masonry structures. Construction and Building Materials 41, 957–967.

Pietruszczak, S., Mroz, Z., 1981. Finite element analysis of deformation of strain-softening materials. International Journal for Numerical Methods in Engineering 17, 327–334.

Pijaudier-Cabot, G., Bažant, Z.P., 1987. Nonlocal damage theory. Journal of engineering mechanics 113, 1512–1533.

Pijaudier-Cabot, P., Bazant, Z.L., 1987. Non local damage theory. Journal of Engineering Mechanics ASCE 118, 1512–1533.

Van der Pluijm, R., 1997. Non-linear behaviour of masonry under tension. HERON-ENGLISH EDITION- 42, 25–54.

Van der Pluijm, R., 1998. Overview of deformation controlled combined tensile and shear tests. Rep. TUE/CCO 98.

Van der Pluijm, R., 1999. Out-of-plane bending of masonry: behaviour and strength .

Van der Pluijm, R., Rutten, H., Ceelen, M., 2000. Shear behaviour of bed joints 12th international brick, in: Block Masonry Conference.

Van der Pluijm, R.V., 1993. Shear behavior of bed joints, in: Proceedings of the 6th Canadian Masonry Symposium, pp. 125–136.

Raffa, M.L., Lebon, F., Sacco, E., Welemane, H., 2013. A multi-level interface model for damaged masonry.

Rashid, Y., 1968. Ultimate strength analysis of prestressed concrete pressure vessels. Nuclear engineering and design 7, 334–344.

Reccia, E., Leonetti, L., Trovalusci, P., Cecchi, A., 2018. A multi-scale/multidomain model for the failure analysis of masonry walls: a validation with a combined FEM/DEM approach. International Journal for Multiscale Computational Engineering 16, 325–343.

Roca, P., Cervera, M., Gariup, G., Pelà, L., 2010. Structural analysis of masonry historical constructions. Classical and advanced approaches. Archives of Computational Methods in Engineering 17, 299–325.

Roca, P., Lourenço, P.B., Gaetani, A., 2019. Historic Construction and Conservation: Materials, Systems and Damage. Routledge.

Rodrıguez-Ferran, A., Morata, I., Huerta, A., 2004. Efficient and reliable nonlocal damage models. Computer methods in applied mechanics and engineering 193, 3431–3455.

Rosa Valluzzi, M., Da Porto, F., Casarin, F., Monteforte, N., Modena, C., 2009. A contribution to the characterization of masonry typologies by using sonic waves investigations. Actes des journées scientifiques du LCPC , 713–718.

Rots, J.G., 1988. Computational modeling of concrete fracture .

Sacco, E., 2009. A nonlinear homogenization procedure for periodic masonry. European Journal of Mechanics - A/Solids 28, 209–222.

Sacco, E., Toti, J., 2010. Interface elements for the analysis of masonry structures. International Journal for Computational Methods in Engineering Science and Mechanics 11, 354–373.

Sangirardi, M., Liberatore, D., Addessi, D., 2019. Equivalent frame modelling of masonry walls based on plasticity and damage. International Journal of Architectural Heritage 13, 1098–1109.

Saritas, A., Filippou, F.C., 2009. Numerical integration of a class of 3d plastic-damage concrete models and condensation of 3d stress–strain relations for use in beam finite elements. Engineering Structures 31, 2327–2336.

Selby, R.G., 1995. Three-dimensional constitutive relations for reinforced concrete .

Sena-Cruz, J., 2005. Strengthening of concrete structures with near-surface mounted cfrp laminate strips .

Sena-Cruz, J., Barros, J.A., Azevedo, Á.F., 2004. Elasto-plastic multi-fixed smeared crack model for concrete. Technical Report. Universidade do Minho. Departamento de Engenharia Civil (DEC).

Serpieri, R., Albarella, M., Sacco, E., 2017. A 3d microstructured cohesive–frictional interface model and its rational calibration for the analysis of masonry panels. International Journal of Solids and Structures 122, 110–127.

Sorrentino, L., D'Ayala, D., de Felice, G., Griffith, M.C., Lagomarsino, S., Magenes, G., 2017. Review of out-of-plane seismic assessment techniques applied to existing masonry buildings. International Journal of Architectural Heritage 11, 2–21.

de Souza Neto, E.A., Peric, D., Owen, D.R., 2011. Computational methods for plasticity: theory and applications. John Wiley & Sons.

Stefanou, I., Sab, K., Heck, J.V., 2015. Three dimensional homogenization of masonry structures with building blocks of finite strength: A closed form strength domain. International Journal of Solids and Structures 54, 258–270.

Stirling, J., 1717. Lineae tertii ordinis Neutonianae, sive, Illustratio tractatus D. Neutoni De enumeratione linearum tertii ordinis: cui subjungitur, solutio trium problematum.

Taliercio, A., 2014. Closed-form expressions for the macroscopic in-plane elastic and creep coefficients of brick masonry. International Journal of Solids and Structures 51, 2949–2963.

Taylor, R.L., 2017. FEAP-A finite element analysis program. Version 8.5. Department of Civil and Environmental Engineering, University of California at Berkeley, California.

Tesei, C., Ventura, G., 2016. A unilateral nonlocal tensile damage model for masonry structures. Procedia Structural Integrity 2, 2690–2697.

Toti, J., Gattulli, V., Sacco, E., 2015. Nonlocal damage propagation in the dynamics of masonry elements. Computers & Structures 152, 215–227.

Vecchio, F.J., Collins, M.P., 1986. The modified compression-field theory for reinforced concrete elements subjected to shear. ACI J. 83, 219–231.

Willam, K., Pramono, E., Sture, S., 1989. Fundamental issues of smeared crack models, in: Fracture of concrete and rock. Springer, pp. 142–157.

Zucchini, A., Lourenço, P.B., 2009. A micro-mechanical homogenisation model for masonry: Application to shear walls. International Journal of Solids and Structures 46, 871–886.